
MODELING PROPELLED PARTICLE SYSTEMS IN 2D

— from Particles to Fields —

Christoph Alexander Gerhard Weber



Munich, 2013

MODELING PROPELLED PARTICLE SYSTEMS IN 2D

— from Particles to Fields —

Christoph Alexander Gerhard Weber

PHD-thesis
at the Arnold-Sommerfeld-Center,
Chair for Biological & Statistical Physics,
Ludwig-Maximilians-University
Munich

by
Christoph Alexander Gerhard Weber
from Munich

Munich, 14.5.2013

First referee : Prof. Erwin Frey

Second referee: Prof. Andreas R. Bausch

Date of oral examination: 15.07.2013

Contents

Zusammenfassung	vii
Summary	ix
1 Introduction to Propelled Particle Systems	1
1.1 What is a Propelled Particle System?	1
1.2 Modeling Propelled Particle Systems — State of the Art	3
1.3 Outline	6
2 Modeling Propelled Particle Systems	7
2.1 The Gliding Assay – A Paradigm for <i>in-vitro</i> Active Systems	7
2.1.1 <i>Anomalous</i> Contour Fluctuations	9
2.1.2 Gliding Assay at <i>High</i> Filament Densities	15
2.1.3 Gliding Assay with Crosslinkers — Freezing of Activity	18
2.2 The Vibrated Polar Disk Assay	25
2.2.1 Qualitative Experimental Observations	26
2.2.2 Quantitative Modeling of the Dynamics of Vibrated Polar Disks	27
2.3 Modeling Propelled Particle Systems under Dilute Conditions	33
2.3.1 Rule-based Automaton with Local Interactions	33
2.3.2 Digression: Kinetic Theory for Propelled Particle Systems — Basic Assumptions & Findings	37
2.3.3 Kinetic Theory for Propelled Particle Systems: Open questions	40
2.3.4 Particle Length in a Kinetic Description	41
2.3.5 Role of Particle Conservation for Propelled Particle Systems	44
2.3.6 Non-perfect Active Collisions: Deviations from Half-angle Alignment	50
2.3.7 Scrutinizing Quantitatively Kinetic Theory: Role of Correlations	53
2.4 Propelled Particle Systems at High Densities	60
2.4.1 Agent-based Model	60
2.4.2 Results for Propelled Particles at Large Densities	61

A List of Publications	65
B Selected Publications	67
B.1 Polar Patterns of Driven Filament	68
B.2 Polar Pattern Formation: Hydrodynamic Coupling of Driven Filaments . .	69
B.3 Frozen Steady States in Active Systems	70
B.4 Nucleation-induced Transition to Collective Motion in Active Systems	71
B.5 Role of Particle Conservation in Self-propelled Particle Systems	72
B.6 Long-range Ordering of Vibrated Polar Disks	73
B.7 A Critical Assessment of the Boltzmann Approach for Active Systems . . .	74
B.8 Understanding Collective Dynamics of Soft Active Colloids by Binary Scattering	75
B.9 Defect-Mediated Transition in Active Soft Matter	76
C Materials & Methods for Section on <i>Anomalous</i> Contour Fluctuations	89
Acknowledgement	97

Zusammenfassung

Der Vogel fliegt, die Zelle wandert, das Bakterium schwimmt. Jedes dieser Individuen gehört zur Klasse der angetriebenen Partikelsysteme. Jedes besitzt seinen eigenen Antrieb. Und jedes führt eine persistente Zufallsbewegung aus. Kommt es zu einer Anhäufung gleichartiger Individuen lässt sich oft ein beeindruckender Selbstorganisationsprozess beobachten. Populäre Beispiele sind die Schwarmbildung von Vögeln oder das kohärente Bewegen ganzer Zell- oder Bakterienkolonien. Die Entstehung von kollektiver Bewegung in diesen Nichtgleichgewichtssystemen ist ein allgegenwärtiges Naturschauspiel —und auch ein besonders faszinierendes. Vermutlich entspringt diese Faszination der Bildung zeitabhängiger örtlicher Muster wie Cluster, Wirbel oder Wellen, deren charakteristische Ausdehnungen die der Individuen bei weitem überragen. Für die Aufschlüsselung der physikalischen Prinzipien, die der Entstehung kollektiver Bewegung zu Grunde liegen, wurden diverse theoretische Studien durchgeführt; von partikelbasierten Simulationen über kinetische Theorien bis hin zu hydrodynamischen Modellen. Diese Modelle wurden jedoch typischerweise von der Idee inspiriert, dass die zugrundeliegenden Nichtgleichgewichtsprozesse generisch und universell sind, und damit vermissen sie den direkten Bezug zu echten, experimentellen Systemen.

Diese Arbeit beinhaltet verschiedene theoretische Modellierungsansätze von angetriebenen Partikelsystemen, deren Resultate entweder in qualitativer oder quantitativer Übereinstimmung mit kürzlich durchgeführten Experimenten stehen. Im Speziellen werden zwei experimentelle Systeme betrachtet: Der *Aktin-„gliding assay“*, in dem molekulare Motoren, fixiert auf einer Oberfläche, Aktinfilamente bewegen, und der *„vibrated polar disk assay“*, in welchem scheibenförmiges Granulat mit einer eingebauten polaren Asymmetrie durch vertikale Vibrationen des Substrats angetrieben wird. Mittels diverser theoretischer Werkzeuge und Methoden, wie regelbasierter Automatenmodelle, numerischer Lösungen Newtonscher Bewegungsgleichungen, kinetischer Theorie und Hydrodynamik, war es möglich die folgenden neuen Erkenntnisse im Bereich angetriebener Partikel zu erzielen:

Es konnte gezeigt werden, dass die anomalen Krümmungsfluktuationen von einzelnen Aktinfilamenten im „gliding assay“ durch zwei verschiedene Interaktionsarten mit den molekularen Motoren bedingt werden. Die Motoren ‘drücken’ oder ‘halten’, und erzeugen damit entweder eine persistente Bewegung oder führen zu einem lokalen Stau, der wiederum die beobachteten starken Krümmungen verursacht. Interessanterweise werden Erregung und Relaxation dieser starken Krümmungen ausschließlich durch diese Interaktionen bedingt, wobei der thermische Anteil an Erregung und Relaxation nahezu irrelevant ist.

Bei hohen Dichten entstehen im „gliding assay“ facettenreiche Muster bestehend aus sich kohärent bewegenden Strukturen, wie Cluster, Wirbel oder Wellen. Es wurde gezeigt, dass sich die Muster aufgrund von lokalen, ausrichtenden Wechselwirkungen, ähnlich denen im Ferromagneten, bilden. In der späteren Phase der Musterbildung werden hydrodynamische Wechselwirkungen relevant. Die kohärent bewegenden Cluster erzeugen einen der Bewegungsrichtung entgegengesetzten Fluss der darüber liegenden Flüssigkeit, wodurch eine repulsive hydrodynamische Interaktion zwischen Cluster und zwischen Cluster und Rand, vermittelt wird.

Wenn man nun Verknüpferte Proteine zum „gliding assay“ bei hohen Filamentdichten hinzu gibt, kann man die Entstehung eines sogenannten absorbierenden Zustands, bestehend aus sich fortwährend drehenden Ringen, welche in zwei Morphologien (offen und geschlossen) vorliegen, beobachten. Die Physik der Entstehung dieser Strukturen kann man sich als einen Wettstreit von zwei Ereignissen vorstellen: dem Verschmelzen von Filamentstrukturen und dem seitlichen Wachstum dieser, das wiederum die Krümmung einfrieren lässt. Dieses Erkenntnis konnte durch die Verwendung eines geeigneten partikelbasierten Modells erlangt werden. Darüber hinaus erlaubte es die qualitative Reproduktion der Ringradienverteilung und des Ratios der offenen und geschlossenen Ringe als Funktion der „Noise“-Stärke des Systems.

Der „*polar vibrated disk assay*“ hat eine Ausdehnung von nur etwa 20 Partikeldurchmessern, was eine Festlegung der Art des Phasenübergangs zu einem geordneten, fließenden Zustand unmöglich macht. Mittels eines mikroskopischen Modells konnte die Einzelpartikelbewegung im Experiment, die Details der binären Stöße, sowie die kollektive Dynamik in der experimentellen Geometrie reproduziert werden. Genauer gesagt wurden alle Eigenschaften der persistenten Zufallsbewegung, die mittlere Geschwindigkeit, die Amplitude und das Spektrum der Orientierungs- und Geschwindigkeitsfluktuationen im Experiment vom Modell wiedergegeben. Die Übereinstimmung der Charakteristika der Stöße wurde überprüft, indem die Wahrscheinlichkeitsverteilungen der Stoßlänge und Stoßdauer verglichen wurden. Schlussendlich wurden die kollektiven Eigenschaften zwischen Modell und Experiment durch eine Gegenüberstellung der mittleren Polarisation verglichen. Die quantitative Übereinstimmung all dieser Details erlaubte es, unser Modell im Computer hochzuskalieren und damit die Frage zu beantworten, ob der „*polar vibrated disk assay*“ tatsächlich langreichweitige polare Ordnung ausbilden kann.

Darüberhinaus wurde ein regelbasiertes Automatenmodell für angetriebene Partikel entworfen, um die Entstehung kollektiver Bewegung als Funktion der Zeit zu untersuchen. Das zentrale Resultat ist, dass kollektive Bewegung nahe des Übergangs durch Nukleation eines Clusters ausreichend großer Masse angeregt wird, und nicht wie verbreitet angenommen, aus einem Vergrößerungsprozess von ausgerichteten Domänen hervorgeht.

Nahe der Phasengrenzkurve findet man wellenförmige Muster in teilchenzahlerhaltenden, angetriebenen Partikelsystemen. Im Rahmen einer Analyse kinetischer Theorie für angetriebene Systeme werden keine wellenartigen Muster beobachtet, sobald die Teilchenzahlerhaltung verletzt wird.

Zudem finden wir, dass die Anwendung kinetischer Theorie angetriebener Systeme auf *schwachausrichtende* Stöße beschränkt ist, in welchen der Winkel nach dem Stoß nur ge-

ringfügig verglichen mit dem Relativwinkel vor dem Stoß reduziert wird. Die Aussage wurde ermöglicht, indem kinetische Theorie für angetriebene Systeme bezüglich ausschlaggebender *qualitativer* Eigenschaften von Stößen erweitert wurde, die aus kürzlich durchgeführten Experimenten extrahiert wurden. Da kinetische Theorie Unordnung in Parameterbereichen vorhersagt in denen sich echte (experimentelle) Systeme anordnen, konnten die inhärente Einschränkung auf schwachausrichtende Stöße herausgearbeitet werden.

Außerdem wurden Newtonsche Gleichungen für angetriebene dissipative Kolloide numerisch analysiert. Es wurde entdeckt, dass nahe der Phasengrenzkurve die Mikrozustände beim Einsetzen des Ordnungsübergangs nicht frei von Orientierungskorrelationen sind. Damit ist die Annahme des molekularen Chaos —eine gar typische Annahme in kinetischen Theorien— für angetriebene Partikelsysteme am Ordnungsübergang *nicht* erfüllt. Noch wichtiger ist, dass die gefundenen Korrelationen für das betrachtete kolloidale System eine qualitative Voraussetzung darstellen, damit kinetische Theorie für angetriebene Systeme überhaupt einen Ordnungsübergang vorhersagt. Der Gewinn dieser Erkenntnis fusst auf der Tatsache, dass der Stoßprozess quantitativ mit der mesoskopischen Beschreibung verknüpft wurde, ohne eine Näherung zu verwenden. Dies erlaubt wiederum eine quantitative Überprüfung der kinetischen Theorie. Implementiert man nun die beobachteten Korrelationen in den kinetischen Zugang, stimmt die aus kinetischer Theorie berechnete Phasengrenzkurve im Regime geringer Packungsdichten mit der aus der numerischen Lösung der Newtonschen Bewegungsgleichung gewonnenen, überein.

Zuletzt wurde das Regime großer Packungsdichten mittels eines geeigneten partikelbasierten Modells für angetriebene Systeme untersucht. Durch Charakterisieren des Grades von Translationsordnung und hexatischer Orientierungsordnung konnten die folgenden generischen Zustände identifiziert werden: ein *unpolarisierter, aktiver Kristall* mit langreichweitiger Orientierungs- und Translationsordnung, und eine *polykristalline Phase*, die sich kollektiv bewegt und sich aus hexagonalen Domänen zusammensetzt. Es wurde gezeigt, dass die jeweiligen Übergänge durch eine charakteristische Defektdynamik bestimmt werden.

Die meisten Resultate dieser Arbeit veranschaulichen die Wichtigkeit eines direkten Abgleichs der Vorhersagen des Experiments mit denen der korrespondierenden Theorie, um angetriebene Systeme besser zu verstehen. Das zentrale Anliegen dieser Arbeit ist es die Mikroskopik angetriebener Systeme mit deren Makroskopik zu verknüpfen, sowie eine Beschreibung zu entwickeln, die den Beobachtungen im Experiment gerecht wird. Dieses Vorgehen wurde einem generischen Zugang stets vorgezogen, wodurch entscheidende Fortschritte im Verständnis der Physik zweier experimenteller Systeme erzielt werden konnten. Hoffentlich dient dieses Vorgehen als Vorlage und Motivation, analog auch in der Modellierung anderer aktiver Systeme, wie in der für bewegende Zellen oder Bakterien, vorzugehen.

Summary

Birds fly, cells crawl and bacteria swim. Each of these individuals has their own propulsion mechanism leading to a persistent motion, hence they all belong to the class referred to as *propelled particle* systems. Propelled particles in large number typically exhibit impressive self-organization processes such as the flocking motion of birds, the coherent motion of cell colonies and the swarming of bacteria. The emergence of collective motion in these non-equilibrium systems constitutes a ubiquitous phenomenon in nature—and perhaps one of the most fascinating. One reason for this might be the emergence of highly dynamic, coherently moving spatial patterns such as clusters, swirls or waves, and the fact that the patterns commonly extend over length scales much larger than the size of the individuals. To elucidate the physical principles underlying the collective motion of these particles, numerous theoretical studies have been devoted to model propelled particle systems by approaching the problem on all levels of description. These range from particle-based simulations to kinetic theory and hydrodynamic models. However, these models were typically inspired by the idea of universality and tended to analyze the generic non-equilibrium phenomena in propelled particle systems, thereby obscuring a one-to-one relation to experimental studies.

This thesis focusses on theoretical modeling approaches for propelled particle systems that are either in qualitative or quantitative agreement with recent observations and measurements in experimental propelled particle systems. Two experimental systems are specifically considered: The *actin gliding assay*, where molecular motors, immobilized on a substrate, propel actin filaments, and the *polar vibrated disk assay*, where disk-like granular particles with a built-in polar asymmetry are driven by vertical vibrations. By means of various theoretical tools including rule-based automaton models, numerical solution of Newtonian equations of motion, and kinetic theory, the following central new findings and insights within the field of propelled particle systems were discovered:

Anomalously strong curvature fluctuations of single actin filaments moving in the gliding assay arise from two different interactions with the molecular motors. The motors either “Push” or “Hold” locally, giving rise to persistent movement or localized jams, which, in turn, lead to pronounced curvature kinks. Interestingly, both excitation and relaxation of curvature originates from these interactions, and it is shown that the impact of thermal fluctuations on the curvature distribution is negligible compared to these *active fluctuations*.

At high densities, filaments in the gliding assay form beautiful patterns of coherent motion

such as clusters, swirls and waves. These patterns were shown to be triggered by *local* “ferromagnetic”-like alignment interactions between the filaments. In the later stages of pattern formation, hydrodynamic interactions become relevant. Coherently moving clusters induce a back-flow in the overlying fluid, mediating a ‘repulsive’ cluster–cluster or cluster–boundary interaction.

With the addition of crosslinking molecules to the gliding assay at high filament densities, an absorbing state comprised of open and closed rings can form. The assembly dynamics is fully understood in terms of a competition between merging events of filaments and filament growth that freezes the curvature. Specifically, by means of an appropriate particle-based model, the statistical properties of the system, such as the characteristics of the ring radii distribution and the ratio of open to closed rings as a function of the system’s noise level, was *qualitatively* reproduced.

The vibrated polar disk assay has a size of only about 20 particle diameters — a fact which precludes definitive conclusions on the nature of the underlying phase transition to a polarized state of coherent motion. By means of a microscopic model, the experimental single particle motion, the details of binary collisions and the collective dynamics in the confined geometry were *quantitatively* reproduced. Specifically, we matched all properties of the persistent random walk such as average speed, amplitude and spectrum of orientational and velocity fluctuations. Agreement between the characteristics of the collisions described by the model and those measured in the experiment, were verified by comparing the probability distributions for collision extension and time. Finally, collective properties were studied and likened by considering the average polarization within some restricted area, again confirming a very good agreement between model and experiment. The *quantitative* match of all details of the experimental dynamics allowed us to use our models to scale up the vibrated polar disk assay *in-silico*, proving that a long-range polar ordered state would develop in the vibrated disk assay in the absence of boundaries.

Moreover, a generic automaton model for propelled particles was employed to analyze the onset of collective motion in time. The central finding is that collective motion close to the transition is induced by nucleation of a cluster of sufficiently large mass, and not by a wide-spread coarsening process of polarized domains.

In particle-conserving, propelled particle systems wave-like patterns generically emerge close to the phase boundary. Considering kinetic theory, there are clear indications that wave-like patterns cannot exist in the absence of particle conservation.

Moreover, kinetic theory for propelled particle systems is found to be restricted to *weak aligning* systems, whereby post-collision angles are only slightly reduced with respect to pre-collision orientations. This conclusion was obtained by extending kinetic theory for propelled particle systems with respect to significant *qualitative* features of collisions observed in experimental propelled particle systems. Since kinetic theory predicts disorder for regimes in which real (experimental) systems exhibit order, the inherent restrictions of kinetic theory to weak aligning systems could be elucidated.

Furthermore, using a set of Newtonian equations of motion for propelled, dissipative colloids, we found that near the phase boundary, the microscopic states from which collective motion develops are not free of orientational correlations, *i.e.* the assumption of *molecular*

chaos that is commonly applied in kinetic theory is not valid for propelled particle systems at the onset of collective motion. Most importantly, the ensuing correlations at the onset are—for the aforementioned system—a *qualitative* prerequisite for kinetic theory to predict a phase transition to collective motion at all. This conclusion was made possible by *quantitatively* connecting the details of the microscopic collision process with the mesoscopic kinetic description, in turn allowing for a *quantitative* test of the predictions of kinetic theory. If the aforementioned correlations are implemented into the kinetic approach, the prediction of kinetic theory for the phase boundary *quantitatively* coincides with the one obtained from the underlying microscopic Newtonian particle dynamics in the regime of low packing fractions.

Finally, an appropriate particle-based model for propelled particle systems at large packing fractions was analyzed in detail. Upon characterizing the degree of bond orientational and translational order, the following generic states were identified: An *unpolarized active crystal* state with long-ranged orientational and translational order, and a *polycrystalline* state, which coherently flows and is composed of hexagonal domains. It was shown that the underlying ordering transitions are defect-mediated.

Most of the results of this thesis exemplify the importance of a one-to-one comparison between theoretical models and experimental studies in order to advance our understanding of propelled particle systems. Rather than adopting a generic approach, the central goal of this thesis is to develop both a bottom-up modeling framework as well as an experiment-specific one. This formulation advances our understanding of the physics of two specific experimental propelled particle systems and hopefully will serve as a starting point for investigations of the dynamics in other active systems such as moving cells and bacteria.

Chapter 1

Introduction to Propelled Particle Systems

1.1 What is a Propelled Particle System?

For a system in *thermal equilibrium*, the probability of states is fully determined by *Boltzmann-Gibbs* statistics. This permits the calculation of macroscopic average quantities, such as energy or particle number. The ensuing fluctuations around these averages are Gaussian distributed with the width solely given by the temperature and the system's susceptibilities. The assumption of local thermal equilibrium allows the concepts of Boltzmann-Gibbs to be extended to a class of hydrodynamic non-equilibrium systems and has been effective in predicting patterning dynamics on large length and time scales. Paradigms for this broad class of pattern forming, non-equilibrium systems are the *Turing* [102] and *Rayleigh-Bénard* setup [27].

However, *in-vivo* biological systems such as living cells [62, 94, 92] and bacteria [32, 110, 78] eschew any description that relies on thermal equilibrium. In these systems, the constituents consume energy that is converted into forces acting *locally* on the scale of the individual particle. Specifically, the direction (and amplitude) of these forces are determined by an *inherent polarity* of each particle, *e.g.* the long axis of a rod-like bacteria with a distinct front and rear. The fact that the forces are local and depend on the particle's polarity defines the aforementioned systems as members of the class of **propelled particle systems** [9, 81, 106, 65]. The ensuing particle motion is characterized by large distances (typically several particle diameters) of rather persistent trajectories, only interrupted by slight reorientation events due to fluctuations¹. This particle motion is commonly referred to as a *persistent random walk*².

Even though biological systems like cells and bacteria are undoubtedly of high relevance and interest in biological physics, probing their physics often involves complications:

¹Examples are interactions with the substrate, thermal fluctuations, fluctuations of the propelling mechanism due to *e.g.* the limited availability of “fuel”, etc.

²In general, orientation and speed can fluctuate in the case of a persistent random walker [77].

Several highly complex and unknown types of interactions in addition to repulsion and adhesion exist between the constituents, such as chemotaxis, or non-linear and non-trivial responses to stresses (pressure, temperature,...) determined by all internal degrees of freedom (*e.g.* involving all molecules and fibers in a cell). Forming an understanding of these propelled particle systems requires disentangling certain physical phenomena. This can be reached by considering only a few subparts of the actual *in-vivo* system (*e.g.* a few constituents,...), leading to the development of *in-vitro*, reconstituted systems. In these systems, interactions between the propelled particles are mostly known and usually only a few different particle species are used. Motility assays consisting of purified proteins such as molecular motors and bio-polymers [21, 90, 89, 93] are examples of reconstituted, propelled particle systems. Another line of attack is to build on the experience of the granular physics community and shake man-made *mm*-sized solid objects [18, 71, 10, 58, 30, 91, 31].

The class of propelled particle systems (*in-vivo* and *in-vitro*) gives rise to a variety of fascinating self-organization phenomena ranging from the emergence of phase-segregated clusters [5, 8], to patterns of characteristic size such as asters and vortices [32, 18, 10, 58, 110], to collectively moving swarms [30, 31, 90]; see Fig. 1.1 for a selection of intriguing patterns observed in propelled particle system. Moreover, all propelled particle systems share several unifying features:

- (i) *inherent polarity* of the constituents,
- (ii) *persistent* trajectories,
- (iii) an interaction that breaks (on average) rotational-symmetry (*“ferromagnetic” alignment*),
- (iv) a *density-dependent transition* to an ordered collectively moving phase with various kinds of patterns, such as waves, swirls or clusters,
- (v) huge fluctuations in the particle density in the ordered phase, referred to as *giant number fluctuations*³.

These similarities suggest universal organizing principles underlying the dynamics and the ensuing pattern formation in these systems. Typically, theoretical models on all levels of description are inspired by this universality. The “Swiss Army knife” of models for propelled particle systems is the so-called *Vicsek-model* [105] and will be detailed throughout the next section.

³In order to measure number fluctuations, a *e.g.* quadratic domain of linear size L_{box} is divided into M^2 sub-boxes of linear size L_{box}/M . For each size, the average particle number $\langle N \rangle$ and standard deviation $\Delta N := \sqrt{\langle N^2 \rangle - \langle N \rangle^2}$ is calculated. Equilibrium systems lead to $\Delta N \propto \langle N \rangle^\delta$ with $\delta = 1/2$. Fluctuations are termed as *giant* if $\delta > 1/2$.

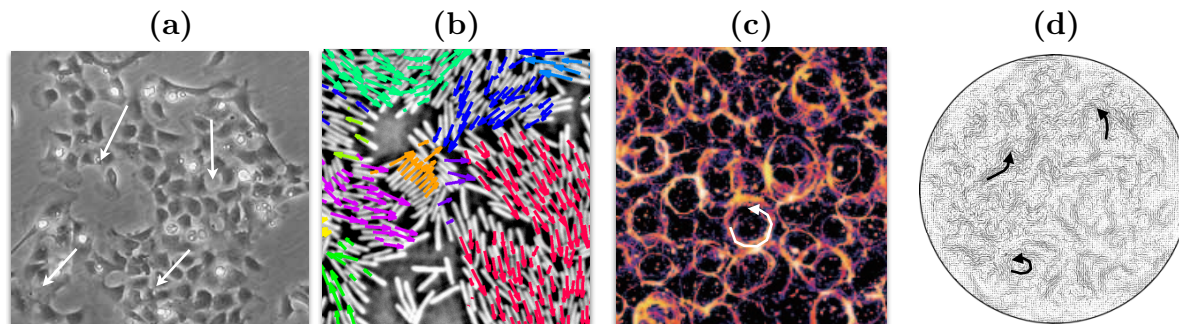


Figure 1.1: *Patterns in propelled particle systems*: (a) Coherently moving keratocyte cells [94], (b) swarming wild-type *Bacillus subtilis* [110], (c) large-scale vortex lattice emerging from collectively moving microtubules [93], and (d) swarming and swirling granular rods on a vibrating dish [58]. Coherently moving groups/regions are depicted by arrows.

1.2 Modeling Propelled Particle Systems — State of the Art

Historically, generic agent-based models [105, 29, 40] constitute the first theoretical approach aiming to understand the minimal ingredients necessary for the emergence of collective motion. Motivated by the question of how order can emerge spontaneously by means of simple local interactions among propelled constituents, Vicsek et al. [105] suggested the following principle: Collective motion is thought to be a consequence of a generic competition between a local tendency of “ferromagnetic alignment” and noise. Specifically, in their famous *Vicsek-model*, particle alignment is implemented as an update rule in the spirit of a cellular automaton: Each particle aligns parallel to the average of all particles’ orientations within some defined finite neighborhood. The central result is that propelled particle systems with “ferromagnetic alignment” interactions and noise can give rise to a *long-range ordered* state of coherently moving constituents; a state with broken rotational symmetry, or in brief a “polar state”. The phase transition to the polar state requires large enough particle densities or, equivalently, low enough noise strength.

Moreover, Vicsek-like models have been instrumental in exploring the pattern forming capabilities of propelled particle systems [105, 28, 29, 40, 22, 23, 11]: Analyzing the patterning dynamics in time shows that localized coherently moving units emerge in the very beginning. These units, commonly termed ‘clusters’, grow in size by successively taking up surrounding particles and aligning them to the horde. This effect is reminiscent of a “vacuum cleaner”, which leaves a depletion zone around the growing clusters, making it even easier⁴ for them to assimilate further particles. The ensuing coarsening process leads

⁴Note that reorientations of a cluster only occur if colliding particles significantly alter the average orientation of a “cluster particle’s” neighborhood, which is rather unlikely when single particles from the depletion zone collide with a dense (“self-stabilized”) cluster.

to clusters typically elongated along their average direction of motion [see Fig. 1.2].

The long-time dynamics of the system can be summarized in a density–noise phase diagram depicting the stationary phases that develop in Vicsek-like models. The phase diagram is comprised of a disordered region with *isotropic* particle orientations and a *polar* ordered regime with a stationary mean flow velocity [see Fig. 1.3]. Within the ordered region of the density–noise phase diagram, one finds polar states with two different spatial arrangements of the particles, namely a *homogeneously* distributed state and a coherently moving *wave-like* pattern. The latter solely exists close to the phase boundary, or in other words, crossing from the *isotropic* region to the homogeneously distributed polar phase, there are always states comprised of wave-like patterns in between. Finally, in a polar state that is homogeneously distributed, Vicsek-like models exhibit *giant number fluctuations*, with a scaling coefficient $\delta \approx 0.8$ ([23], and see footnote³).

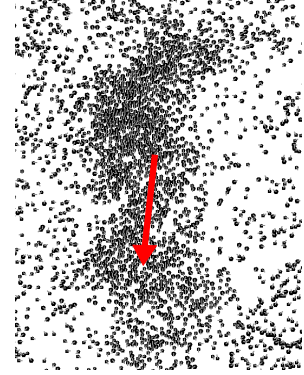


Figure 1.2: Elongated cluster at the very beginning of the dynamics.

Comparing the experimentally observed patterns [Fig. 1.1] with the phases found in Vicsek-like models [Fig. 1.3] it is apparent that real systems do *not* develop states with *long-range* polar order. Instead, real systems create coherently moving structures of finite size, which, using the standard terminology for phase transitions [69, 49, 68, 57, 48], would fall into the category of short-range order (or isotropic on large scales). The reason for this discrepancy could be the fact that every experimental system is finite, hindering the growth of long-wave length modes in the system. However, to understand the underlying principles for the emergence of collective motion in real (experimental) systems, one must go beyond simplistic Vicsek-like models by introducing certain system-specific features into the modeling framework. Examples for potential modifications of Vicsek-like models are including the actual shape and physical properties of the experimental boundary, or, accounting for further interactions between the constituents, such as adhesion or repulsion. Note that the original Vicsek model deals with point-like particles, neglecting the impact of particles' excluded volume. Only a few studies exist that included the particles' excluded volume [22, 40, 41, 74, 107, 76, 67, 17, 66, 46, 108]. Further extensions of the Vicsek model could concern the explicit treatment of the surrounding solvent. Finally, it is tempting to understand the impact of inertia by investigating the pattern formation in propelled particle systems in terms of Newtonian equations of motion involving explicit forces for propulsion, dissipation and interaction [63, 37, 36, 75, 34, 64, 42, 84, 43, 83]. In this thesis, several distinctly different particle-based models are proposed, which are built on or at least inspired by Vicsek-like models, but aim to unravel the essential new ingredients necessary to reproduce the observations and findings of several different experimental systems within the field of propelled particles.

Additionally, there are analytic approaches to quantify the phase transition and understand the pattern formation in propelled particle systems, namely hydrodynamic approaches and kinetic theory. On the one hand, hydrodynamic equations were constructed

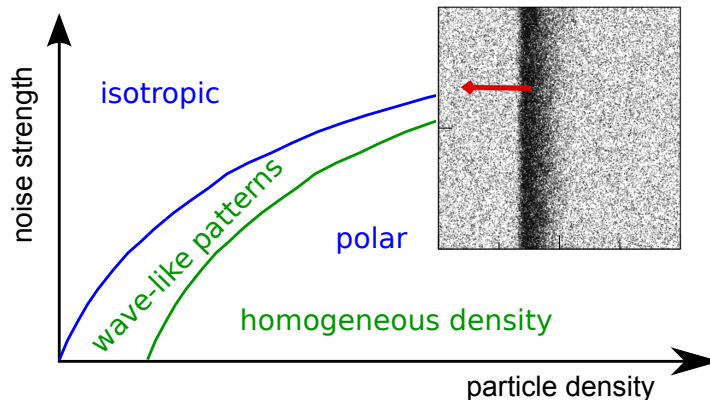


Figure 1.3: *Density-noise phase diagram* for Vicsek-like propelled particle systems: For large noise strength or small particle densities, the overall state is *isotropic*. Increasing density/decreasing noise leads to a transition to an ordered *polar* phase (divided by blue lines), which is in turn comprised of regions with either *wave-like patterns* or a *homogeneous density*. An example of a wave-like pattern found in the Vicsek-model is depicted at the top right (taken from [23]).

based on conservation laws and symmetry arguments [96, 97, 101, 1, 82, 98, 39, 95], and analyzed by means of a one-loop dynamic renormalization group calculation. It was proven that collections of self-propelled particles can exhibit a true, long-range ordered, spontaneously broken symmetry state. Moreover, this approach predicted anomalously large density fluctuations, referred to as *giant number fluctuations* and allowed the calculation of the scaling coefficient $\delta = 0.8$, which is in agreement with the findings in Vicsek-like models.

On the other hand, hydrodynamic equations for propelled particle systems were derived by kinetic models, directly based on mesoscopic collision rules [7, 15, 6, 16, 51, 80, 79], or on microscopic interactions [85, 86, 13, 12, 70]. However, to keep calculations feasible these approaches neglect higher-order correlations and are formulated for the one-particle density. This restricts their application to systems with interactions dominated by binary particle encounters, *i.e.* dilute particle densities. However, as opposed to symmetry based hydrodynamic approaches, which involve a vast number of *unknown* coefficients (*e.g.* the viscosities), these coefficients are known in kinetic approaches allowing for quantitative predictions of the ordering transition. More details on kinetic theory including its quantitative predictions are discussed in section 2.3.2. There will be a separate part of this thesis, which is devoted to extensions of kinetic theory for propelled particle systems in order to appropriately account for recent qualitative experimental and numerical observations in propelled particle systems.

1.3 Outline

This thesis essentially consists of two parts⁵:

(A) The first part (section 2.1 and section 2.2) deals with *specific*, particle-based modeling approaches for two experimental *in-vitro* systems within the field of propelled particle systems: The *actin gliding assay* and the *vibrated polar disk setup*.

(B) The second part (section 2.3 and section 2.4) is devoted to the extensions of kinetic theory for propelled particle systems as well as *generic* particle-based modeling approaches, presenting several new hallmarks within the field of propelled particle systems.

⁵Due to the large amount of considered quantities in this thesis, the notation of variables is independent for each of the four sections, 2.1 to 2.4.

Chapter 2

Modeling Propelled Particle Systems

In the following two sections, 2.1 and 2.2, two experimental paradigm systems within the field of propelled particle systems are introduced, and the corresponding modeling approaches are discussed. Section 2.3 is devoted to the analysis of generic models for propelled particle systems under dilute conditions, while section 2.4 deals with phenomena occurring in dense packing of propelled particles.

2.1 The Gliding Assay – A Paradigm for *in-vitro* Active Systems

Three components are required to build a gliding assay [50, 109, 99, 103, 100, 44, 104, 19, 38]: Molecular motors, filaments and a planar surface (“coverslip”). Molecular motors are nanometer-sized machines that can exert forces by the consumption of energy through hydrolyzing adenosine-tri-phosphate (ATP) to adenosine-di-phosphate (ADP)—the standard “bio-fuel” for cellular processes. In the gliding assay, these motors, consisting of a molecular “head” and “tail” region, are immobilized upon a planar surface by their tails. With the “head” region they can bind to nearby filaments, *e.g.* actin or microtubules, which are commonly purified from muscle or cell extracts. These filaments exhibit an intrinsic polarity directed tangentially along the filament contour, determining the direction along which the molecular motor can exert forces locally. This leads—even for several “working” motors—to a perpetual transport of filaments within the gliding assay. The driving that couples locally on the filament’s contour with a well-defined intrinsic polarity, makes the filaments on the gliding assay a **propelled particle system**. For an illustration of the gliding assay, please refer to Fig. 2.1.

The binding chemistry of molecular motors is in general complex and specific. For all later studies, we will deal with *heavy mero-myosin* (HMM) [50] as the molecular motor and *actin filaments*. For the convenience of the readers, a description of the most important properties of *HMM molecular motors* and *actin filaments* are given below:

The binding cycle of the *HMM motor* involves three crucial steps¹: (i) The cycle starts with a time period (denoted τ_h), where the motor is bound to the filament providing a link between the planar substrate and the filament. Therefore, this is referred to as “Hold” state. (ii) In the subsequent *power-stroke* phase the motors exert forces parallel to the filament contour within a very short² time period τ_s . The corresponding state is short-handed “Push” in the following. (iii) Finally, the motor detaches, and its head region remains inaccessible for further binding events for a long time period, denoted τ_{off} . After that, the cycle starts again from the beginning. A sketch of the binding cycle for HMM is depicted in Fig. 2.1.

Actin filaments are semi-flexible polymers with an aspect ratio of 1000:1. The typical length of the filament ranges in the order of $10\mu m$ and the diameter is about $10nm$. Each filament can be viewed as a two-stranded (right-handed) helix with the strands wrapped around each other with a repeat period of about $70nm$ [50] [see Fig. 2.1]. In turn, each strand consists of monomers with a size of about $5nm$. A more coarse-grained but adequate picture for our later theoretical description can be constructed by treating actin as a single stranded polymer with a diameter of about $10nm$. Finally, since the thermal persistence length for actin $\ell_p = 17\mu m$ [24, 50] is about the typical filament length, the actin filament constitutes a semi-flexible polymer with respect to Brownian fluctuations.

The following three sections will deal with experimental investigations and corresponding modeling approaches for the actin gliding assay. Specifically, section 2.1.1 focuses on the origin of anomalous, non-thermal contour fluctuations of single actin filaments. Section 2.1.2 is devoted to the gliding assay at high filament densities finding the emergence of coherently moving states with complex spatio-temporal patterns. Finally, by only adding a single type of molecule, namely crosslinking molecules, the system’s dynamics at high filament densities is altered severely, leading to “frozen” ring-like structures (see section 2.1.3).

¹Recently, it turned out that there could also be a further short time-period step in the HMM cycle, called the “after-stroke” [3, 2]. For the presented approaches, however, we neglected this new phase due to the limited amount of available data and the fact that this “second step” for Myosin-II is so fast that it could not be detected in the experiments by direct measurements.

²Typical values are: $\tau_s \sim 10^{-4}s$, $\tau_h \sim 10^{-3}s$ and $\tau_{off} \sim 5 \cdot 10^{-2}s$ (*e.g.* [50] and references therein).

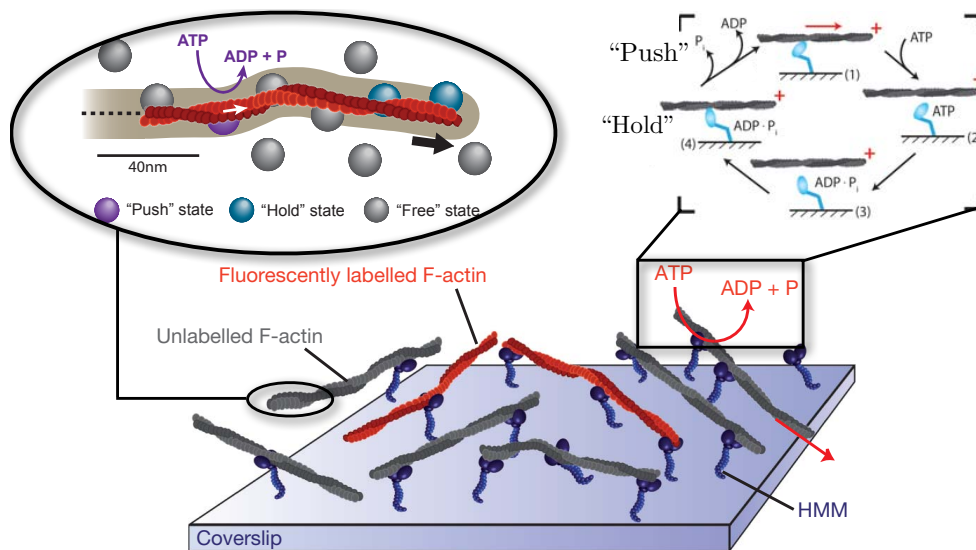


Figure 2.1: *Illustration of the gliding assay:* Actin filaments are depicted in red/grey. HMM motors shown in blue are fixed on a planar surface. Only some of the filaments are labelled [“labelled” (“unlabelled”) filaments are depicted in red (gray)] in order to increase the contrast of density heterogeneities for the microscope (only necessary for large filament densities). By hydrolysis of ATP to ADP, these motors can bind to the filament with a certain relative distance and propel the actin filaments forward due to the intrinsic polarity of the filament (top left). The motor passes through a rather complex cycle including the “Hold” and ‘Push” states, which is depicted at the top right (for explanation see text; sketch courtesy of Volker Schaller).

2.1.1 Anomalous Contour Fluctuations

Throughout this section we will consider the gliding assay with highly *dilute* filament densities and intermediate motor surface densities $c \approx 1.5 \cdot 10^3 \mu\text{m}^{-2}$. In this case, filament-filament interactions are extremely rare.

However, running the gliding assay at these *dilute* conditions, we found various kinds of filament configurations, ranging from smoothly bent shapes to configurations with rather strong pronounced *kinks* in the contour [Fig. 2.2(a–c)]. The filaments are approximately of length $L = 8 \mu\text{m}$, with the kinks occurring on a length scale on the order of $1 \mu\text{m}$. For a thermally fluctuating polymer with a thermal persistence length larger or on the order of the filament’s length ($L \lesssim \ell_p$), large curvature events [Fig. 2.2(a,b)] should be very unlikely and occur with a probability proportional to $\exp(-\kappa^2/2\ell_p^2)$ [24, 50], with κ denoting the local curvature along the polymer contour. Any deviation from these statistics would indicate a *non-thermal influence* on the fluctuations of the actin filament’s contour. In order to study the curvature statistics of the filaments, we discretize the polymer contour into segments and extract the local curvature values κ for each segment. The corresponding curvature probability distribution clearly shows an anomalous tail [Fig. 2.3(a)], *i.e.* large

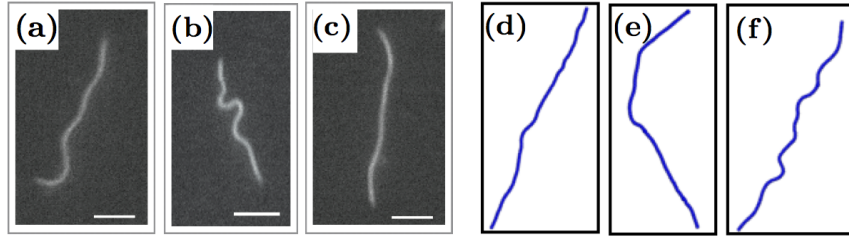


Figure 2.2: Snapshots of typical filament configurations observed in the experiment (a)-(c), and found in the stochastic simulation (d)-(f). Scale bar: $2\mu m$.

curvature events are distributed exponentially. The Gaussian core in the distribution for small curvatures indicates the residual impact of the thermal bath on the actin filament, whereas the excitation of curvature that results in anomalous strong kinks can only be related to the interactions between filaments and molecular motors.

To form an understanding of how motors give rise to these anomalous events, we study the following stochastic model for a propelled actin polymer (for details, refer to Appendix C): Each filament has a length L and diameter d . We account for the bending stiffness of the actin filaments, which in the presence of thermal fluctuations is solely characterized by the ratio between the persistence length ℓ_p and the filament length L . The interactions between the filament and the molecular motors on the two dimensional substrate is modeled as a process of stochastic and independent binding events of motors along the filament contour. For the binding cycle of the motors, we employ the aforementioned simplified picture of “Push” and “Hold” as being the two essential states [Fig. 2.1(a)]. A motor begins its cycle with the “Hold” state by binding to the filament. We assume that the motor attaches randomly at a certain segment of the filament with a probability $[\text{number of segments}]^{-1}$, independent of the binding history or state occupancy of a segment. After attaching to the filament, the motor acts as a rigid link between the substrate and the filament for a period of time τ_h (holding time) if the displacement of the attached filament segment is beyond a certain critical distance l_c . Otherwise, the force exerted on the segment is zero³. We assume that the critical length l_c is essentially determined by the average length of the tail of the HMM motor, which is in the order of $40nm$. After the holding time period, the molecular motor is modeled as a spring that is connected to the filament and moves with a velocity $\Delta x_s/\tau_s$ (Δx_s denotes the stroke length) during the stroke time τ_s along the filament’s local tangent. Subsequently, the stochastic binding cycle starts again. Along the filament’s contour, the total number of attached motors, denoted m_b , is chosen to be constant in time. The number of bound motors can be estimated from the experimental surface density by $m_b \approx c(d_a + 2l_c)LD$, where $d_a \approx 10nm$ is the diameter of an actin filament. The quantity D denotes the duty ratio and accounts for the fact that HMM is a non-processive motor [50]. It is defined as the ratio between $(\tau_s + \tau_h)$ to the time required for the motors to bind to the filament again. Measurements for HMM have

³In other words: Say a motor with coordinates \mathbf{R}_m is bound to a filament segment with coordinates \mathbf{R}_s , there is only a force if: $|\mathbf{R}_s(t) - \mathbf{R}_m| > l_c$.

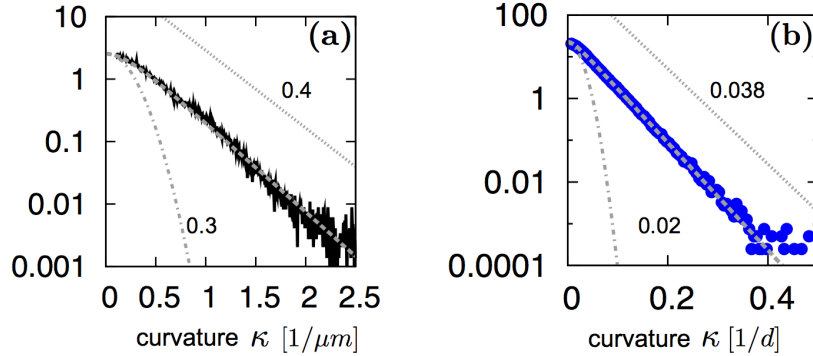


Figure 2.3: *Curvature probability distribution* $P(\kappa)$: **(a)** For the *experimental setup* with the control parameters of motor density $c = 1.5 \cdot 10^3 \mu\text{m}^{-2}$ and filament length between $4\text{-}8\mu\text{m}$. **(b)** For the *stochastic model* with parameters: $m_b = 30$, $\ell_p = L$ and $L = 100d$. Solution to Eq. (2.1) using the constitutive relations for λ and D_κ [see Eq. (2.2)] is indicated by gray dashed lines. An exponential distribution is indicated by a dotted line with the slope value, and a Gaussian distribution by a dashed-dotted line with the value of its standard deviation. Multiplying the corresponding characteristic values for experiment and model by filament length is in approximate quantitative agreement.

estimated this ratio to be $D \approx 1/50$ [50], which leads to an approximate value of $m_b = 30$ for a typical surface density $c = 1.5 \cdot 10^3 \mu\text{m}^{-2}$.

Running the model for $L \approx \ell_p$ and $m_b = 30$, we observe very similar filament configurations as in the experiments, including the anomalous non-thermal local curvature events [Fig. 2.2(d-f)]. Analyzing the curvature statistics in the simulation, we also find that for decreasing curvature values, the exponential anomalous tail transitions to a Gaussian core [Fig. 2.3(b)]. To further examine the validity of the model, we studied the impact of the control parameters such as filament length L and motor density m_b in the experiment as well as in the model. We find that length in experiment and model has no essential impact on the curvature PDF $P(\kappa)$ [Fig. 2.4(a,b)]. This observation disproves thermal bending relaxation of large curvatures as a central determinant of the filament dynamics, because the relaxation time of semi-flexible polymers exhibit a strong dependence on the filament length [50]. However, increasing the motor density c in the experiment, or equivalently m_b in the model, results in the slope of the distribution tail to increase monotonically, both for the experiment and the model. These observations clearly show that the molecular motors contribute to the majority of the elastic energy in the filament ($\propto \int_0^\infty d\kappa \kappa^2 P(\kappa)$), whereas the contributions of the thermal bath only plays a role for very small curvatures. This raises a question: *Can we understand the origin of anomalous curvature events, i.e. excitation and relaxation of curvature?*

To this end, we describe the mesoscopic impact of motors on the actin filament by means of a simplified kinetic equation for the stationary curvature distribution $P(\kappa)$. By analyzing the stochastic model on the smallest time scale, *i.e.* the stroke time τ_s (which is not accessible in the experiment) we are led to the following microscopic principle for

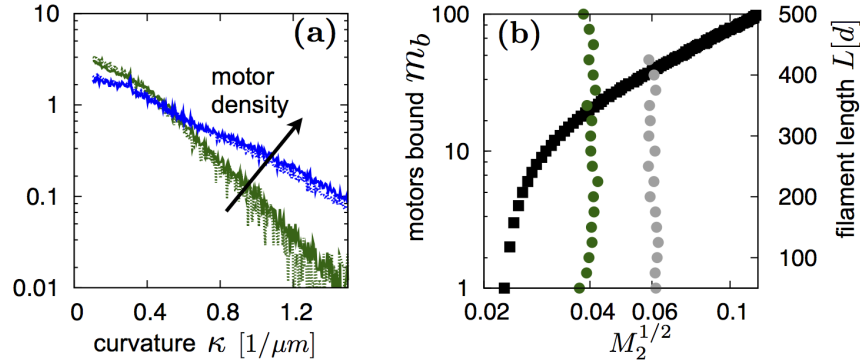


Figure 2.4: (a) *Experimental curvature probability distribution* $P(\kappa)$ for two different motor densities (green: $c = 10^3 \mu\text{m}^{-2}$; blue: $c = 5 \cdot 10^3 \mu\text{m}^{-2}$) and two different filament length intervals (dotted: $1\text{-}4\mu\text{m}$; solid: $4\text{-}8\mu\text{m}$). (b) *Square root of second moment of curvature distribution in the model*, denoted as $M_2^{1/2}$ for varying number of bound motors m_b (indicated by black solid squares; $L = 100$) and different filament length L (green and grey solid circles correspond to $m_b = 20$ and $m_b = 40$, respectively).

curvature build-up in the filament bulk: A local configuration of motors with “holding” motors at the front and “pushing” motors at the rear leads to a local build-up of curvature [Fig. 2.5]. Then, there are two general scenarios: (i) A similar configuration of motors leads to the emergence of anomalous large curvature events, while (ii) a reversed configuration with “pushing” motors at the front and “holding” motors at the rear flattens the established curvature. Our mesoscopic kinetic equation for $P(\kappa)$ will exactly account for these two scenarios. Specifically, we model the curvature build-up as a diffusion process with a diffusion constant D_κ depending on the motor density m_b . Moreover, the flattening process is assumed to be composed of discrete events occurring with rate λ , which decreases the curvature according to $\kappa/\eta \rightarrow \kappa$, with $\eta < 1$ characterizing the strength of the flattening process⁴. The resulting equation is then the following [56, 45, 92]:

$$0 = D_\kappa(m_b)\partial_\kappa^2 P(\kappa) + \frac{\lambda}{\eta}P(\kappa/\eta) - \lambda P(\kappa). \quad (2.1)$$

Rescaling the equation above by $\kappa \rightarrow \kappa/\sqrt{D_\kappa\lambda^{-1}}$, the moments $M_n = \int d\kappa \kappa^n P(\kappa)$ can be computed from the corresponding recursion relation $M_n = n(n-1)(1-\eta^n)^{-1}M_{n-2}$, leading to $M_{2n} = (2n)! \prod_{k=1}^n [1-\eta^{2k}]^{-1}$. From this equation the limit $\eta \rightarrow 0$ can be easily performed, leading to all even moments $M_{2n} = (2n)!$, which are equal to those of an exponential function in $\kappa \in [0, \infty)$. In particular, the normalized fourth moments yields $M_4/M_2^2 = 6$.

⁴The coefficient κ also determines the amount of energy dissipated relative to the energy input set by the curvature diffusion constant D_κ . Since the elastic energy of the filament scales as $\propto \kappa^2$ and $\kappa \rightarrow \eta\kappa$, the elastic energy scales as a function of η also as $\propto \eta^2$. Therefore, $1-\eta^2$ is the ratio of energy that is dissipated.

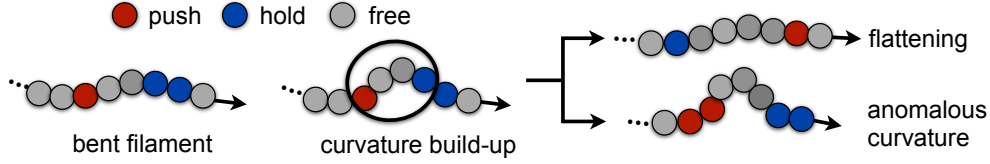


Figure 2.5: *Illustration of the principle for curvature build-up*: Brownian fluctuations create a slightly bent filament contour, while the jam created by holding motors at the filament’s front and pushing motors at the rear leads to a local build-up of curvature. Similar motor configurations can then create *anomalous* curvature events, while a reversed configuration flattens the contour.

In the limit $\eta \rightarrow 1$, the procedure is a bit more intricate: The even moments, given by⁵ $M_{2n} = (2n - 1)!!(1 - \eta)^{-n}$, diverge in this case. Even though not directly obvious from Eq. (2.1) the given singularity explains why setting $\eta = 1$ in Eq. (2.1) is not well-defined. However, the limit $\eta \rightarrow 1$ can be accomplished in Eq. (2.1) by expanding $\frac{1}{1-\epsilon}P(\kappa/(1-\epsilon))$ into a Taylor series around $\epsilon = 1 - \eta = 0$, yielding: $P(\kappa) + [P(\kappa) + \kappa P'(\kappa)]\epsilon + \mathcal{O}(\epsilon^3)$. Plugging this series into Eq. (2.1) leads to a Gaussian distribution as a solution, $P(\kappa) \propto \exp(-\epsilon\kappa^2/2)$, with κ denoting the rescaled curvature $\kappa \rightarrow \kappa/\sqrt{D_\kappa\lambda^{-1}}$. The Gaussian limit for $\eta \rightarrow 1$ also becomes obvious when considering the fourth normalized moment as a function of η , which is given by $M_4/M_2^2 = 6/(1 + \eta^2)$. This leads to $M_4/M_2^2 = 3$ for $\eta \rightarrow 1$, which is exactly the value expected for a Gaussian distribution. Taken together, $\eta \rightarrow 0$ lead to an exponential curvature distribution, whereas the limit $\eta \rightarrow 1$ corresponds to a Gaussian.

Moreover, the formula above for M_4/M_2^2 allows us to eliminate η as an unknown parameter by measuring the fourth normalized moment from the experimental and model PDF $P(\kappa)$. Consequently, Eq. (2.1) has only two unknown parameters, namely the curvature diffusion constant D_κ and the rate of the flattening events λ .

Following our aforementioned picture of the microscopic origin for curvature build-up, we assume that the rate of the flattening events λ is primarily given by the larger time-scale⁶, namely the holding time of the molecular motors τ_h^{-1} . To account for minor deviations to this assumption, we write $\lambda = \frac{\gamma_h}{\tau_h}$, with γ_h a dimensionless number $\mathcal{O}(1)$.

Now, we construct a constitutive equation for the curvature diffusion constant $D_\kappa(m_b)$ that includes thermal fluctuations characterized by the persistence length ℓ_p , along with the impact of the molecular motors, *i.e.* a dependence on the number of working motors. An increasing average number of working motors, given by $\frac{\tau_s}{\tau_h}m_b$ [m_b : number of bound motors], is thought to result in a larger curvature diffusion constant D_κ . We simplify this monotonic increase by a linear dependence. Furthermore, we assume that the time-scale related to this diffusion process is given by the stroke-time τ_s , with γ_s again some dimensionless number $\mathcal{O}(1)$ accounting for minor deviations to this assumption. This yields the following constitutive equation for a curvature diffusion constant with a dimension

⁵The double factorial is defined as: $(2n - 1)!! = \prod_{m=1}^n (2m - 1)$.

⁶So far we did not find a really convincing argument that $\lambda \sim \tau_h^{-1}$. However, this assumption leads to excellent predictions for the curvature scale for the experiment and the numerical model.

[1/(time \times length²):

$$D_\kappa(m_b) = \frac{1}{\ell_p^2} \left[1 + \delta \frac{\tau_s}{\tau_h} m_b \right] \frac{\gamma_s}{\tau_s}, \quad (2.2)$$

where δ measures the relative impact of a single working motor on D_κ compared to thermal fluctuations. We consider this impact to be given by the relative amount of work a motor exerts on a filament relative to its thermal energy. For a filament with $L \approx \ell_p$, the corresponding energy content is about $1k_bT$, whereas a single motor exerts a work also of approximately $1k_bT$ (force $\sim 1pN$, stroke displacement $\sim 10nm$, refer to *e.g.* [50]). Consequently, we estimate $\delta \approx 1$.

By means of the constitutive equations for λ and D_κ , the solutions of the kinetic equation (2.1) can now be quantitatively related to the curvature PDF of both, the experimental assay and the numerical model, by rescaling the curvature as $\kappa \rightarrow \kappa/\sqrt{D_\kappa\lambda^{-1}}$. Note that only the ratio between the time-scale for stroke and holding time matters for the curvature scale. We find that $\frac{\gamma_s}{\gamma_h} \approx 1$ in order to reproduce the PDFs quantitatively for both model and experiment. The corresponding results are given by the gray dashed lines in Fig. 2.3(a,b), showing an excellent agreement between the kinetic model with the PDF obtained for the model and experiment, thereby proving at least the approximate validity of the constitutive equations for $D_\kappa(m_b)$ and λ .

We conclude that the mesoscopic impact of the molecular motors on the curvature distribution of the filaments $P(\kappa)$ is twofold: Although motors effectively increase the polymer's temperature ($\propto D_\kappa$), they give rise to anomalous flattening of the filament contour otherwise, thereby invalidating any approach for the actin gliding assay relying on thermal fluctuations [35] or “effective” temperature [60, 59]. Consequently, since the fluctuations originate from the motor–filament interactions we refer to those as *active fluctuations*.

In the next step, we plan to investigate the dynamical behavior of our active filaments by means of studying tangent-tangent correlations as well as the correlations in time of the end-to-end vector [61], and work out the deviation to thermally fluctuating, semi-flexible polymers. A manuscript of the presented results that also includes the results on the polymer's dynamics is currently under preparation (see **list of publications A**).

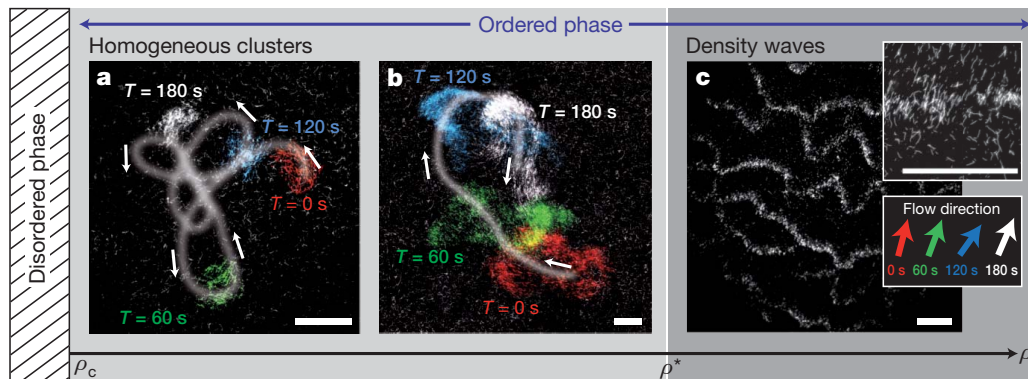


Figure 2.6: *Phase diagram for the gliding assay as a function of the filament density:* **a.** For low densities, a disordered phase is found with filaments “mostly” moving randomly. However, recent experimental investigations indicate the existence of weak orientational correlations (private communication with Ryo Suzuki). **b.** Above a certain critical density ρ_c small, homogeneous and polar clusters of coherently moving filaments start to form. At higher densities, these clusters become larger and move more persistently. **c.** Above a threshold density, ρ^* , in the high-density regime, wave-like patterns emerge. In **a** and **b**, the trajectory of the clusters is shown by a color-coded time overlays of their movements in time (white line). The movement of the small cluster in **a** has a low persistence length, $\sim 60\mu\text{m}$, while the cluster in **b** is larger and less prone to reorientations (persistence length $\sim 200\mu\text{m}$). The insets in **c** show a magnified view and a local analysis of the average flow direction. The density waves show only minor reorientations over the time period of several minutes. Scale bars: $50\mu\text{m}$.

2.1.2 Gliding Assay at *High* Filament Densities

Now we turn to the gliding assay with a larger number of filaments. For dilute filament densities, filaments move mostly randomly throughout the motility assay. However, increasing the filament density above a critical value, denoted as ρ_c , results in a transition to an ordered phase that is characterized by a plethora of different polar patterns, each comprised of coherently moving units at approximately constant speed [see Fig. 2.6, for further experimental findings please refer to **publication B.1**]:

a/b: In an intermediate-density regime directly above ρ_c , moving clusters (swarms) of filaments appear [Figs. 2.6a and 2.6b].

c: Moreover, in the high-density regime exceeding a second threshold density, denoted ρ^* (about $20\text{ filaments}/\mu\text{m}^2$), propagating waves start to form [Fig. 2.6c].

a/b: The clusters encountered in the intermediate state have cluster sizes ranging from about $20\mu\text{m}$ to more than $500\mu\text{m}$ in diameter. In general, clusters have an erratic motion with frequent reorientations of low directional persistence. The low orientational persistence affects the cluster’s shape but barely influences its temporal stability. The

cluster integrity is only affected if they collide with boundaries or encounter other clusters. Increasing the filament density in this intermediate regime not only yields larger clusters but also a more persistent cluster movement. Individual clusters spontaneously emerge from the dilute, disordered background and continually assemble and disassemble filaments. In the absence of cluster-cluster interactions this uptake and loss dynamic is balanced and leads to cluster sizes that are stable for several minutes.

c: A further increase of filament concentration above ρ^* results in density waves characterized by correlated movement of high-density regions. In this high-density regime, the filaments move predominantly in bands that are stable throughout the observation time (up to 30 min). The bands exceed the size of their constituents by up to three orders of magnitude, almost spanning the entire system and forming crescent-shaped substructures. The appearance of the bands is a generic feature of the high-density motility assay. Whereas filaments in the high-density regions move collectively with high orientational persistence, filaments lying outside the bands perform persistent random walks (“disorder sea of filaments”). The system is less sensitive to other control parameters, such as the ATP concentration or the filament length.

Assuming that the interactions between the filaments are short-ranged, a fascinating question is: *How do the interactions between the constituents give rise to the emergence of these wave-like patterns?*

To give a first approximate answer, we developed an agent-based simulations accounting for the probabilistic movement of the filaments in presence of interactions. The agents are finite-length filaments, each performing a persistent random walk with a persistence length approximately equal to the actin filaments. Moreover, we assume that filaments interact via weak repulsion as well as weak local “ferromagnetic” alignment. Weak repulsion arises due to the fact that the gliding assay is just a *quasi* two-dimensional system: Filaments frequently cross each other (“indifferent event”). However, in between, one observes polar-alignment events; see Fig. 2.7 for some exemplary trajectories at diluted filament densities (left: parallel alignment event, right: indifferent event; pre-/post-collision state is depicted top/bottom). In the simulations, the symmetry-breaking nature of the local “ferromagnetic” interactions is crucial: Without it, filaments interact only sterically and do not show collective motion at all. More details on the simulation as well as the corresponding results can be found in **publication B.1** or section 2.3.1, where the same model is used to discover a new feature on the nature of the phase transition in propelled particle systems. However, here, the most important results are that for filament densities above some critical density, polar wave-like patterns emerge [see Fig. 2.8].

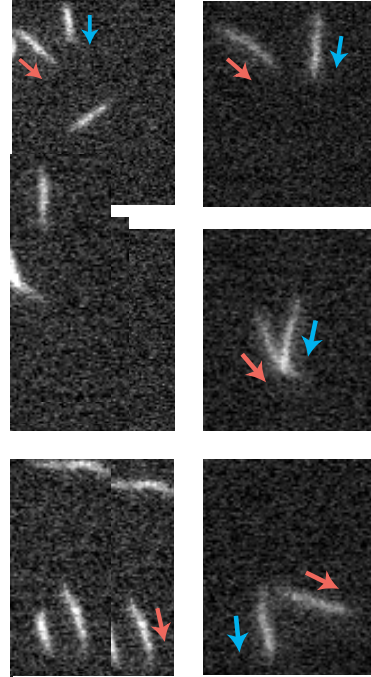


Figure 2.7: Filament collisions (courtesy of Ryo Suzuki).

This phenomena is rather robust against variations of parameters (alignment strength, density, etc.), as long as the density is above the threshold for collective motion. Interestingly, the same phenomenology—wave-like patterns—has also been found for more generic, agent-based models for spheres, called the Vicsek model (see *e.g.* section 1.2 or [22, 40, 23]). There, each particle aligns polar to the average orientation calculated over all particles within some finite neighborhood. As opposed to these generic agent-based models, our model explicitly incorporates filament length. Further, it matches the persistence of the ensuing random walk in the absence of interactions and accounts for weak repulsive interactions. Therefore, it constitutes undoubtedly a more realistic model for the gliding assay at large filament densities. However, the emergence of wave-like patterns seems to be a rather generic phenomenon. From this we concluded that the essential mechanism for the patterning instability in the gliding assay are *local* symmetry-breaking (“ferromagnetic”) interactions.

However, a more refined experimental study of the gliding assay revealed that hydrodynamic interactions play a crucial role in the later stages of the pattern forming process (see **publication B.2** for details). We found that the approximately two-dimensional collectively moving patterns induce a back-flow in the overlying fluid, which has been suggested by preliminary *Finite-Element simulations* [see Fig. 2.9]. By means of appropriate shear flow experiments this back-flow was shown to be strong enough to influence the movement of nearby coherently moving structures. Interestingly, the hydrodynamic interactions are also crucial for a swarming cluster near a confining boundary: The cluster feels a repelling force away from the boundary without being in direct contact. Again, hydrodynamic interactions are assumed to be mediated by the solvent above the coherently moving structure.

One remark is in order: Apart from the fascinating patterns reminiscent of flocks of birds or schools of fishes, the motility assay also exhibits anomalous number fluctuations, called *Giant-number fluctuations*, and anomalous scalings in the corresponding correlation functions of the hydrodynamic fields. These were recently analyzed experimentally [87]. Astonishingly, all experimental measurements are in agreement with the corresponding theoretical predictions based on dynamical renormalization group theory [96, 97, 101, 95]. Taken together, since the gliding assay exhibits all the hallmarks of collectively moving systems, it can be regarded as a *paradigm* that deserves more attention and experimental studies to understand the physics of collective motion.

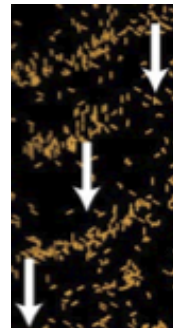


Figure 2.8:
Wave pattern in simulation.

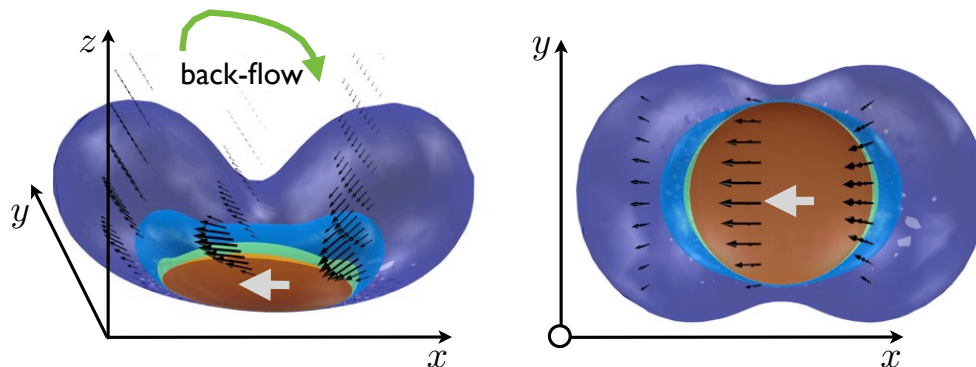


Figure 2.9: *Preliminary Finite-element simulations:* A swarming cluster is idealized as a rigid thin disk (height= 50nm , diameter= $50\mu\text{m}$), moving with a constant velocity of about $5\mu\text{m/s}$ in the x - y -plane (moving direction is indicated by gray arrow). For the simulations, we assume no-slip boundary conditions at the contact surface to the fluid surrounding. Left: side view; Right: top view. Black arrows depict the hydrodynamic flow field. Iso-velocity surfaces depict areas of constant flow velocity, with blue corresponding to $1/8$ of the moving velocity of the swarming cluster. The results clearly indicate that the moving “idealized” swarm gives rise to a notable back-flow, which is assumed to mediate the aforementioned hydrodynamic interactions between swarming clusters (see text).

2.1.3 Gliding Assay with Crosslinkers — Freezing of Activity

This section is devoted to the experimental study and a corresponding modeling approach for the gliding assay at large filament densities when adding a certain amount of *fascin crosslinking molecules*. Fascin is a so-called polar crosslinker, *i.e.* it only connects actin filaments in an approximately polar and parallel configuration [25], while filaments in orthogonal or even anti-parallel configurations are not affected by the crosslinkers⁷. These interactions mediate an ‘implicit alignment mechanism’ as they do not create explicitly aligned structures, however, parallel structures are stabilized. In the following we will investigate what happens to the patterning capability of the gliding assay at large filament densities when increasing the fascin concentration and we will discuss how we can understand the patterning pathway by an appropriate model. Let us first start with the experimental observations.

⁷The molecular binding mediated by the crosslinker is practically irreversible on the time-scales considered. However, non-thermal unbinding events (“forced-unbinding”) created by the molecular motors cannot be excluded; unfortunately, this is also hard to quantify at these large filament densities.

Experimental Observations: Emergence of *Frozen* Rings

Adding only a small amount of fascin does not change the pattern formation significantly⁸: Still, coherently moving structures such as clusters and density waves emerge, as discussed in the previous section [see also Fig. 2.10(a)]. This behavior drastically changes if the added amount of fascin added exceeds a critical concentration. The presence of crosslinkers leads to the emergence of rotating polar (mostly planar) actin-fascin structures, with a rotation speed of the rings of about $3\mu\text{m}/\text{s}$. While structure formation in the high-density motility assay relies on a balance between assembly and disassembly processes, the addition of crosslinker molecules inhibits the disassembly. This leads finally to a *quiescent* steady state where all filaments are firmly incorporated in constantly rotating rings [see also Fig. 2.10(b)] and where any orientational fluctuations on the single filament level are completely arrested (“frozen-in”). The absence of disassembly pathways makes the structure formation mechanism reminiscent of a coarsening process which ends up in an absorbing state [48]. In this kind of “frozen” steady state, rotating rings are homogeneously distributed throughout the motility assay and no preferred direction of rotation can be observed. Moreover, rings occur in two distinct conformations which are equally abundant: *open* and *closed* [see also Fig. 2.10(b)]. Closed rings consist of self-contained and constantly rotating actin-fascin fibers, while open rings also move on a stable circular trajectory with uniform curvature radius, as can be seen in a time overlay [see also Fig. 2.10(b)]. We measure the distribution of ring radii $P(r)$ in the steady state, which exhibits the following three characteristics [Fig. 2.10(c)]:

- (i) $P(r)$ shows a pronounced maximum at around $9.5\mu\text{m}$ which is of the order of the persistence length of individual filaments.
- (ii) Towards small curvature radii, the distribution is characterized by a cut-off radius of $\sim 5\mu\text{m}$, below which no rings are found.
- (iii) The decay of the distribution for large radii is of double exponential shape [see also Fig. 2.10(c)]. The double exponential nature of the curvature radii distribution is highly robust upon parameter variation and is conserved throughout variations of the fascin and actin concentrations, making this a generic feature of the system.

Analyzing the assembly dynamics in time of the open and closed rings allows us to identify the two following competing mechanisms for the formation of the two ring morphologies:

- *growth-stiffening*: Open rings seem to develop from strings (filament bundles of a few filaments⁹) that assemble by smaller strings approaching from the sides. This growth process seems to freeze the curvature of the string.

⁸Note that low fascin concentrations slightly dampen the inherent density fluctuations by crosslinking events but are not sufficient to completely inhibit them.

⁹Note that single filaments cannot be distinguished experimentally from bundles consisting of a few (say 5-10) actin filaments. Due to this limitation, we introduce the non-precise term: “string”.

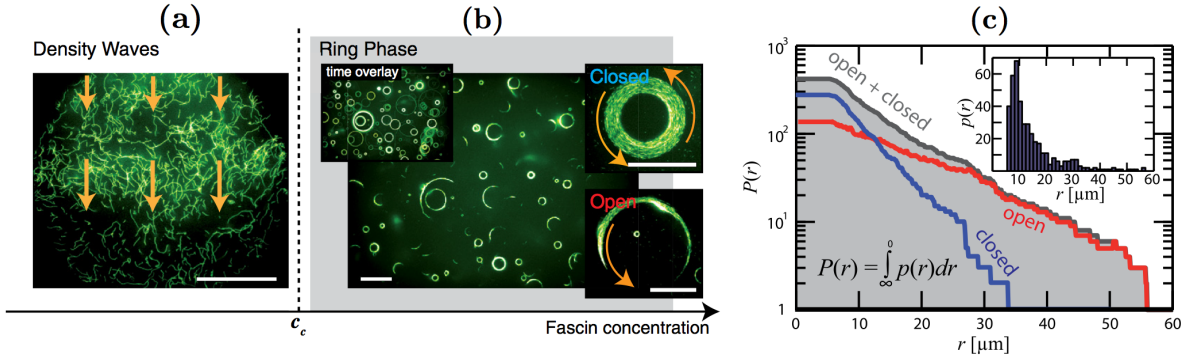


Figure 2.10: *Phase behavior as a function of the fascin concentration:* (a) Low fascin concentrations are not sufficient to significantly alter the pattern formation in the high-density motility assay and at an actin concentration of $\rho = 10\mu M$, the characteristic traveling density waves evolve. Compared to the case without crosslinkers, the density waves are less pronounced as the crosslinker slightly hinders the formation of density inhomogeneities. (b) Above a critical fascin concentration of $c_c \sim 0.075\mu M$, the pattern formation drastically changes as constantly rotating rings evolve that are either closed or open. In the steady state, all actin filaments are incorporated in rotating rings and fluctuations on the single filament level are absent. All scale bars are $50\mu m$. *Ring curvature distributions:* (c) shows the cumulative curvature radii distribution $P(r)$ in the frozen steady state; the inset depicts the noncumulative distribution. The distribution is comprised of two characteristic decays, each corresponding to either closed or open rings. These two different ring morphologies rely on distinct ring formation mechanisms that are related to the growth mechanisms in the system (see text for details).

- *ring-closure:* Closed rings typically¹⁰ emerge from self-closure of strings if they are long enough and the curvature is not yet frozen-in. While ring closure leads to predominantly small ring diameters, the *growth-stiffening* process naturally yields rings with larger curvature radii.

Modeling of *Freezing*

In the following, we aim to construct an appropriate model that reproduces the characteristics of $P(r)$ observed in the experiment [(i)-(iii)], and otherwise, includes the two competing mechanisms of *ring-closure* and *growth-stiffening*. To this end, we developed an agent-based model, where the experimentally observed actin-fascin strings are modeled as elongated, polar strings that move with a velocity v_0 on meandering trails [Fig. 2.11(a,b)]. The heads of these strings pursue circular trajectories with stochastically varying curvatures, and the tail strictly follows the head's trajectory. Further, the strings are subjected to aggregation process which result in a continuous string thickening and merging processes between adjacent strings. The following describes the two basic ingredients of the

¹⁰Very rarely, open rings with frozen-in curvature build a closed ring by assembly of more flexible stings.

simulations: **(A)** the computation of the random trajectories and **(B)** the incorporation of the aggregation mechanisms.

(A) In the absence of aggregation processes, the trajectory of the strings is determined by stochastic forces stemming from the HMM motor proteins at the surface. Similar to worm-like bundles [47, 14], it can be expected that the curvature distribution is approximately of Gaussian shape. Mathematically, such a distribution can be generated by a stochastic process defined by the following update rule for the curvature:

$$\kappa(t_{n+1}) = \frac{1}{2} (\kappa(t_n) + \eta), \quad (2.3)$$

where n denotes the time step and η represents a random variable that is uniformly distributed over the interval $[-\alpha, \alpha]$ (α characterizes the noise level in the system). Stochastic changes of a given curvature occur with a rate ω , with equally spaced time intervals, $t_{n+1} - t_n = \omega^{-1}$. For the resulting distribution, the reader is referred to the Supplementary Material of **publication B.3**. It should be noted that Eq. (2.3) is not precisely equal to equations of motion for a discrete Brownian walker described in curvature space. The factor 1/2 introduces a memory term, which leads, however, only to weak deviation of $P(r)$ relative to a Gaussian distribution.

(B) Aggregation of the strings into longer and thicker bundles affects the trajectories of the strings in a twofold way: While elongation of strings changes their probability to collide and form even longer strings or closed loops, thicker bundles that are the result of lateral aggregation are less susceptible to curvature changes. The elongation of strings is mainly based on *merging events* between adjacent strings, which occur only for certain collision parameters. The colliding beads, say beads 1 and 2, have to be within a capture distance $R_1 + R_2$, where R_1 and R_2 denote the radii of the particular beads. The bead radius R_i mainly depends on the excluded volume of the strings and scales with the number of strings already merged according to¹¹ $R_i = R_i^0 M L_0 / L$, where R_i^0 denotes the initial radius and L the length of the structure [see Fig. 2.11(a)]. Further, strings only merge if the collision angle $|\theta|$ is smaller than a critical merging angle θ_c accounting for the binding properties of fascin, which can only link approximately parallel orientated filaments [25]. The merging naturally includes ring closure events when the head of a string interacts with its own tail. The lateral aggregation is based on the continuous uptake of individual filaments and small strings, leading predominantly to a growth in thickness. The increase in thickness results in an increased stiffness of the strings that is modeled by a linear increase of what we call a *tenacity parameter* $b(t)$

$$b(\tau_{n+1}) = b(\tau_n) + \beta b_0, \quad (2.4)$$

with b_0 being the initial tenacity $b(\tau = 0)$ and β determining the thickening speed. The time intervals are taken as equally spaced and $\tau_{n+1} - \tau_n = \lambda^{-1}$ defines the thickening rate

¹¹This formula just expresses conservation of the two-dimensional particle surface (excluded volume), since $M 2R_i^0 L_0$ is the surface of M merged strings, which shall be equal to the dynamic surface $L(t) 2R_i(t)$. Implicitly, we neglect string growth in three dimensions, which is however, only a weak effect according to experimental measurements of the light intensity (private communication with Volker Schaller).

λ . The linear tenacity increase modeled in Eq. (2.4) is motivated by the fact that a linear increase in the thickness of the strings implicitly implies an infinite filament reservoir. Since the experimentally observed ring formation is completed long before the filament reservoir is depleted, this is in good agreement with experimental observations. Thicker strings have a higher tenacity and are thus less susceptible to curvature changes. This reduced susceptibility to curvature changes can readily be modeled by modifying the update rule of Eq. (2.3) with a weight factor $w[b(t)]$ that depends on the tenacity

$$\kappa(t_{n+1}) = \frac{w[b(t_n)]\kappa(t_n) + \eta}{w[b(t_n)] + 1}. \quad (2.5)$$

The functional dependence of the weight factor w on the tenacity b is given by $w[b(t)] = \exp[(b(t) - b_0)/b_0]$. The curvature distributions that result from the incorporation of Eqs. (2.4) and (2.5) are fundamentally different from the curvature distributions that result from the stochastic process defined by Eq. (2.3). The interested reader is referred to the Supplementary Material of **publication B.3**.

Results: Competition between merging processes of actively transported strings and the growth-stiffening embodied in the increase of $b(t)$ and the weight factor w , seems sufficient to retrieve the coexistence of open and closed rings [see Fig. 2.11(b)]. Omission of one of these processes leads to the formation of either closed or open rings only. Most importantly, the cumulative radii distributions $P(r)$ for open and closed rings decay exponentially in accordance with experimental observations [see Fig. 2.11(c)], with average ring radii of open rings larger than the ones of closed rings.

Moreover, the simulations allow for a backtracking of the steady state properties to the inherent noise in the active system which determines the stochasticity of each string trajectory: Lowering the amplitude α or increasing the rate of curvature changes ω leads to an increase in the fraction of open to closed rings, denoted Γ [see Fig. 2.11(d)]. This prediction has also been verified in the experiment as the noise level in the system can be addressed by varying the motor density on the cover slip σ_m . A decreased number of motor proteins on the surface leads to more rugged trajectories and hence smaller curvature radii. In accordance with simulations, a gradual decrease of the motor density (*i.e.* a larger noise level, equal to larger α in the simulation) decreases the ratio between open and closed rings Γ (not shown, see **publication B.3**). Taken together, the consistent predictions of the model confirm that the assembly dynamics of rings in the gliding assay with crosslinkers can be understood in terms of the competition between merging events of filaments and filament growth that freezes the curvature.

In summary, the high-density motility assay serves as a versatile model system to explore the full breadth of non-equilibrium steady states in active systems. In section 2.1.2 it was shown that the interplay between assembly and disassembly of driven filaments leads to dynamic patterns like swirls, clusters, and density waves [Fig. 2.6]. These non-equilibrium steady states are characterized by the perpetual formation and destruction of structures driven by the on-going input of energy at the scale of an individual filament. Upon adding just a single new ingredient, namely passive crosslinking molecules, we have found here that the nature of the non-equilibrium steady state changes fundamentally; the presence

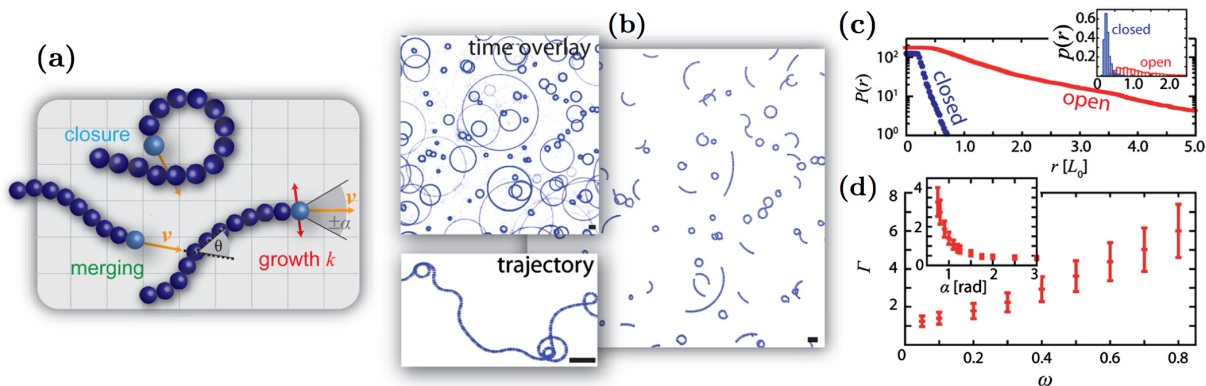


Figure 2.11: *Results of the Cellular automaton simulations:* (a) The two experimentally observed aggregation processes — merging and growth stiffening — are described using a continuous agent-based simulation. The actin-fascin strings are modeled as polar elongated strings that move with a velocity v_0 on meandering trails. The tip is subjected to curvature changes of rate ω and a noise level α , resulting in a meandering trajectory [inset (b)]. The strings stiffen due to growth processes of rate λ . Furthermore, merging events with adjacent objects occur if the relative angle θ between them is smaller than θ_c . These two aggregation processes lead to the emergence of rings in two configurations — open and closed (b). The occurrence of two ring configurations is reflected in the ring radii distribution $p(r)$ and the corresponding cumulative distribution $P(r)$ that can be separated in open and closed contributions (c). The distribution for open and closed rings decays approximately exponential. The ratio of open to closed rings Γ increases with the rate of the random turns ω , while it decreases with the noise level α , see (d). Parameters are: $\omega = 0.1$, $\lambda = 0.4$, $\alpha = 1$, $\beta = 0.2$ and $\theta_c = 10$ degrees. All scale bars are one string length L_0 . For more details on the simulation, the reader is referred to Material and Methods as well as the Supplementary Material of **publication B.3**.

of crosslinking molecules facilitates permanent filament aggregation and thereby switches off the disassembly pathway. As a consequence, the system's dynamics drive the filament assembly into an absorbing state where the structure arrests while the filaments still move. The coarsening process towards this absorbing state combines active driving with filament aggregation. Once reached, this state is stable and independent of the activity of the system, yet it directly maps the assembly pathway. This “structural memory” relies on the intricate mechanical coupling between active transport and aggregation processes. This coupling and the ensuing aggregation mechanisms fully determine the statistical properties of the absorbing state.

Two remarks are in order: The phenomena discussed in this section are strongly determined by the type of the crosslinking molecule, in this case, the passive and polar crosslinker fascin. Different crosslinking molecules give rise to a completely different structure formation: For example, one finds contracting gels (termed “active compactification”) in the presence of non-polar cross linkers α -actinin [88]. Finally, if molecular motors are no more

confined to the planar substrate, active gels with strongly localized density heterogeneities are observed [55, 54].

2.2 The Vibrated Polar Disk Assay

The setup for vibrated particle systems typically consists of the following three basic constituents: Granular particles (“grains”) manufactured from hard solids like metal, a planar substrate (“plate”) and a shaker-apparatus capable of periodically vibrating the substrate. Granular particles are typically of size $\mathcal{O}(1mm)$ and come in various shapes: Disks [30, 31], spheres (see *e.g.* Refs. in [9]) or rods [33, 18, 10, 58]. Particle movement, in general, occurs due to interactions with the vibrating substrate and the time scale of the interactions is set by the frequency of the plate vibration. During a vibration period each grain collides with the plate where it gains momentum depending on the particle’s state¹² at the moment of contact. If the interaction with the plate is anisotropic due to *e.g.* the anisotropic shape of the particles, one can observe a rather persistent motion for these asymmetric particles [33, 18, 10, 58, 30, 31]; see Fig. 2.12(c). Otherwise, if particles are perfectly isotropic with respect to plate collisions, as in the case of spheres or disks, the ensuing single particle motion is diffusive¹³ [Fig. 2.12(d)]. The driving, which is coupled to the granule’s *inherent asymmetry* at the moment of contact with the plate, makes the vibrated granular particles a **propelled particle system**.

In the following we consider a specific example of a vibrated granular system, where particles are trapped between two plates, with the lower of both vibrated vertically (parallel to the direction of gravity). Moreover, particles are perfectly round (disks) with respect to inter-particle collisions. However, regarding the collisions with the vibrating substrate underneath, these particles have a *built-in polar anisotropy* [see Figs. 2.12(a) and 2.12(b)]: The rear part is made of rubber, while the front part consists of a tiny metal tip. During vibration, this asymmetry leads to a rather persistent movement of these particles compared to disks, which lack any built-in asymmetry [see Figs. 2.12(c) and 2.12(d)]. In the horizontal direction, the system is confined by a flower-shaped solid boundary [see Fig. 2.12(e)], where the specific shape of the boundary was chosen in order to reduce particles’ jamming in sharp edges of *e.g.* a rectangular geometry. Interestingly, large collections of polar vibrated disks exhibit swirling and swarming patterns (see Fig. 2.12(e), left; and [30, 31]) quite similar to the gliding assay at high filament densities (refer to section 2.1.2). In order to understand how these patterns develop at the particle level, we aim at a *quantitative* modeling approach for the vibrated polar disk assay. Initially, the basic qualitative experimental observations are presented in section 2.2.1. In section 2.2.2 a theoretical model is discussed that *quantitatively* matches with the corresponding experimental observations (the qualitative agreement is already indicated in Fig. 2.12(e), right). The *quantitative* agreement of the model dynamics to those from experiment allows us to use the model to investigate system sizes inaccessible for the experiment due to the inherent limitations¹⁴ of the vibration apparatus. Therefore, the model offers the answer to the following question: *Can the experimental system exhibit a phase transition to a true long-range ordered, coherently moving state in the absence of confining boundaries?*

¹²The state of a granular particle is given by its orientation and the center-of-mass coordinates.

¹³Diffusive trajectories are observed for time scales notably above the inverse vibration frequency.

¹⁴Increasing the size of the vibrating plate leads to bending modes interfering with the particle dynamics.

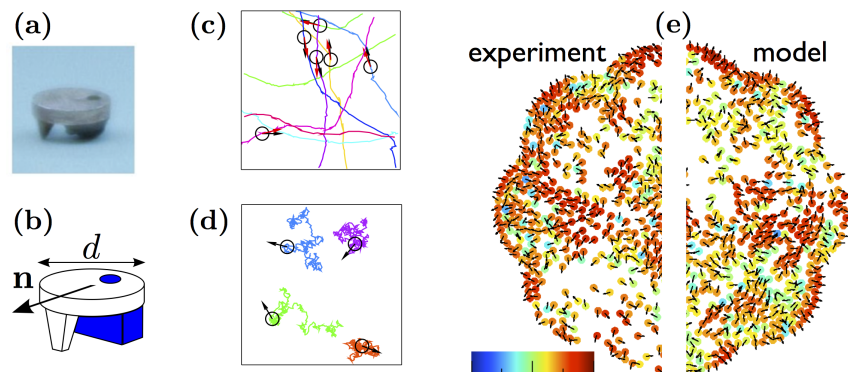


Figure 2.12: (a) Photograph and (b) sketch of one polar disk, with particle's polarity \mathbf{n} indicated. (c) Polar disks typically move along persistent trajectories, while (d) isotropic disks without built-in asymmetry mostly perform a random walk. (e) Typical snapshots of the patterns observed in the petal-shaped geometry, for the experiment (left), and the model (right). Particles that are aligned parallel [anti-parallel] to their neighborhood are depicted in red [blue] (figures (c), (d) with courtesy of Oliver Dauchot).

2.2.1 Qualitative Experimental Observations

Let us first summarize the main *qualitative* experimental findings and observations from the vibrated polar disk assay [30, 31], and give their implications for the equations of motion of a model that adequately describes the dynamics:

- There are two, in generally non-parallel fields in the dynamics of the polar disks: Particle velocity and intrinsic polarity [Fig. 2.12(b)]. This fact is illustrated in Fig. 2.13, which depicts a typical collision. Blue arrows correspond to the polarity and the solid line indicates the trajectory. An appropriate model should therefore involve equations of motion for both respective fields, and it is required to capture adequately the coupling between both.
- Even though the particle polarity is rather persistent, the velocity fluctuates comparably strongly. These pronounced velocity fluctuations even lead to notable periods of backward motion. A model should be able to account for this finding and reproduce the ratio between backward and forward displacements.
- Particles are made of hard materials and move in the absence of a surrounding dissipating medium. Therefore, particle interactions in the model's equations of motion should be solely short-range and repulsive.

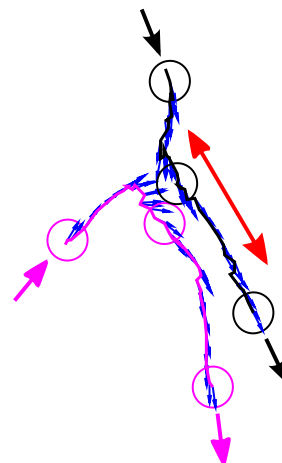


Figure 2.13: Illustration of a typical collision.

- Collisions are observed to exhibit a rather peculiar feature [see Fig. 2.13]: One “encounter” typically involves many successive collisions, where each time the particles bounce back without altering their polarity much, so that they quickly collide again. These encounters last for a finite time and take place over some finite spatial extension. An appropriate model should be able to reproduce these characteristics as well as the average extension and duration of these strange encounters.
- Particles are observed to move with significantly lowered speed close to the horizontally confining boundary. This and the aforementioned “bouncing-back” collisions imply that the model must account for particles’ inertia.
- The shape of the boundary was found to have a profound effect on the system’s patterning properties due to accumulation of particles at the boundary. Therefore, the shape of the boundary (*i.e.* the flower-shaped geometry) must be explicitly accounted for.

In the following section we aim at a model, *i.e.* a set of equations of motion, that give rise to the qualitative features listed above, and also allows us to reproduce the single and collective dynamics *quantitatively*.

2.2.2 Quantitative Modeling of the Dynamics of Vibrated Polar Disks

In the experimental setup, the polar disks are vibrated between two plates. Rather than modeling their full three-dimensional dynamics, we describe their effective two-dimensional motion. In other words, vertical vibrations are not treated explicitly. Instead, the vibration amplitude enters implicitly via effective parameters. The major new features of the model compared to Vicsek-like models [105, 28, 22, 40, 23] are: (i) The dynamics of the particle’s intrinsic polarity with respect to their velocity is explicitly described, and (ii) no explicit alignment rules are employed, but collisions are modeled explicitly. We assume that the vibration frequency is large enough to allow us to describe driving and dissipation of the particles via continuous forces. Building on the experimental observations detailed in section 2.2.1, we were led to the following model¹⁵: Particle i is subject to a noisy acceleration along its *polarity* axis \mathbf{n}^i (with anisotropic, intrinsic, “active” noise, with respect to the particle’s polar symmetry), balanced by an effective linear friction term along its *velocity* $\mathbf{v}^i = \frac{d}{dt}\mathbf{r}^i$, with \mathbf{r}^i denoting the particle’s coordinates. Particles i and j with $|\mathbf{r}^i - \mathbf{r}^j| < d$, where d is the particle diameter, interact by means of a pairwise, inelastic, repulsive interaction force \mathbf{F}_ϵ^{ij} . Hence, we have

$$\frac{d}{dt}\mathbf{v}^i = [\mu + \eta_{\parallel}]\mathbf{n}^i + \eta_{\perp}\mathbf{n}_{\perp}^i - \beta\mathbf{v}^i + \sum_j \mathbf{F}_\epsilon^{ij}, \quad (2.6)$$

¹⁵Other solutions were tested, but the one presented here is both simple and quantitatively consistent with the data.

where μ and β are constants giving rise to a stationary speed $v = \mu/\beta$, \mathbf{n}_\perp^i is a unit vector perpendicular to \mathbf{n}^i , $\eta_{\parallel,\perp}$ represent Gaussian distributed white noises with zero mean, *i.e.* $\langle \eta_{\parallel,\perp}(t)\eta_{\parallel,\perp}(t') \rangle = 2D_{\parallel,\perp}\delta(t-t')$, where $D_{\parallel,\perp}$ denotes the corresponding diffusion constant. The interaction force \mathbf{F}_ϵ^{ij} is given by the established spring dash-pot model [52, 20], which, for hard particles, depends on just a single parameter, the restitution coefficient ϵ . Specifically, $\mathbf{F}_\epsilon^{ij} = [-\lambda(\mathbf{v}^i - \mathbf{v}^j) \cdot \hat{\mathbf{r}}_{ij} + \kappa(d - |\mathbf{r}^i - \mathbf{r}^j|)]\hat{\mathbf{r}}_{ij}$, for $|\mathbf{r}^i - \mathbf{r}^j| < d$, and $\mathbf{F}_\epsilon^{ij} = 0$ otherwise, where $\hat{\mathbf{r}}_{ij} = \frac{\mathbf{r}^i - \mathbf{r}^j}{|\mathbf{r}^i - \mathbf{r}^j|}$, and parameters λ and κ are related to the (normal) restitution coefficient via $\epsilon = \exp(-\lambda\tau_{\text{hc}})$ with $\tau_{\text{hc}} = \pi[2\kappa - \lambda^2]^{-1/2}$ [52].

Eq. (2.6) must be complemented by one governing the polarity of particles, which was observed to remain anti-aligned to the velocity during episodes of backward motion. In other words, when $\alpha^i = \angle(\mathbf{v}^i, \mathbf{n}^i)$, the angle between velocity and polarity, is acute, frictional interactions with the vibrating plate are assumed to rotate \mathbf{n}^i towards \mathbf{v}^i , while for $|\alpha^i| > \pi/2$, \mathbf{n}^i rotates towards $-\mathbf{v}^i$ [see Fig. 2.15 for an illustration of the directions of rotation]. We thus propose the following equation for the polarity angle θ^i [with $\mathbf{n}^i = (\cos \theta^i, \sin \theta^i)$]:

$$\frac{d}{dt}\theta^i = \zeta \sin \alpha^i \text{sign}(\cos \alpha^i), \quad (2.7)$$

where ζ characterizes the strength of the coupling between polarity and velocity. This parameter is expected to be rather small given the observed persistence of \mathbf{n} even when \mathbf{v} changes sign abruptly.

Before proceeding to the results, let us consider how Eq. (2.6) and Eq. (2.7) can lead to parallel alignment of particles. In general, there are two distinct particle configurations [Fig. 2.15]: **(a)** In one case, director and velocity point into the same half-plane (defined by the director, with $\cos \alpha > 0$), which applies to *e.g.* cases of persistent movement. In the other case, **(b)** director and velocity point into opposite half-planes ($\cos \alpha < 0$), *e.g.* after bouncing back collisions or collisions with the boundary. It is the hard inter-particle collision that spontaneously creates an angle α between both fields, which is either reduced to zero **(a)** or increased towards π **(b)**. Then, depending on the relative orientation and spatial arrangement of the two colliding particles, each rotation of the particle itself (between two successive collisions) changes the relative orientation towards a parallel or an anti-parallel configuration. This is reflected in the typical outcomes of collisions, which are either aligned approximately parallel [Fig. 2.13] or “indifferent”, *i.e.* their pre-collisional angle is approximately equal to the post-collisional angle [see Fig. 2.14].

Rescaling: To make contact with the experimental results, we rescale time $t \rightarrow t/\tau_0$, with τ_0 the inverse of the vibration frequency $f = 115$ Hz [30, 31]. Length is measured in particle diameters d : $\mathbf{x} \rightarrow \mathbf{x}/d$. Our model possesses six parameters: μ , β , ζ , D_\parallel , D_\perp , and ϵ . At fixed (dimensionless) experimental vibration amplitude¹⁶ $\Gamma = 2\pi a f^2/g$, one



Figure 2.14: Illustration of an “indifferent” collision.

¹⁶Vibration amplitude a is about $25\mu\text{m}$ and is measured at a peak acceleration of $1g$ at the given frequency f .

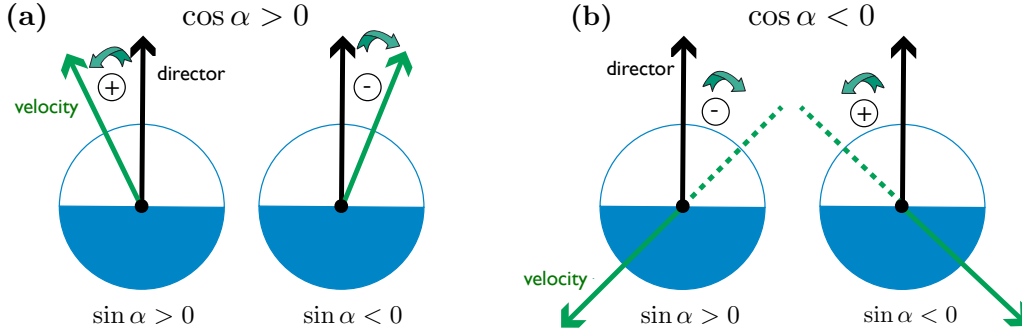


Figure 2.15: Coupling between velocity and director in Eq. (2.7): **(a)** If the velocity and the director point into the same half-plane, the director is directed towards the velocity, while **(b)** for the opposite case, the director is rotated towards the negative velocity.

parameter can be eliminated by matching the typical experimental speed with the model’s velocity $v = \mu/\beta$. In the following, we use the experimental data gathered at the vibration amplitude $\Gamma = 2.7$, where the most ordered regimes have been observed, and for which $v = 0.025$ [30, 31].

Single particle results: We first analyze the single-particle dynamics in order to test the overall quality of the model and to estimate the remaining four parameters (*i.e.* β , ζ , D_{\parallel} , D_{\perp} ; the restitution coefficient ϵ only affects particle interactions). To find the best-matching set of parameters, we consider the following two quantities: The angular diffusion constant $D_{\theta} = \frac{1}{2\tau} \langle [\theta(t + \tau) - \theta(t)]^2 \rangle_t$ (with $\langle \dots \rangle_t$ denoting a time-average), and the ratio of the displacement fluctuations parallel and perpendicular to the polarity, $\Pi := \frac{\langle \Delta r_{\parallel}^2 \rangle_t - \langle \Delta r_{\parallel} \rangle_t^2}{\langle \Delta r_{\perp}^2 \rangle_t - \langle \Delta r_{\perp} \rangle_t^2}$, with $\Delta r_{\parallel, \perp}(\tau, t) = \sum_{m=t/\Delta t}^{(t+\tau)/\Delta t} [\mathbf{r}^i(m\Delta t + \Delta t) - \mathbf{r}^i(m\Delta t)] \cdot \mathbf{n}_{\parallel, \perp}^i(m\Delta t)$, where $\Delta t = 5.75 \tau_0$, equal to the experimental sampling time determined by the camera frame rate. Scanning the four dimensional parameter space, we select a best-matching parameter set for which both quantities agree with the experimental value within an error margin of $\pm 30\%$. This is approximately equal to the imprecision arising due to different preparations of the experimental setup. In spite of this modest accuracy, the model quantitatively captures the observed experimental particle dynamics: We compare the distributions of the parallel displacements normalized by τ , denoted as $v_{\parallel}(\tau) = \Delta r_{\parallel}/\tau$, and of the angle $\alpha(\tau) = \angle(\mathbf{n}(t), \mathbf{r}(t + \tau) - \mathbf{r}(t))$ to those recorded experimentally. We find a very good agreement for all values of τ considered [Figs. 2.17(a) and 2.17(b)]. Note that, as expected, the particles exhibit backward motion for significant time periods [tails in the negative sector in Fig. 2.17(a), and peaks at $\pm\pi$ in Fig. 2.17(b)].

Binary collision results: We now turn to binary collisions, for which the restitution coefficient ϵ must be chosen. The following results are presented for $\epsilon = 0.4$, but we observed that changing ϵ in the range $\pm 30\%$ does not influence collision properties significantly. Experiments have revealed that one “encounter” typically involves many successive collisions, where each time the particles bounce back without changing their polarity much, so that they quickly collide again. These encounters last for a finite time and take place

over some finite spatial extension. It was found experimentally that they are well delimited using the following criterion: An encounter starts when two particles get closer than some threshold collision distance¹⁷, namely $|\mathbf{r}^i - \mathbf{r}^j| \leq d_c = 1.7$, and their polarities point “inwards”, *i.e.* $|(\mathbf{r}^i + \mathbf{n}^i) - (\mathbf{r}^j + \mathbf{n}^j)| \leq |\mathbf{r}^i - \mathbf{r}^j|$ (see Fig. 2.16 for an illustration; and [31]). An encounter ends when either particles are separated by more than d_c , or their polarities point “outwards”. We have used the same criterion for our model. Figures 2.17(c-f) depicts the results of a scattering study for the experimental setup and the model.

Thousands of binary encounters (hereafter called collisions for simplicity) were recorded, and the outgoing relative angle θ_{out} of the two particles plotted against their incoming relative angle θ_{in} , the impact parameter $b \in [0, 1]$ [20] is shown as color code [Figs. 2.17(c) and 2.17(d)]. The model data shows a striking agreement with the results measured in the experiments: Most collisions actually leave the polarities unchanged ($\theta_{\text{out}} \simeq -\theta_{\text{in}}$), and a minority of them align the particles almost perfectly ($\theta_{\text{out}} \simeq 0$). We estimated the fraction of polar aligned events, finding 0.14 for the model and 0.18 for the experiment¹⁸. The model also matches the distribution of head-on ($b \approx 0$) and glancing ($b \approx 1$) collision events. We further determined the PDF of the duration of collisions τ_{col} as well as that of their spatial extension ℓ_{col} , given by the center of mass displacement. The model reproduces the observed exponential distribution of τ_{col} quantitatively, while it fails to reproduce the roughly algebraic decay of ℓ_{col} (but nevertheless gives a correct mean extension). To what degree this is an actual discrepancy between model and experiment remains to be clarified. In fact, the very existence of an algebraic decay for the experimental data can be questioned due to the small number of collisions with large extensions.

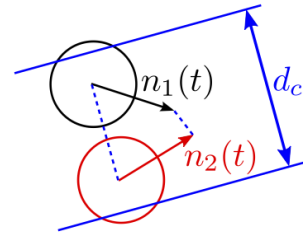


Figure 2.16: Definition of an encounter.

Thousands of binary encounters (hereafter called collisions for simplicity) were recorded, and the outgoing relative angle θ_{out} of the two particles plotted against their incoming relative angle θ_{in} , the impact parameter $b \in [0, 1]$ [20] is shown as color code [Figs. 2.17(c) and 2.17(d)]. The model data shows a striking agreement with the results measured in the experiments: Most collisions actually leave the polarities unchanged ($\theta_{\text{out}} \simeq -\theta_{\text{in}}$), and a minority of them align the particles almost perfectly ($\theta_{\text{out}} \simeq 0$). We estimated the fraction of polar aligned events, finding 0.14 for the model and 0.18 for the experiment¹⁸. The model also matches the distribution of head-on ($b \approx 0$) and glancing ($b \approx 1$) collision events. We further determined the PDF of the duration of collisions τ_{col} as well as that of their spatial extension ℓ_{col} , given by the center of mass displacement. The model reproduces the observed exponential distribution of τ_{col} quantitatively, while it fails to reproduce the roughly algebraic decay of ℓ_{col} (but nevertheless gives a correct mean extension). To what degree this is an actual discrepancy between model and experiment remains to be clarified. In fact, the very existence of an algebraic decay for the experimental data can be questioned due to the small number of collisions with large extensions.

Collective results: We performed simulations using the same flower-shaped geometry [Fig. 2.12(e)], and number of particles ($N = 890$) as in the experiment [30, 31]. For the parameter values matching the single particle dynamics and binary collisions (for vibration amplitude $\Gamma = 2.7$), we observe, as in the experiments, fairly large, polar aligned, moving clusters [compare Fig. 2.12(e) right/left]. However, the order parameter $\psi(t) = \frac{1}{M(t)} |\sum_{i \in \text{ROI}} \mathbf{n}^i|$, with $M(t)$ denoting the number of particles currently located within the central “region of interest” (ROI) of radius 10, is typically smaller than in the experiment [Fig. 2.17(g)]. The effective packing fraction observed in the ROI is found to be very close to that of the experiment ($\phi \simeq 0.39$, whereas the nominal packing fraction is

¹⁷The value of $d_c = 1.7$ has been found empirically as optimal by means of the numerical model and the experiments: Values significantly below this value “artificially” cut collisions with larger bouncing back distances into two collisions, thereby altering the statistical quantities such as mean duration and mean length of a collision. By means of the simulations we could show that values above $d_c = 1.7$ notably increase the number of “ghost” collisions, where particles move within the collision area defined by d_c [Fig. 2.16], but leave it without touching each other due to their intrinsic stochastic single particle motion.

¹⁸To avoid counting events whose outcomes are possibly influenced by the limited camera frame rate, we neglected all events with $\theta_{\text{in}} < \pi/6$. Moreover, polar events are defined by: $\theta_{\text{out}} > -\theta_{\text{in}}/2$.

0.47), indicating that particles accumulate at the boundary in the model as well. Running the model at $\phi = 0.39$ in a box of approximately the same size but with periodic boundary conditions—a privilege of the *in silico* approach—yields only a marginally larger average polarization [Fig. 2.17(g)]: a frustration-free geometry is unable to restore enough order.

We also ran the model in square periodic domains of linear size L at the nominal packing fraction $\phi = 0.47$, and then found order being slightly stronger than in the experiment [Fig. 2.17(g)]. Nevertheless, increasing system size L , we observe that the overall order parameter $\langle \Psi \rangle_t = \langle \frac{1}{N} |\sum_{i=1}^N \mathbf{n}^i| \rangle_t$ decreases first rather slowly, then faster as a function of L [inset of Fig. 2.17(h)]. Thus, no true long-range order is present at the exact conditions probed experimentally.

Next we use a further privilege of *in silico* investigations—the freedom to change parameter values—and show that asymptotically ordered regimes would probably be observed in slightly different experimental conditions. Experimentally, the vibration amplitude Γ was used as a control parameter for the onset of collective motion. Decreasing Γ to around 2.7 in the experiments, order was observed to increase from near-zero to about $\langle \psi \rangle_t = 0.5$. Unfortunately, due to static friction, the particles stopped moving for Γ values below 2.7. To mimic different Γ -values in the model we multiply both diffusion constants D_{\parallel} and D_{\perp} by a coefficient γ^2 , with $\gamma \in [0, 2]$, so that $\gamma = 1$ corresponds with the experiment at $\Gamma = 2.7$. Varying γ , we find the transition to collective motion to be close to $\gamma = 1$ [Fig. 2.17(h)]. The transition point is observed to move slightly to smaller noise values γ as the system size is increased. This confirms that vibrated polar disks, in the experimental conditions, are asymptotically disordered, but signals that asymptotically ordered regimes do exist nearby, constituting the first report of *long-range orientational order* in colliding hard disks without explicit alignment.

Finally, we have performed a systematic exploration of the model, varying γ and the packing fraction ϕ in square domains of linear size $L = 200$ with periodic boundary conditions [not shown¹⁹]. For $\phi \lesssim 0.6$, varying γ , we observe the usual phenomenology of models with (effective) polar alignment like the Vicsek model [105, 40, 22, 23, 107]: Immediately below the transition, the particles spontaneously segregate into high-density high-order “bands”²⁰ traveling in a low-density disordered sea. Further away from the transition, these nonlinear structures disappear, leaving a homogeneous polar phase with its characteristic giant number fluctuations and long-range correlations [96, 97, 101, 95].

To summarize, we have built a simple yet quantitatively consistent model for the dynamics of the vibrated polar disks studied in [30, 31]. This model constitutes one of the first in which the dynamics of the particle’s intrinsic polarity with respect to their velocity are taken into account [46, 94]. An adequate description of the granular system of vibrated discs requires that the polarity is treated as a slow variable compared to the velocity, which can change fast due to collisions with the plate or neighboring particles. Our *in silico* study has shown that in the original experiments, the most ordered state reached was in fact in

¹⁹The interested reader is referred to **publication B.6**.

²⁰Interestingly, for $\phi \geq 0.6$, we could not observe bands in the large noise regime. A detailed discussion and its implication on the nature of the phase transition is described in **publication B.6**.

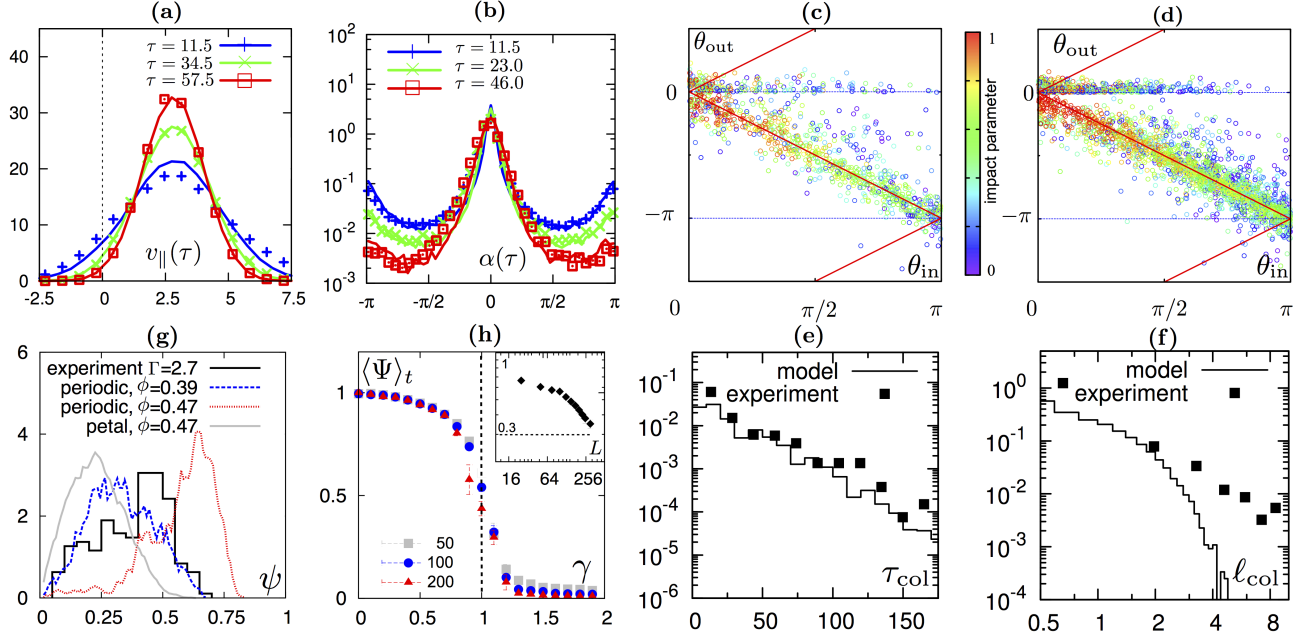


Figure 2.17: **(a)** PDF of v_{\parallel} and **(b)** PDF of the angle $\alpha = \angle(\mathbf{n}(t), \Delta\mathbf{r}(t + \tau))$ [lin-log] for selected values of the time increment τ . Experimental data are indicated with symbols; model data are illustrated with lines. **(c,d)** Scatter graph $\theta_{\text{in}} - \theta_{\text{out}}$ for the experiment **(c)**, and our model **(d)**. Values of the impact parameter b are indicated by the color bar. PDF of the duration τ_{col} **(e)** [lin-log], and the extension ℓ_{col} of a collision **(f)** [log-log]. **(g)** PDF of the average polarization ψ , evaluated within the ROI, for the experimental system, the model in the petal-shaped geometry and in periodic boundaries using two values of packing fractions: $\phi = \{0.39, 0.47\}$. **(h)** Average polarization $\langle \Psi \rangle_t$ as a function of the noise fraction $\gamma^2 = D_{\parallel}/D_{\parallel}^{\Gamma=2.7} = D_{\perp}/D_{\perp}^{\Gamma=2.7}$, shown for three boundary sizes $L \in \{50, 100, 200\}$ and $\phi = 0.47$. *Inset:* $\langle \Psi \rangle_t$ [log-log] for $\gamma = 1$ and $\phi = 0.47$ as function of system size L .

the region of the transition to collective motion, slightly on the disordered side. However, asymptotically-ordered regimes do exist nearby. In conclusion, concerning the initial question of whether polar vibrated disks exhibit a phase transition to a true long-range ordered, coherently moving state in the absence of confining boundaries, the answer is: “Yes”.

2.3 Modeling Propelled Particle Systems under Dilute Conditions

This section deals with modeling approaches suited to describe the dynamics of propelled particle systems under *dilute* conditions. In contrast to the two previous sections, most of the models described in this section do not *explicitly* refer to a specific experimental setup. However, these models can be regarded as extensions of common, already established models in order to appropriately account for recent qualitative experimental observations in propelled particle systems. We will discuss these qualitative observations in the respective sections in more detail.

In section 2.3.1, a lattice gas automaton for propelled particles with local “ferromagnetic” interactions is introduced. By means of this model, we will show that the phase transition to collective motion is induced by stochastically nucleated, coherently moving clusters. All following sections are devoted to different kinetic approaches. For the reader’s convenience, a digression, establishing the basic knowledge about kinetic theory for propelled particle systems is presented in section 2.3.2. A list of open questions in kinetic theory is given in section 2.3.3, bridging the gap between the state of the art and the research work performed in this thesis. Each of the subsequent section is then dedicated to one of these open questions. Section 2.3.4 deals with the extension of the Boltzmann equation to rod-like particles, and how ordering capabilities are changed due to the rod’s shape. After that, in section 2.3.5, we investigate the role of particle conservation in collections of propelled particles, and investigate how pattern forming capabilities are influenced if particle number is not conserved. The impact of a limited interaction range as well as deviations from a popular generic interaction rule (called *half-angle alignment* rule) are detailed in section 2.3.6. Finally, we show how kinetic theory must be modified in order to obtain a quantitatively correct prediction for the phase boundary between the isotropic and polarized state in the dilute limit; *cf.* section 2.3.7.

2.3.1 Rule-based Automaton with Local Interactions

While previous approaches on propelled particle systems focussed on the long-time dynamics [105, 28, 29, 22, 40, 23, 11], *e.g.* the emergence of the polar state, or concentrated on the analysis of the ensuing stationary patterns, the transient assembly processes leading to collective motion remain largely elusive. In the introduction (section 1.2) we explained that growing clusters act as “vacuum cleaners”, which successively take up surrounding particles and align them to the horde. Since clusters already exist on the isotropic side of the phase boundary it is not clear which criteria clusters must meet to induce a transition (in time) to a polar state.

To investigate this question, we designed a rule-based automaton for (self-)propelled particles moving on a hexagonal lattice which is efficient enough to deal with large system sizes and particle numbers, thereby offering good statistics to study the time-dependent dynamics on short and long time scales. In our model, particles of length L and width equal

to one inter-lattice spacing, interact via an effective excluded volume interaction and a local polar alignment field. Both enter into the model by supplementing the probabilities for the unperturbed persistent random walk by appropriate factors [for details on the model please refer to caption of Fig. 2.18(a)]. Since particles in the model move with constant speed and interactions solely change the outcome with respect to the particles' orientations, the automaton model is restricted to *dilute* conditions where caging effects or the emergence of bond orientational and translational order can be neglected.

In the absence of excluded volume interactions, we find—in agreement with other agent-based models with ferromagnetic interactions, *e.g.* [105, 28, 22, 29, 40, 23]—a phase transition to collective motion above a critical packing fraction. Interestingly, strong excluded volume interactions increase this critical packing fraction or even inhibit the development of collective motion. This breakdown of collective motion at large particle densities has also been found in other models [67], **publication B.9** and **publication B.8**. A heuristic explanation for this finding is the following: While ferromagnetic interactions tend to build-up parallel orientations, repulsive interactions lead to anti-correlations in the velocity. Therefore, it is only a matter of the strength of the ferromagnetic to the repulsive interaction whether collective motion emerges or not²¹.

Analyzing the dynamics of the pattern forming processes of N particles, we find that collective motion is accompanied by a gain in free volume, $\rho - \gamma$, where $\rho = NL/A$ [with A : area of simulation domain, and $N \sim 10^6$] is the (reduced) particle density and γ denotes the fraction of occupied lattice sites. In the absence of polar alignment processes between the filaments or for too strong excluded volume interactions, we find that γ fluctuates around a constant value depending on the strength of the excluded volume interaction ϵ [see Fig. 2.18(b), inset]. Adding polar alignment interactions leads to qualitatively different behavior: There is a threshold density ρ_c , where the gain in free volume $\rho - \gamma$ jumps to a value much larger than the corresponding value for a non-interacting system. Moreover, measuring the polar order parameters, it turns out that this jump actually coincides with the onset of polar order. The jump in $\rho - \gamma$ may, therefore, be taken as a signature to map out the model's phase diagram (not shown, see **publication B.4**). The gain in free volume also clearly indicates that filaments must have formed some clusters much denser than expected for a purely statistical (random) overlap of filaments. Fig. 2.18(b) shows that these clusters are formed by a nucleation process: There is a *lag-phase* during which γ remains largely close to a value obtained in the absence of polar alignment processes. Subsequently, there is a time window $[T_{\text{nuc}}, T_{\text{stat}}]$, where the available free volume fraction $\rho - \gamma$ increases towards a higher stationary value. The time to reach the final polar steady state diverges as a power law $T_{\text{stat}} \propto (\rho - \rho_c)^{-\zeta}$ with $\zeta \approx 1$.

Due to the fact that small clusters are continuously assembled and disassembled during the *lag-phase*, the sudden decrease of γ at T_{nuc} indicates that a notably larger cluster develops. Until such an event occurs, the overall macroscopic state, characterized here by

²¹This argument only applies to models with equations of motion solely for particles' velocities. Particles with *e.g.* a direction and a velocity can sustain strong repulsive interactions, while keeping orientational correlations. An example is the vibrated polar disk assay, which is discussed in section 2.2.

the gain in free volume, is unchanged. A systematic analysis of the cluster mass distribution during the *lag-phase* corroborates our finding that the onset of collective motion is triggered by a single nucleation events (details on evaluation of cluster mass distribution see **publication B.4**), which manifests itself in a coherently moving cluster of sufficiently large size/mass. We conclude that collective motion close to the critical density is induced by a rare event, *i.e.* the nucleation of a cluster of sufficiently large mass, and not by a wide-spread coarsening process of polarized domains.

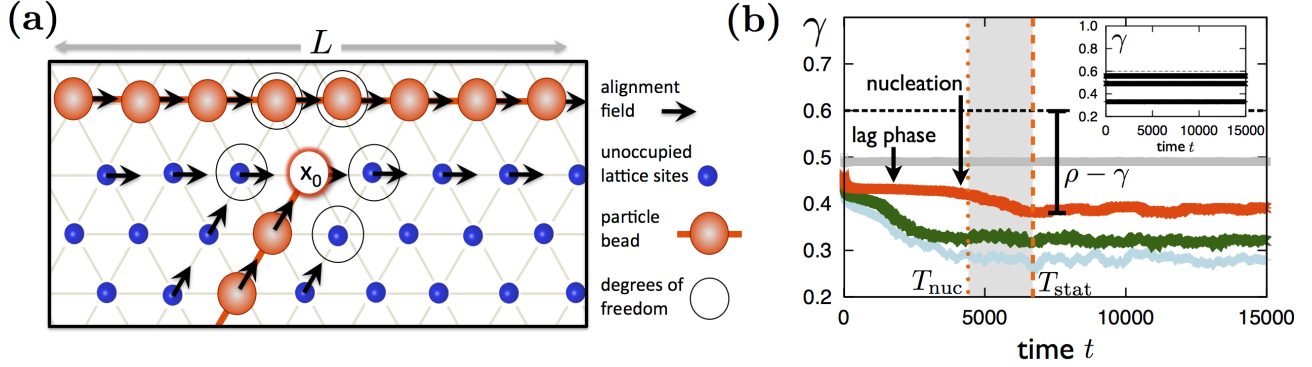


Figure 2.18: **(a) Illustration of the rule-based lattice gas automaton:** The particles' dynamics are assumed to be fully determined by its head, while the tail strictly follows the head's trail. The persistent random walk is implemented by a stochastic process, where each filament's head \mathbf{x}_0 moves to one of its five neighboring sites \mathbf{x}_α according to a fixed set of conditional probabilities $P_{\text{prw}}(\mathbf{x}_\alpha|\mathbf{x}_0)$. *Excluded volume:* For a lattice site that is already k -times occupied, the probability for further occupation is reduced by a Boltzmann factor, $e^{-k\epsilon}$, where ϵ characterizes the penalty for multiple occupations. Formally, for $\epsilon \rightarrow \infty$, the limit of strict excluded volume is obtained. *Alignment interaction:* Each particle is assigned an alignment field $\mathbf{u}(x, t)$ at its occupied and neighboring lattice sites (see black arrows); it is directed along the particles contour. Overlapping alignment fields of different particles are averaged. In a collision event, the alignment field modifies the transition probability to move from \mathbf{x}_0 to \mathbf{x} by the Boltzmann factor, $\alpha^{\cos\varphi}$, where φ is the relative angle between the alignment field and the direction of motion of the respective collision partner, $\varphi = \angle(\mathbf{u}(\mathbf{x}), \mathbf{x} - \mathbf{x}_0)$. *Update rule:* Given a configuration of N filaments we use random sequential updating and move a chosen head from position \mathbf{x}_0 to a target position \mathbf{x} with probability $P(\mathbf{x}|\mathbf{x}_0; \mathbf{u}, k) \propto P_{\text{prw}}(\mathbf{x}|\mathbf{x}_0) \cdot e^{-k\epsilon} \cdot \alpha^{\cos\varphi(\mathbf{u})}$. **(b) Lag-phase and nucleation:** Time traces of the ratio of occupied lattice sites γ for $\rho = 0.6$, and a set of values: $\epsilon = 0, 0.5, 1$ with $\alpha = 5$, and $\epsilon = 1$ with $\alpha = 1$, from bottom to top. Close to the phase boundary from the isotropic (ISO) to the polar ordered state (PO) [$\epsilon = 1$; (red)], a *lag-phase* exists, where the system waits for the nucleation of a cluster that triggers the emergence of polar order; the time when nucleation occurs T_{nuc} and the time when γ becomes stationary T_{stat} are indicated by vertical dotted or dashed lines. *Inset:* for $\alpha = 1$, no order develops, irrespective of the value of ϵ ($\epsilon = 0, 5, 100$ from bottom to top).

2.3.2 Digression: Kinetic Theory for Propelled Particle Systems — Basic Assumptions & Findings

This section serves as a summary of the basics ingredients and predictions of kinetic theory for propelled particle systems. A reader familiar with kinetic theory can proceed to the next section on the open questions in kinetic theory for propelled particle systems.

Boltzmann Equation for Propelled Particle Systems

As in the case of monatomic gases, the Boltzmann equation for propelled particles moving at constant speed in two dimensions [15, 16] provides a link between the system’s macroscopic behavior and the underlying “microscopic” physics of collisions. The latter is, *e.g.* described by Newtonian equations of motion or automaton rules, as detailed in the previous section. The Boltzmann equation for propelled particles in two dimensions governs the time-evolution of the one-particle density $f(\mathbf{r}, \theta, t)$, which is a function of the spatial coordinates \mathbf{r} , the orientation of the velocity θ and time t . Considering solely the *one*-particle density leads to²² the restriction to binary interactions between the constituent particles, in turn limiting the validity of the Boltzmann equation to dilute conditions. Binary interactions are described by collision integrals with each kernel involving a measure for the rate of collisions, known as the *Boltzmann collision cylinder*, as well as a *collision rule*. The latter constitutes a mapping between the pre-collision angles θ_1 and θ_2 and the post-collision orientations of the two colliding particles. The corresponding continuous distribution function required to compute the rate of binary collisions is actually the two-particle density $f^{(2)}(\mathbf{r}, \theta_1, \theta_2, t)$. However, to obtain a closed equation for the time evolution of the one-particle density $f(\mathbf{r}, \theta, t)$, called the *Boltzmann equation*, the *assumption of molecular chaos* is commonly applied [15, 16],²³

$$f^{(2)}(\mathbf{r}, \theta_1, \theta_2, t) = f(\mathbf{r}, \theta_1, t)f(\mathbf{r}, \theta_2, t), \quad (2.8a)$$

which neglects any correlations between the particles. Following Refs. [15, 16], the time evolution of the one-particle density $f(\mathbf{r}, \theta, t)$ is given by:

$$\partial_t f(\mathbf{r}, \theta, t) + \underbrace{v_0 \hat{\mathbf{v}}(\theta) \cdot \nabla f(\mathbf{r}, \theta, t)}_{\text{streaming}} = \underbrace{\mathcal{N}[f](\mathbf{r}, \theta, t)}_{\text{angular fluctuations}} + \underbrace{\mathcal{C}[f^{(2)}](\mathbf{r}, \theta, t)}_{\text{interaction kernel}}. \quad (2.8b)$$

The second term on the l.h.s. is the streaming term accounting for movement of particles with a velocity $v_0 \hat{\mathbf{v}}(\theta)$, where $\hat{\mathbf{v}}(\theta) = (\cos \theta, \sin \theta)$ is the orientation and v_0 denotes the constant speed. The first term on the r.h.s. in Eq. (2.8b) describes the influence of random angular single particle fluctuations (or self-diffusion events) occurring at a rate λ and reads [15, 16]:

$$\mathcal{N}[f](\mathbf{r}, \theta, t) = -\lambda f(\mathbf{r}, \theta, t) + \lambda \int_{-\pi}^{\pi} d\theta' f(\mathbf{r}, \theta', t) \int_{-\infty}^{\infty} d\eta p_0(\eta) \bar{\delta}(\theta' + \eta - \theta), \quad (2.8c)$$

²²This is apparent when considering the Boltzmann equation as the first equation of the Bogoliubov-Born-Green-Kirkwood-Yvon hierarchy [53].

²³Note that on the level of the Boltzmann equation collisions are assumed to occur locally at \mathbf{r} .

where angular fluctuations are assumed to be Gaussian-distributed according to $p_0(\eta)$ with a standard deviation σ_0 . The periodicity of angles is accounted for by a sum of δ -functions: $\bar{\delta}(\theta) = \sum_{m=-\infty}^{\infty} \delta(\theta + 2\pi m)$. The parameters λ and σ_0 determine the strength of background noise in the system. The single particle noise described above can either originate from fluctuations of the particles' propelling mechanism or stem from thermal fluctuations (solely rotational diffusion).

The second term on the r.h.s. in Eq. (2.8b) is the collision integral $\mathcal{C}[f^{(2)}] = \mathcal{C}^-[f^{(2)}] + \mathcal{C}^+[f^{(2)}]$. It captures the effects of binary collisions and can be split into a *loss* and a *gain* contribution, $\mathcal{C}^+[f^{(2)}]$ and $\mathcal{C}^-[f^{(2)}]$. These contributions capture the scattering of particles out of ($-$), or into ($+$) an angle interval $[\theta, \theta + d\theta]$, respectively, and read:

$$\mathcal{C}^-[f] = - \int_{-\pi}^{\pi} d\theta' \Gamma(\theta', \theta) f^{(2)}(\mathbf{r}, \theta, \theta', t), \quad (2.8d)$$

$$\mathcal{C}^+[f] = \int_{-\pi}^{\pi} d\theta_1 \int_{-\pi}^{\pi} d\theta_2 \Gamma(\theta_1, \theta_2) f^{(2)}(\mathbf{r}, \theta_1, \theta_2, t) \int_{-\infty}^{\infty} d\eta p(\eta) \bar{\delta}(\bar{\theta}(\theta_1, \theta_2) + \eta - \theta), \quad (2.8e)$$

where the stochasticity of collisions (later shortly referred to as collision noise) is modeled by a Gaussian distribution $p(\eta)$ with a standard deviation σ . Collision noise can, for example, arise from the particles' neglected spatial arrangements characterized by the impact parameter. The kernel of the collision integrals [Eq. (2.8d) and Eq. (2.8e)] involves a measure for the rate of collisions **(i)**, denoted as $\Gamma(\theta_1, \theta_2)$, as well as a *collision rule* **(ii)**, $\bar{\theta}(\theta_1, \theta_2)$, implementing a mapping between pre- and post-collision orientations of the two colliding particles.

(i) The rate of collision, also referred to as *Boltzmann scattering cylinder*, is, as follows, derived on geometrical grounds for spheres assuming a completely uncorrelated, isotropic and homogeneously distributed state: Consider a collision between two particles with orientations θ_1 and θ_2 . Given short-ranged repulsive interactions, the two spherical particles collide if their relative distance becomes less than the particles' diameter d . Going into the reference frame of e.g. particle 2, the velocity of particle 1 is given by the relative velocity $\mathbf{v}_{12} = v_0 [\hat{\mathbf{v}}(\theta_1) - \hat{\mathbf{v}}(\theta_2)]$. A collision between the two particles occurs within the time interval $[t, t + dt]$ if particle 1 can be found in a rectangle of length $|\mathbf{v}_{12}| dt$ and width $2d$. Back in the laboratory frame, this rectangle deforms into a parallelogram retaining its surface area given by $2dv_0 |\hat{\mathbf{v}}(\theta_1) - \hat{\mathbf{v}}(\theta_2)| dt =: \Gamma(\theta_1, \theta_2) dt$ [15, 16]. This function is commonly referred to as *Boltzmann collision cylinder* and determines the rate of collisions in the uncorrelated (pre-collision) state for spherical particles moving ballistically in two dimensions. The function Γ depends solely on the relative angle θ_{12} , and can be written as follows:

$$\Gamma(\theta_{12}) = 4dv_0 |\sin(\theta_{12}/2)|. \quad (2.8f)$$

(ii) The *collision rule* can be measured experimentally, or can be obtained from simulation or just postulated. In Refs. [7, 15, 6, 16], a very simplistic collision rule, from now on termed as “half-angle alignment rule”, is used [see Fig. 2.21(a) for an illustration]:

$$\bar{\theta}(\theta_1, \theta_2) = \frac{1}{2} (\theta_1 + \theta_2), \quad (2.8g)$$

which is commonly [7, 15, 6, 16] used for all relative angles $\theta_{12} = \theta_1 - \theta_2 \in [0, \pi]$ (maximal angular interaction range). Equations (2.8a)–(2.8g) constitute the kinetic theory for propelled particle systems as proposed by Refs. [15, 16]. The central control parameters are: noise level, characterized by the single particle noise σ_0 and the collision noise σ , and the homogeneous density $\rho_0 = 2\pi f_0$ [f_0 : homogenous one-particle density]. Before we discuss the open questions, we will give a short overview of the most important results of kinetic theory for propelled particle systems.

Properties & Results

- **conservation of particle number:** Noting that the hydrodynamic density $\rho(\mathbf{r}, t) = \int_{-\pi}^{\pi} d\theta f(\mathbf{r}, \theta, t)$ and the hydrodynamic velocity $\mathbf{u}(\mathbf{r}, t) = \frac{v_0}{\rho(\mathbf{r})} \int_{-\pi}^{\pi} d\theta f(\mathbf{r}, \theta, t)$, simple integration leads to the continuity equation,

$$\partial_t \rho + \nabla \cdot (\rho \mathbf{u}) = 0, \quad (2.9)$$

implying that particle number is conserved.

- **continuous equation for the momentum field:** The equations for the momentum field $\boldsymbol{\tau} = \rho \mathbf{u}$ can be regarded as *Navier-Stokes Equations*, for which conservation of momentum as well as Galileian invariance is broken. For a complete presentation of these equations and their derivation, we refer the reader to Refs. [15, 16]. Here, for the sake of brevity, we neglect all gradient terms, leading to the following hydrodynamic equations:

$$\partial_t \boldsymbol{\tau} = \nu \boldsymbol{\tau} - \gamma \boldsymbol{\tau}^2 + \mathcal{O}(\nabla \boldsymbol{\tau}, \nabla \rho), \quad (2.10)$$

where ν and γ constitute two kinetic coefficients that are fully determined by the control parameters σ_0 , σ and ρ_0 , as well as all microscopic properties such as particle size d , speed v_0 , and the collision rule Eq. (2.8g). From Eqs. (2.10) two important predictions can be made:

- (i) **Phase Boundary:** Since the kinetic coefficient $\nu < 0$ as a function of the control parameters changes²⁴ sign [15, 16], a homogeneous states with $\boldsymbol{\tau} = 0$ becomes unstable, and tends toward a polarized state with a finite polarization. The manifold in the control parameter space $(\sigma_0, \sigma, \rho_0)$ for which $\nu(\sigma_0, \sigma, \rho_0) = 0$ determines the *phase boundary* between the *isotropic* and *polarized* state²⁵, with

$$\rho_t(\sigma_0, \sigma) \Big|_{\nu=0}$$

defining the *transition density* or the *critical single particle noise*

$$\sigma_{0,c}(\rho_0, \sigma) \Big|_{\nu=0}.$$

²⁴Small values of σ_0 [or σ] or large enough values for ρ_0 lead to $\nu > 0$.

²⁵Strictly speaking, the homogeneously distributed, polarized state is *not* stable with respect to spatially inhomogeneous perturbations; for this see next set of bullet points.

- (ii) **Existence of Fixed Points:** For $\nu > 0$, there is a stationary fixed point with $\boldsymbol{\tau}_0 = \tau_0 \mathbf{e}$, where \mathbf{e} denotes some arbitrary broken symmetry axis, and the value of the fixed point is given by $\tau_0 = \sqrt{\nu/\delta}$.
- **Predictions of the Inhomogeneous Equations:** Testing the inhomogeneous equations (refer to [15, 16]) against wave-like perturbations $\propto e^{i\mathbf{q}\cdot\mathbf{r}}$ [\mathbf{q} : wave number] leads to the following central findings:
 - (i) **Long Wave Length Instability:** The *isotropic* state $\boldsymbol{\tau}_0 = 0$ undergoes a long wave length instability, with $\mathbf{q} = 0$ as the fastest growing mode (type III_s instability according to ref. [26]). This finding allows us to restrict to Eq. (2.10) to determine the phase boundary²⁶.
 - (ii) **Longitudinal Modes in the Polarized State:** For $\rho > \rho_t$ a spatially homogeneous, polarized state with $\boldsymbol{\tau} = \boldsymbol{\tau}_0$ is unstable with respect to longitudinal perturbations. These perturbations are parallel to the wave vector \mathbf{q} and the fixed point polarization $\boldsymbol{\tau}_0$. The corresponding longitudinal modes are the most unstable ones, *i.e.* their growth rates are larger than any other modes. It is expected—but not proven—that these modes give rise to a polarized state with a stationary wave-like spatial pattern, as already found earlier in agent-based simulation such as the Vicsek-model [23]. Specifically, Bertin et al. [16] showed that the Boltzmann equation [Eq. (2.8)] supports a solitary wave solution, however, stability of this solution has not been analyzed so far.

2.3.3 Kinetic Theory for Propelled Particle Systems: Open questions

In this section we give a short list of open questions in kinetic theory for propelled particle systems given by Eqs. (2.8), bridging the gap between the last section and the research work performed, which is discussed throughout the subsequent sections:

The *Boltzmann cylinder* Eq. (2.8f), which determines the rate of binary collisions, is related to spherical particles, therefore, naturally the following question arises:

- (1) What is the *Boltzmann collision cylinder* for *rod-like* propelled particles, and is there an impact on the ordering transition due to the rod shape? → section 2.3.4

Furthermore, the Boltzmann equation Eq. (2.8) deals with a single particle species, with the corresponding particle number being conserved. Therefore, it is natural to ask:

- (2) Are the patterning instabilities affected (*e.g.* the longitudinal instability) when the total particle number is not conserved? → section 2.3.5

²⁶An instability with a characteristic mode, *e.g.* Rayleigh–Bénard convection, requires to include the gradient terms in order to predict the regions in the control parameter space with convection roles.

Commonly, propelled particles are assumed to interact on the mesoscopic scale for *all* relative angles ($\theta_{12} \in [0, \pi]$) via the so-called *half-angle alignment rule* (see Eq. (2.8g), and [7, 15, 6, 16]). A number of well-characterized experimental model systems including actin and microtubule gliding assays ([90, 93], and section 2.1), and shaken granular particles ([30, 31], and section 2.2) highlight that actual collisions differ from this generic interaction rule in two important respects: (i) The post-collision particle orientations are not symmetric with respect to the average of the pre-collision directions, but depend on both the relative orientation and relative position of the colliding particles before the collision [Figures 2.19(a) and 2.19(b)]. (ii) Frequently, one finds “indifferent” events where collisions do not change the relative orientations of the collision partners [30, 31]. Therefore, the region of configuration space supporting aligning collisions is restricted, and it is thus far from obvious whether binary, dissipative interactions actually contribute to the formation of order in active systems. This raises an interesting question:

- (3) With no additional assumptions to be made, does the integrated effect of *realistic binary* particle interactions in propelled particle systems suffice to establish a state of collective motion on macroscopic scales? → section 2.3.6

Finally, the Boltzmann approach relies on the fundamental assumption of molecular chaos, *i.e.* it neglects spatial and orientational correlations between the particles which are about to collide (*assumption of molecular chaos*). Using the phase boundaries between the *isotropic* and *polarized* states obtained from molecular dynamics simulations as a benchmark, we ask:

- (4) Are correlations essential for a quantitative agreement between the phase boundaries obtained from kinetic theory and from molecular dynamic simulations. And if so, how is the Boltzmann equation to be modified in order to achieve *quantitatively* correct predictions of kinetic theory under dilute conditions? → section 2.3.7

2.3.4 Particle Length in a Kinetic Description

This section is devoted to the question how the *Boltzmann collision cylinder* changes when particles are of rod shape [refer to Eq. (2.8f) for spheres], and whether the rod shape has an impact on the ordering transition from the isotropic to the polarized phase. In the following we consider sphero-cylindrical rods of length L and diameter d , as illustrated in Fig. 2.20(a), with each rod moving with a constant velocity v_0 . The collision cylinder $\Gamma(L, d, \theta_{12})$ depends on the relative angle θ_{12} and can be derived in an isotropic and homogeneously distributed state by geometrical considerations [cf. Fig. 2.20(a)]: On the scale of the Boltzmann equation, binary collisions occur locally, say in an infinitesimal volume element centered at \mathbf{r} . Assume that particle 1 has an orientation θ_1 . Then, $\Gamma(L, d, \theta_{12}) dt$ gives the area around particle 1 in which every particle with orientation θ_2 will collide during a time interval $[t, t + dt]$ with particle 1. As a consequence $\Gamma(L, d, \theta_{12}) f(\mathbf{r}, \theta_1, t) f(\mathbf{r}, \theta_2, t) d\theta_1 d\theta_2$ equals the number of collisions per unit time and unit area at time t and position \mathbf{r} for

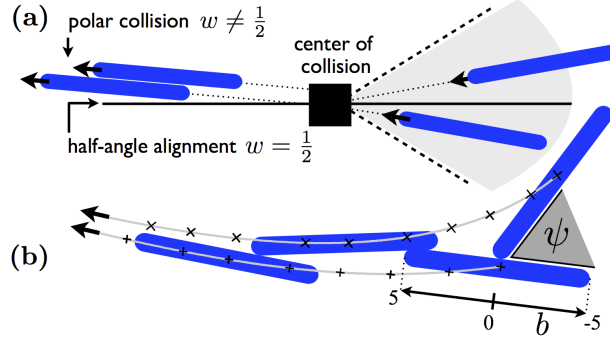


Figure 2.19: **(a)** Rod interactions within an angular alignment range $\bar{\psi}$ (grey shaded) lead to polar alignment, whose direction typically deviates from the half-angle alignment. **(b)** Simulated example trajectory for a model of propelled rigid rods (relative angle $\psi \approx \pi/3$, impact parameter $b \approx 0$ in units of rod diameter, $w(\pi/3, 0) \approx 1.3$). For definition of w , refer to Eq. (2.22) and the corresponding section. Details on the model used to create the depicted trajectories are detailed in **publication B.7**.

two colliding particles with orientations θ_1 and θ_2 , with $f(\mathbf{r}, \theta, t)$ denoting the one-particle distribution function. To determine $\Gamma(L, d, \theta_{12})$, we take a microscopic point of view. Since the model employed in this work assigns to each particle a velocity vector pointing along its rod axis, we can distinguish “head” and “tail”. Referring to Fig. 2.20(a), without loss of generality, we assume $\pi - \theta_{12} \equiv \theta \in [0, \pi]$ (negative relative angles lead to the same result), and consider the blue rod, with the position of its head indicated by the blue dot. All rods of relative orientation $\theta_{12} = \theta_1 - \theta_2$, and with their heads lying in the area $S = A \cup S_1 \cup S_2$ at time t , will collide with the blue rod during the time interval $[t, t + dt]$. Since A , S_1 and S_2 are disjoint²⁷,

$$|S| = |A| + |S_1| + |S_2|, \quad (2.11)$$

where $|X|$ denotes the area of the region X . The respective areas are given by:

$$|A| = dt v_{\text{rel}} (L - d) |\sin \theta| = dt v_{\text{rel}} (L - d) |\sin \theta_{12}|, \quad (2.12)$$

and

$$|S_2| + |S_1| = dt v_{\text{rel}} d \int_{-\theta}^{\pi-\theta} d\phi \sin(\phi + \theta) = 2 dt v_{\text{rel}} d. \quad (2.13)$$

Returning to the laboratory frame, we have $v_{\text{rel}} = v_0 |\hat{\mathbf{v}}(\theta_1) - \hat{\mathbf{v}}(\theta_2)| = 2 v_0 |\sin(\theta_{12}/2)|$. Noting that $\Gamma = |S|/dt$ [cf. Eq. (2.11)], we find²⁸:

$$\Gamma(L, d, \theta_{12}) = 4v_0 d \left| \sin \left(\frac{\theta_{12}}{2} \right) \right| \left(1 + \frac{\xi - 1}{2} |\sin \theta_{12}| \right), \quad (2.14)$$

²⁷Implicitly, we also assumed that the rods move ballistically, therefore we neglected angular changes by noise within the collision cylinder.

²⁸Preliminary investigations of binary collisions of short ($\sim 5\mu\text{m}$) actin filaments in the gliding assay indicate that the calculated characteristics as a function of length (shift of maximum to smaller relative angles, zero at $\theta_{12} = 0$) is also found experimentally (private communications with Ryo Suzuki).

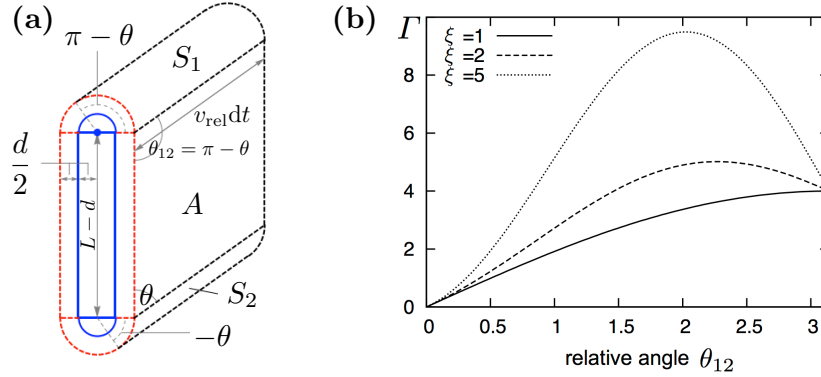


Figure 2.20: **(a)** Illustration of the collision cylinder in the rest frame of the blue rod. The red lines indicate the excluded volume due to the finite expansion of the rods. The quantity v_{rel} denotes the magnitude of the relative velocity of those rods making a relative angle $\theta_{12} = \pi - \theta$ with the blue rod's axis, and is given by $v_{\text{rel}} = v_0 |\hat{\mathbf{v}}(\theta) - \hat{\mathbf{v}}(0)| = 2v_0 |\sin(\theta_{12}/2)|$. **(b)** $\Gamma(L, d, \theta_{12})$ as a function of the relative angle θ_{12} for different values of aspect ratio $\xi = L/d$. For the figure, we chose for particle width $d = 1$ and for particle velocity $v_0 = 1$. Increasing the aspect ratio ξ , the most probable collision approaches $\theta_{12} = \pi/2$, whereas for $\xi = 1$ the most probable collision shifts towards $\theta_{12} = \pi$.

Integral	$I_{0,0}$	$I_{1,0}/I_{0,0}$	$I_{1,1}/I_{0,0}$	$I_{2,0}/I_{0,0}$	$I_{2,1}/I_{0,0}$
Value	$\frac{8dv(2+\xi)}{3\pi}$	$-\frac{4+\xi}{5(2+\xi)}$	$\frac{3}{16} \frac{8+\pi(\xi-1)}{2+\xi}$	$\frac{6-13\xi}{35(2+\xi)}$	$\frac{3}{16} \frac{\pi(1-\xi)-8}{2+\xi}$

Table 2.1: Summary of relevant collision integrals $I_{n,k}$ as a function of the aspect ratio $\xi = L/d$, where d denotes the particle diameter and v is the particle velocity. The quantities $I_{n,k}/I_{0,0}$ depend only weakly on the aspect ratio ξ . In particular, the signs of $I_{n,k}/I_{0,0}$ do not change with ξ , leaving all our present conclusions (see section 2.3.2, Properties & Results) made on the basis of the Boltzmann equation (2.8) qualitatively unchanged.

where $\xi = L/d$ denotes the aspect ratio. In Fig. 2.20(b), $\Gamma(L, d, \theta_{12})$ is shown as a function of relative angle θ_{12} for different particle lengths, whereby the particle width d is kept fixed. In the case of a sphere, *i.e.* $\xi = 1$, head-on collisions ($\theta_{12} = \pi$) are most probable because those lead to the largest value of the relative velocity v_{rel} . Increasing the aspect ratio ξ shifts the most probable collision from $\theta_{12} = \pi$ towards $\theta_{12} = \pi/2$ for $\xi \rightarrow \infty$. This limiting case is equal to a needle for which the largest target area is exposed for θ_{12} slightly²⁹ larger than $\pi/2$.

Now let us turn to the question whether the rod-like characteristics embodied in $L/d > 1$ and described by Eq. (2.14) have an impact on the ordering transition. To this end, we have to give a short digression on how the hydrodynamic equations [*e.g.* Eqs. (2.10) for the homogeneous state] are obtained from the Boltzmann equation (2.8). First, the Boltzmann

²⁹Note that the maximum of the relative velocity v_{rel} for $\theta_{12} = \pi$ prohibits Γ to be maximal for $\theta_{12} = \pi/2$ in the limit of infinitely long rods. The maximum of Γ for $\xi \rightarrow \infty$ is at $\theta_{12} \approx 1.91$.

equation is Fourier transformed, with $\hat{f}_k(\mathbf{r}, t) = \int_{-\pi}^{\pi} d\theta e^{ik\theta} f(\mathbf{r}, \theta, t)$, leading to:

$$\begin{aligned} \partial_t \hat{f}_k + \frac{v_0}{2} \left[\partial_x (\hat{f}_{k+1} + \hat{f}_{k-1}) - i\partial_y (\hat{f}_{k+1} - \hat{f}_{k-1}) \right] = \\ - \lambda \left(1 - e^{-k^2 \sigma_0^2 / 2} \right) \hat{f}_k - \sum_{q=-\infty}^{\infty} \left(I_{n,0} - e^{-k^2 \sigma^2 / 2} I_{n,k} \right) \hat{f}_q \hat{f}_{k-q}, \end{aligned} \quad (2.15)$$

where we suppressed the reference to time space coordinates for brevity. The coefficients $I_{n,k}$ are given by:

$$I_{n,k} = \frac{1}{2\pi} \int_{-\pi}^{\pi} d\theta \Gamma(L, d, |\theta|) \cos \left[\left(n - \frac{k}{2} \right) \theta \right]. \quad (2.16)$$

Then, the Fourier space representation of the Boltzmann equation Eq. (2.15) lends itself as a starting point to the derivation of the hydrodynamic equations by an appropriate truncation of the Fourier representation. For details on the truncation scheme we refer the interested reader to refs. [16], **publication B.5, B.7 or B.8**. Importantly, since all kinetic coefficient in the hydrodynamic equations are fully determined by the coefficients $I_{n,k}$, one can already understand the impact of L/d by rescaling the Fourier space Boltzmann equation (2.15). To this end we introduce following characteristic scales for time and space:

$$\hat{\tau}_\lambda = \lambda^{-1} \quad \text{and} \quad \hat{\ell}_e = v/\lambda. \quad (2.17)$$

Noting that $I_{0,0}$ is equal to the *total scattering cross section*, the characteristic scale for the one-particle distribution can be constructed from the noise time scale $\hat{\tau}_\lambda$: $\hat{f} \rightarrow \hat{f} \cdot I_{0,0} \hat{\tau}_\lambda$, which gives as scaling for the $I_{n,k}$:

$$I_{n,k} \rightarrow I_{n,k} \cdot \frac{1}{I_{0,0}}. \quad (2.18)$$

These coefficients $I_{n,k}$ which are essential in the derivation for the momentum field equation (see **publication B.5** for details on the derivation) are depicted in table 2.1. Importantly, the signs of $I_{n,k}/I_{0,0}$ do not change with $\xi \geq 1$, leaving all predictions (see section 2.3.2, Properties & Results) made on the basis of the Boltzmann equation (2.8) qualitatively unchanged. This suggests that the effect of particle shape is merely quantitative and affects “only” the values for transition density or the fixed point.

2.3.5 Role of Particle Conservation for Propelled Particle Systems

In this section we address the significance of constraints for particle number by highlighting the differences in the collective properties between particle conserving systems and those in contact with a particle reservoir. Our focus will be on the comparison of two archetypical scenarios, which we will refer to as the *canonical* (particle conserving), and the *grand canonical* (violating particle conservation) scenarios, respectively.

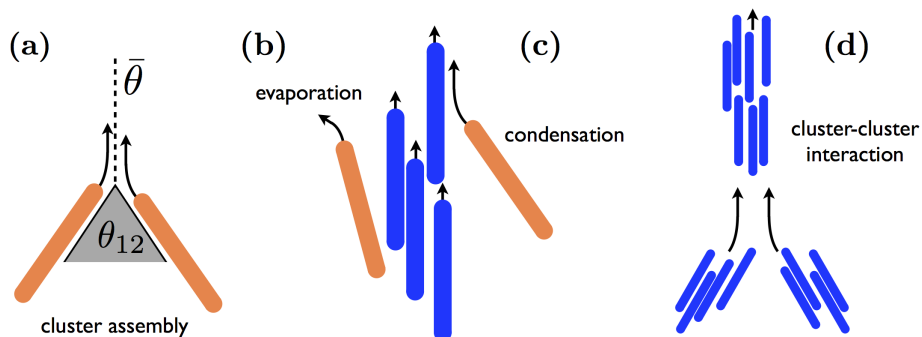


Figure 2.21: **(a) Cluster assembly:** Illustration of two single particle species (light orange) with a pre-collisional relative angle of θ_{12} , colliding such that they align collinear to the average angle $\bar{\theta}$ (*half angle alignment rule*). Both particles assemble to a cluster species (indicated in blue) after the collision. **(b) Evaporation:** A particle leaves the cluster by a random change of its direction at a characteristic rate. **(c) Condensation:** A single particle joins a cluster by perfectly aligning to the cluster particles (blue). **(d) Cluster-cluster interaction:** In our modeling framework clusters are assumed to interact via half-angle alignment.

To this end, we will resort to the kinetic approach given by Eqs. (2.8) for propelled particle systems and extend this description. Specifically, we are led by a physical picture of collective motion that has been developed over the last decade based on observations in agent-based simulations of locally interacting, particle conserving systems [40, 23, 75, 107]. Among the most pertinent phenomena that have been reported in the context of these studies is the formation of intricate local structures pervading these systems in the vicinity of the ordering transition: Densely packed cohorts of coherently moving particles—subsequently referred to as *clusters*—incessantly “nucleate” and “evaporate” on local scales, even below threshold, rendering the system isotropic and homogeneous only in the limit of macroscopic length scales. Individual particles exhibit superdiffusive behavior in this regime, performing quasi-ballistic “flights” as long as they are part of a cluster, and undergoing conventional particle diffusion if they are not. Above threshold, collective motion manifests itself on macroscopic scales in the form of coherently moving and dense bands, which are submersed in an isotropic low-density “particle sea”. Spatially homogeneous flowing states, in contrast, are observed only well beyond the ordering threshold [40].

In light of the above, we suggest a simplified modeling framework be implemented in kinetic theory in order to incorporate the intricate role of clusters on the ordering behavior (for technical details please refer to **publication B.5**):

Particles interact via binary collisions with a scattering cross section which is explicitly derived as a function of particle shape [see Eq. (2.14)]. Depending on whether a given particle is part of a cluster or not, it will be associated with one of two distinct particle classes, which we will refer to as the class of *cluster particles* and the class of *single particles*, respectively. Based on this two-species framework, we propose the following type of

interactions among the species of equivalent and different type [refer to Fig. 2.21]:

(a) *Single particles* are “converted” to *cluster particles* by “cluster assembly” every time two *single particles* collide with each other, with their post-collision orientations determined by the *half-angle alignment rule*. Conversely, (b) *cluster particles* are “converted” back to *single particles* by an “evaporation” process, which we assume to occur at some constant (possibly particle shape dependent [75]) rate. (c) *Single particles* can join the cluster by “condensation”, *i.e.* they perfectly align to the cluster’s direction of motion. (d) *Cluster particles* interact with each other via half-angle alignment³⁰. All inter-particle collisions are assumed to involve an interaction noise of amplitude σ [analog to Eq.(2.8e)]. Moreover, in the absence of interactions, *cluster particles* will be assumed to move ballistically, whereas *single particles* will be assumed to perform random walks. Taken together, the conversion dynamics and the class-specificity of particle motion provide a simple way to implement the typical superdiffusive behavior of individual particles that was alluded to above.

To assess the importance of particle conservation in the context of pattern formation, we analyzed two variants of this model: First, we studied closed systems in which the total number of particles is conserved (*canonical* scenario) and where, consequently, the denser cluster phase grows at the expense of the single phase. Secondly, we examined open systems in contact with a particle reservoir (*grand canonical* scenario), where the particle current out of the single phase is compensated for so as to retain the density of the isotropic sea of *single particles* at a constant level; *cf.* Fig. 2.23.

Inspecting the corresponding hydrodynamic equations (for details on the derivation, please refer to **publication B.5**), we were able to establish the following physical picture, portraying the formation of collective motion via dissipative particle interactions. For both, the *canonical* and the *grand canonical* model, we identified two characteristic density scales $\bar{\rho}$ and $\rho^{(c)}(\sigma)$, with $\rho^{(c)}(\sigma) > \bar{\rho}$, which allowed us to distinguish three density regimes. These are illustrated in Fig. 2.22, with *single particles* and *cluster particles* depicted by orange dots and blue arrows, respectively.

- (i) For low densities, $\rho < \bar{\rho}$, the rate at which particles collide is much smaller than the rate at which clusters disassemble. In terms of a particle based picture, this regime corresponds to a situation, where particle clusters are unstable, evaporating shortly after their nucleation. In the stationary state, the vast majority of particles populates the *single particle* phase, rendering the system homogeneous and isotropic even on mesoscopic scales. This low density regime terminates at the characteristic density $\bar{\rho}$, where both classes exchange particles at equal rates.
- (ii) In the contiguous regime of intermediate densities, $\bar{\rho} < \rho < \rho^{(c)}$, the overall rate of cluster formation and growth outstrips the rate at which clusters evaporate, and the majority of particles become organized in clusters. Translated to a particle based

³⁰Usually, the outcome of a cluster-cluster interaction is an intricate process involving disassembly events and in general leads to a cluster size/mass dependent post-collisional orientation [75]. However, within our simplified framework of two species, those processes are neglected.

notion, clusters grow to finite sizes and persist over macroscopic time scales. Clusters of coherently moving particles now dominate the physical picture on mesoscopic scales. Yet, interactions among clusters are too rare to establish a macroscopic state of collective motion. On hydrodynamic length scales, the system can be viewed as a homogeneous and isotropic sea of clusters.

- (iii) For densities exceeding the critical density, $\rho > \rho^{(c)}(\sigma)$, collisions within the cluster phase occur at sufficiently high rates and macroscopic collective motion emerges. The homogeneous and isotropic state, which has been shown to be stable within the two preceding regimes, thus becomes unstable and rotational symmetry is spontaneously broken.

While the qualitative features of the *canonical* and the *grand canonical* model are the same in the low and the intermediate density regime ($\rho < \rho^c$), the establishment of collective motion in the high density ($\rho > \rho^c$) regime differs in important respects in both models:

We found that in the *grand canonical* model, a broadly extended region in parameter space exists, where a spatially homogeneous state of macroscopic collective motion exists and is actually stable. Except density, the key parameter controlling the stability of a spatially homogeneous flowing state is the noise amplitude σ . For low noise levels the homogeneous flowing state is destabilized by transverse perturbations³¹ (*i.e.* perturbations with wavevectors \mathbf{q} perpendicular to the direction of the macroscopic flow). Interestingly, this transverse instability vanishes altogether if angular diffusion is slightly enhanced by increasing σ . Hence, for these noise values, the system directly establishes a homogeneous state of collective motion, which is stable with respect to arbitrary perturbations of small magnitude.

In the case of the *canonical* model, a spatially homogeneous base state is destabilized by longitudinal perturbations (*i.e.* perturbations with wavevectors \mathbf{q} parallel to the direction of the macroscopic flow) for all values of the noise parameter σ . Both the magnitude of the macroscopic velocity field and the particle density are prone to this kind of instability. This is in agreement with previous analytical [16] and numerical [40] results for particle conserving systems where the emergence of solitary wave structures has been reported to

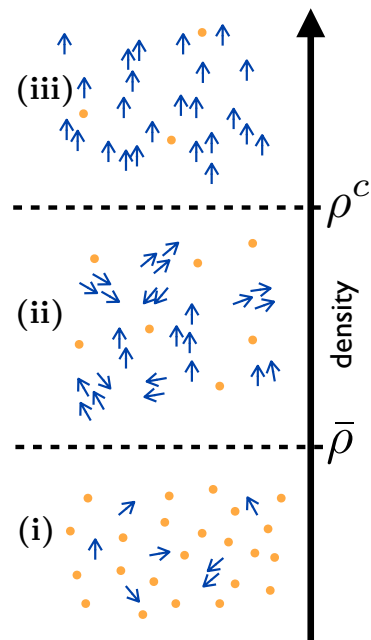


Figure 2.22: Illustration of the three clustering regimes.

³¹We note, however, that these instabilities are remarkably weak, meaning that the corresponding growth rates are smaller than those of the longitudinal instability in the *canonical* model by a factor of ~ 10 . All results are obtained via a standard linear stability analysis, hence speculation about the resulting stationary pattern must be taken with a grain of salt. An appropriate answer of the role of the transversal instability could only be given by a numerical solution of the kinetic equations, which is currently in progress.

be in the vicinity of the ordering transition $\rho \sim \rho^{(c)}(\sigma)$. The longitudinal instability thus seems to be quite a generic feature of particle conserving systems with short-ranged (metric) interactions. For an interesting counterexample we refer the reader to Ref. [80], where a particle conserving system with topological interactions has been studied.

We can now combine our findings for both the *canonical* and the *grand canonical* model, to offer the following mechanistic explanation concerning the emergence of the longitudinal instability. The prerequisite underlying the establishment of coherent motion is embodied by two basic processes: Cluster nucleation by collisions among *single particles*, and cluster growth by alignment of *single particles* to clusters. Only if, by virtue of these processes, the concentration of *cluster particles* reaches a sufficient size clusters are able to synchronize their movements by coagulation. Macroscopic collective motion then emerges. In the following, we will consider the effect of a density fluctuation in a homogeneous state of macroscopic collective motion which shall be described by the equations for a homogeneous state. For the two scenarios considered, the corresponding hydrodynamic equations are (derivation see **publication B.5**):

- In the case of the *grand canonical* model we find

$$\partial_t \rho_c = \underbrace{-\rho_c}_{\text{evaporation}} + \underbrace{\rho_s^0 \rho_s^0}_{\text{cluster assembly}} + \underbrace{\rho_c \rho_s^0}_{\text{condensation}}, \quad (2.19)$$

where ρ_c denotes the density of *cluster particles*, and ρ_s^0 is the constant particle density of the *single particles*. The superscript “0” indicates that the single particle density ρ_s is a non-dynamical quantity. The terms on the r.h.s. describe evaporation ($\propto -\rho_c$), cluster assembly ($\propto \rho_s^0 \rho_s^0$) and condensation ($\propto \rho_s \rho_c$), respectively. Analyzing the fixed point of the hydrodynamic equations leads to the condition $\rho_s^0 < 1$ for all finite values of the total particle density ρ .

- For the *canonical* model we obtain

$$\partial_t \eta = \underbrace{\rho(\rho - \eta)}_{\text{assembly and condensation}} - \underbrace{(\eta + \rho)}_{\text{evaporation}}, \quad (2.20)$$

with $\rho = \rho_s + \rho_c$ as the total particle number density and $\eta = \rho_c - \rho_s$ [ρ_s : *single particle density*]. The first term on the r.h.s. describes cluster assembly ($\propto \rho_s^2$) and condensation ($\propto \rho_s \rho_c$), and the second term corresponds to cluster evaporation ($\propto -\rho_c$).

Let us start with the mechanistic explanation for the absence of the longitudinal instability in the *grand canonical* model. To this end, we consider a polarized state with a homogeneous density of *cluster particles* ρ_c^0 and assess the implications of fluctuations on the *cluster particles* by writing $\rho_c = \rho_c^0 + \delta\rho_c$, which by virtue of Eq. (2.19), leads to:

$$\partial_t \delta\rho_c = -\delta\rho_c \underbrace{(1 - \rho_s^0)}_{>0}. \quad (2.21)$$

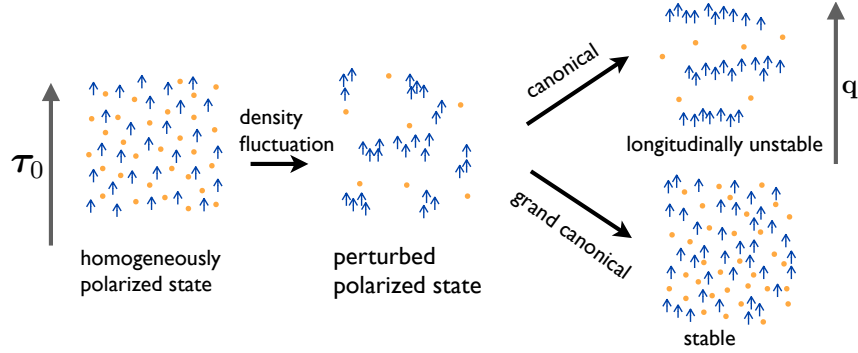


Figure 2.23: Illustration of the *canonical* and *grand canonical* modeling framework, highlighting the quintessential differences in the context of pattern formation. In the homogeneously polarized state (left), the *cluster particles* density (blue arrows) constitutes the system’s macroscopic net momentum τ_0 , while some fraction of the system’s particles, the *single particles* (orange dots) exhibit zero net momentum. Spatial perturbations of both density fields lead to two fundamentally different outcomes: (i) In case of a closed system obeying total particle conservation (*single particles* and *cluster particles*), termed the *canonical* model, the homogeneously polarized state is longitudinally unstable, with a wave vector \mathbf{q} parallel to the polarized state τ_0 , potentially enforcing a wave-like pattern. (ii) In contrast, open systems (*grand canonical* model) turn out to be stable against this kind of density fluctuations.

As can be seen from this equation, locally enhancing ($\delta\rho_c > 0$) the density of *cluster particles* implies a net current from the *cluster particle* phase into the *single particle* phase, thus counteracting the effect of the original density fluctuation. Conversely, locally diminishing ($\delta\rho_c < 0$) the density of *cluster particles* leads to the opposite effect. Density fluctuations are thus damped in the *grand canonical* model (see Fig. 2.23 for an illustration) and do not impact the macroscopic velocity field, which is set up by the *cluster particles*.

Exactly the opposite happens in the particle conserving *canonical* model. Again, consider a spatially homogeneous base state of macroscopic collective motion. Particles are then distributed among the phases of *cluster particles* and *single particles* as determined by the balance equation $\rho(\rho - \eta) = \rho + \eta$ [cf. Eq. (2.20)]. Now, consider a small fluctuation in the total density ρ , *i.e.* $\rho \rightarrow k\rho$, where, for the sake of simplicity, the relative density η is assumed to remain constant. In regions, where the fluctuation leads to an increase in the total density by a factor $k > 1$ we have $k\rho(k\rho - \eta) > k\rho + \eta$, which leads to $\partial_t\eta > 0$ [with $\eta = \rho_c - \rho_s$]. Hence, the number of particles in the *cluster particle* phase grows. Since the *cluster particles* are the “carriers” of the macroscopic momentum, the local value of the momentum current density increases. In contrast, in regions where the fluctuation decreases the total density by a factor $k' < 1$ we have $k'\rho(k'\rho - \eta) < k'\rho + \eta$, yielding $\partial_t\eta < 0$. Therefore, the *cluster particle* phase gets depleted and the local magnitude of the momentum current density declines. As a result, high density regions move at faster speeds than low density regions, gathering more and more particles on their way through

the system. Conversely, lower density regions continually lose particles to the faster high density structures. In particle conserving systems, every density fluctuation thus automatically triggers a corresponding fluctuation in the momentum current density, which in turn amplifies the density fluctuation. As a result of this process, high density bands of collectively moving *cluster particles* might emerge [40] (see Fig. 2.23 for an illustration). These bands are interspersed by regions where the particle density has fallen below the critical density $\rho^{(c)}$ (and possibly below $\bar{\rho}$), leading to local destruction of clusters and collective motion.

2.3.6 Non-perfect Active Collisions: Deviations from Half-angle Alignment

In this section the aim is to establish an appropriate kinetic description of the collision process observed experimentally in gliding assays [90, 93] and shaken granular particles [30, 31] by generalizing the popular [7, 15, 6, 16, 79] *half-angle alignment rule* [Eq. (2.8g)]. Since in these experimental systems the particle speed is mostly constant, it is sufficient to describe each collision by the impact parameter b capturing the particles' relative spatial arrangements, and a pre- and post-collision angle for each particle, θ_i and θ'_i ($i \in \{1, 2\}$), respectively. As already mentioned in section 2.3.3, these experiments highlight that actual collisions differ from the *half-angle alignment rule* in two important respects:

- (i) Collisions may be classified either as “indifferent”, where the relative scattering angle remains virtually unchanged ($\theta'_{12} \approx \theta_{12}$), or “polar alignment” events with $\theta'_{12}=0$. In general these two regimes are delineated by a rather sharp boundary $\psi_{\max}(b)$ in the b - θ_{12} space. For simplicity, we approximate this boundary by a single angle $\bar{\psi} = \max_b \psi_{\max}(b)$, which we refer to as the *effective alignment range*.
- (ii) Within the alignment range ($\theta_{12} \leq \bar{\psi}$), the post-collision angle θ'_{12} is in general an intricate function of the pre-collision angles and the impact parameter b . Due to rotational invariance it is of the form $\theta' = w(\theta_{12}, b) \theta_1 + [1 - w(\theta_{12}, b)] \theta_2$, where $w(\theta_{12}, b)$ can be interpreted as a *microscopic alignment weight* characteristic of the respective system or model considered. Since we are aiming at a Boltzmann approach which does not resolve length scales comparable to the size of single particles, we adopt a mean-field approach and average over all impact parameters to introduce a *mesoscopic alignment weight* $w(\theta_{12}) := \langle w(\theta_{12}, b) \rangle_b$. It defines the relative magnitude of the pre-collision angles in the post-collision angle:

$$\theta' = w(\theta_{12}) \theta_1 + [1 - w(\theta_{12})] \theta_2. \quad (2.22)$$

Taken together, the alignment range $\bar{\psi}$ and the alignment weight $w(\theta_{12})$ constitute a *generalized mesoscopic scattering rule*. It accounts for indifferent scattering events as well as deviations from half-angle alignment [$w = \frac{1}{2}$, cf. Eq. (2.8g)]. Additionally, numerically

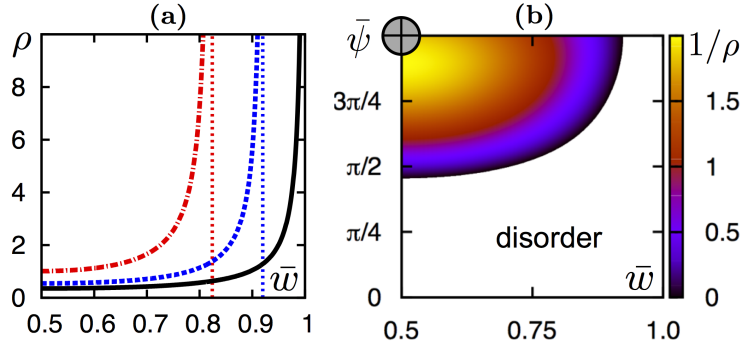


Figure 2.24: **(a)** Transition density ρ_t as a function of collision parameter \bar{w} : Curves from left to right (dash-dotted, dashed, solid) correspond to $\sigma = \{0.7, 0.5, 0\}$ with $\bar{\psi} = \pi$. **(b)** $\rho_t^{-1}(\bar{w}, \bar{\psi})$ for $\sigma = 0.5$. The limiting case of half-angle alignment is depicted by the cross at the top left corner. Parameters for **(c)** and **(d)**: $L/d = 1$, $\sigma_0 = 0.5$.

investigating two archetypical models for propelled rods also confirms the need for the extensions **(i)** and **(ii)** discussed above. For details on the results of these numerical studies please refer to **publication B.7**.

Upon integrating the mesoscopic collision rule into a Boltzmann equation (2.8), but now using Eq. (2.22) instead of Eq. (2.8g) and considering only the integration range for the relative angle³² to $[0, \bar{\psi}]$, we determine the transition density between the isotropic and polarized state, denoted ρ_t , as a function of the interaction range $\bar{\psi}$ and the alignment weight $\bar{w}(\theta_{12})$, finding:

$$\rho_t[w(\psi); \bar{\psi}] = \frac{1 - e^{-\sigma_0^2/2}}{\mathcal{I}_{0,1}[w(\psi); \bar{\psi}] + \mathcal{I}_{1,1}[w(\psi); \bar{\psi}]}, \quad (2.23)$$

where $\mathcal{I}_{1,1}$ and $\mathcal{I}_{0,1}$ denote are Fourier components of the collision integral, which can be defined in analogy to Eq. (2.16) [refer to **publication B.7** for definition and details on the derivation of the above equation]. Importantly, ρ_t depends on the alignment range $\bar{\psi}$ and the alignment weight function $w(\psi)$. However, all functions $\tilde{w}(\psi)$ consistent with $\rho_t[\tilde{w}(\psi); \bar{\psi}] = \bar{\rho}_t$ yield the same location of the ordering transition. Therefore, it is sufficient to consider a constant *alignment weight* \bar{w} with $\bar{\rho}_t = \rho_t[\tilde{w}(\psi); \bar{\psi}] = \rho_t[\bar{w}, \bar{\psi}]$ in order to analyze how the threshold density depends on the characteristic features of the binary collisions³³. The symmetry of the Boltzmann equation (2.8b) with respect to $\bar{w} \rightarrow 1 - \bar{w}$, allows us to consider $\bar{w} \geq 0.5$ without loss of generality.

Fig. 2.24(a) shows the threshold density ρ_t as a function of the alignment weight \bar{w} . For deterministic collisions, $\sigma = 0$, we observe finite but sharply increasing transition densities ρ_t for increasing alignment weights $\bar{w} < 1$ [solid curve in Fig. 2.24(a)]. In the limit

³²The collision integrals Eqs. (2.8d) and (2.8e) can easily be written in terms if the relative angle θ_{12} .

³³That the equation of \bar{w} actually has a unique solution for $\bar{\rho}_t \geq 0$ will be shown in the Supplementary Material of **publication B.7**.

$\bar{w} \rightarrow 1$, the post-collision angle coincides with one of the pre-collision angles, *cf.* Eq. (2.22). This type of binary collision is, on average, equivalent to a specular reflection: Due to particle exchange symmetry, two particles with pre-collision angles θ_1 and θ_2 are both either scattered into θ_1 ($\nearrow\swarrow \rightarrow \nwarrow\nwarrow$) or θ_2 ($\nearrow\swarrow \rightarrow \nearrow\nearrow$). Since both outcomes occur with equal probability, we have $\frac{1}{2}(\nwarrow\nwarrow + \nearrow\nearrow) \equiv \nwarrow\nearrow$, *i.e.* the collision corresponds to a specular reflection. As a consequence, polar order cannot build up from a disordered state, and $\rho_t \rightarrow \infty$ as $\bar{w} \rightarrow 1$. In light of this discussion, the parameter $\bar{w} - 1 \equiv \delta$ can be reinterpreted as an *angular dispersion factor*: While, for $\delta = 0$ the angular distribution remains invariant, for $\delta < 0$, any deviation from an isotropic distribution is amplified by collisions. For $\delta > 0$ the opposite effect is observed. Obviously, the threshold density ρ_t also diverges for $\bar{\psi} \rightarrow 0$ (data not shown), which corresponds to the limiting case where all collisions are indifferent, *i.e.* to non-interacting particles.

Adding stochasticity to the collisions, $\sigma > 0$, the poles of ρ_t are increasingly shifted towards the limiting case $(\bar{w}, \bar{\psi}) = (\frac{1}{2}, \pi)$ corresponding to half-angle alignment over the entire angular range [Figs. 2.24(a) and 2.24(b)]. Surprisingly, to compensate for the dis-aligning effect of collision noise, one needs both a weaker angular dispersion \bar{w} , and a larger alignment range $\bar{\psi}$: Even in the optimal case of half-angle alignment, $\bar{w} = \frac{1}{2}$, any stochasticity during the collision process immediately sets a lower bound for the alignment range $\bar{\psi}$, which cannot be abrogated by increasing collision frequencies. This is illustrated in Fig. 2.24(b) for $\sigma = 0.5$: While parameters $(\bar{w}, \bar{\psi})$ in the colored region are associated with finite threshold densities ρ_t , choosing parameters in the white region renders the system disordered. In other words, the presence of collision noise imposes a ‘minimum efficiency requirement’ on microscopic particle interactions. We also addressed the impact of \bar{w} and $\bar{\psi}$ on patterning capability, and numerically solved the Boltzmann equation (2.8b). For these studies the interested reader is referred to **publication B.7**.

In summary, we have investigated the physics of binary collisions between propelled rod-like particles and their impact on the emergence of polar order within the framework of kinetic theory. To this end, we have introduced a representation of the scattering process in terms of an alignment range $\bar{\psi}$ and a mesoscopic alignment weight $w(\psi)$. Employing a Boltzmann approach this allowed us to determine the transition density ρ_t to polar order as a functional of these quantities, and the collision noise σ . This leads, most importantly, to the following findings: (i) In the absence of collision noise, any collision process with a negative angular dispersion factor δ leads to polar ordered states at sufficiently large densities. (ii) For a finite noise strength, there is a bounded region in the $(\bar{\psi}, \delta)$ -space where polar order is possible. Outside of this parameter region, the physics of binary collisions encoded in the Boltzmann equations not suffice to give rise to a polar ordered state, even at very high densities.

As a consequence, the popular half-angle alignment rule overestimates the effect of binary collisions on the build-up of orientational order. This is indeed the case for the paradigmatic numerical studies of propelled rods and stiff polymers (not shown, refer to **publication B.7**): Upon using the corresponding microscopic scattering functions $\psi_{\max}(b)$ and $w(\psi, b)$, we computed the transition density ρ_t by means of Eq. (2.23). To get a precise estimate we fully accounted for the functional dependence of the collision integrals on

the microscopic alignment weight $w(\psi, b)$, only assuming uniformly distributed collision parameters b . Interestingly, the ensuing threshold densities for both models turn out to be negative. Thus, these systems fail to establish polar order by means of binary collisions alone, despite the fact that the underlying collision dynamics is highly dissipative. However, indirect evidence from various experimental studies [90, 110, 78] suggest that polar order in these systems might still be possible. This would indicate that a Boltzmann theory is inadequate to describe the ordering process for propelled rod-like particles, and one has to seek for mechanisms beyond binary collisions. Possible candidates can be inferred from questioning the basic assumptions underlying Boltzmann’s kinetic approach. In particular, recent numerical and experimental work [75, 107, 78] highlights the importance of nucleation and growth of clusters in the formation of large scale non-isotropic structures. Within clusters, particles are densely packed and move in a coherent manner. This implies that orientational fluctuations of neighbouring cluster particles about the cluster’s axis are strongly correlated. These correlation effects entail an effective ‘stiffness’ of the cluster’s orientation and therefore provide the basis for its growth and, subsequently, the establishment of order. At the same time, such correlations necessarily invalidate the molecular chaos assumption, which is a key ingredient in the derivation of Boltzmann’s equation.

We thus conclude that the kinetic approach we adopted in this work should be applicable to active systems where the formation of order is driven by a gradual reduction in the spread of particle orientations by means of *weakly aligning* binary collisions; *cf.* Fig. 2.25 for an illustration on the validity range. Therein, red areas correspond to outcomes of the depicted pre-collision orientations (indicated by black arrows) for which the Boltzmann equation is invalid. In contrast, systems in which the establishment of order proceeds via the formation of coherently moving clusters, are characterized by the build-up of higher order correlations, whose description lies beyond the scope of Boltzmann’s equation³⁴.

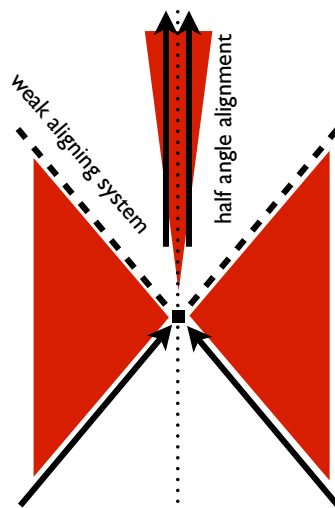


Figure 2.25: Illustration of the validity of the Boltzmann equation.

2.3.7 Scrutinizing Quantitatively Kinetic Theory: Role of Correlations

This section is devoted to a quantitative test of the predictions for the phase boundary obtained from kinetic theory for propelled particle systems. In order to quantitatively scrutinize the underlying Boltzmann equation (2.8) (see *e.g.* section 2.3.2 for an introduction

³⁴The Boltzmann approach can be extended to systems where the molecular chaos assumption can be carried over to a picture of ‘binary’ cluster-cluster interactions as detailed in **publication B.5** or by explicitly accounting for correlations; *cf.* **publication B.8** or section 2.3.7.

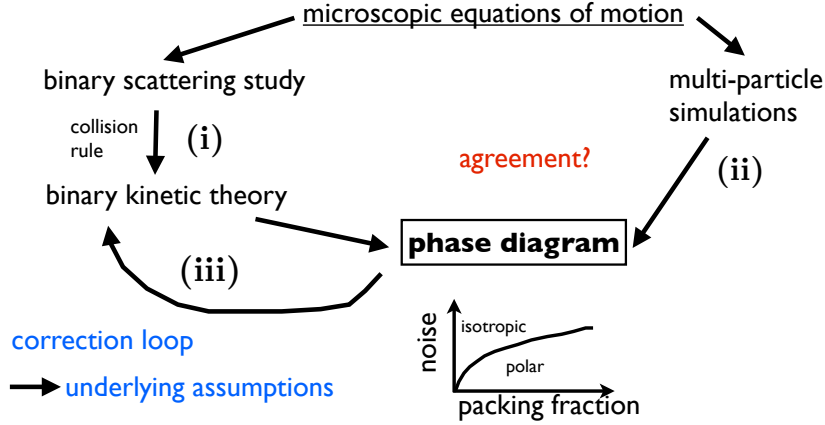


Figure 2.26: Illustration of our “renormalized” kinetic theory (Explanation see text).

on kinetic theory), the collision rule cannot just be postulated, as it is the case for the popular [7, 15, 16] half-angle alignment rule Eq. (2.8g). Instead, we developed a procedure which we call the “renormalized” kinetic theory [see Fig. 2.26]:

First, **(i)** the collision rule is determined from the microscopic equations of motion by studying the details of binary scattering numerically. Second, **(ii)** these equations of motion are used to follow numerically the multi-particle dynamics and compute the phase boundary between *isotropic* and *polar* states. Finally, **(iii)** we employ the collision rule from the binary scattering studies to calculate the phase boundary by means of kinetic theory. Both phase boundaries—from kinetic theory and the multi-particle simulations—are then compared, and in case of any discrepancy, assumptions underlying the kinetic approach can be revised. In particular, it will be interesting to see to what degree the *molecular chaos assumption* [Eq. (2.8a)] of the classical Boltzmann theory remains valid for propelled particle systems.

Let us start with the microscopic equations of motion. In the following, we focus on the dynamics for active colloids in two dimensions [63, 36, 34, 64, 42] in terms of Newtonian equations of motion with the three following forces: An active propelling force capturing the internal propulsion mechanism, which is balanced by a dissipative force accounting for the particle’s loss of kinetic energy. Finally, particles interact by means of a two-body interaction force denoted \mathbf{F}_{ij} . In our studies we restricted ourselves to soft, repulsive interactions. The Newtonian equations of motion read [63, 37, 84, 83]:

$$\frac{d}{d\tau} \tilde{\mathbf{v}}_i = \underbrace{\mu \hat{\mathbf{v}}_i}_{\text{driving}} - \underbrace{|\tilde{\mathbf{v}}_i| \hat{\mathbf{v}}_i}_{\text{dissipation}} + \sum_j \begin{cases} \kappa \tilde{\xi}_{ij} \hat{\mathbf{r}}_{ij} & \text{if } \tilde{\xi}_{ij} \geq 0, \\ 0 & \text{else,} \end{cases} \quad (2.24)$$

where $\tilde{\mathbf{v}}_i = d\tilde{\mathbf{r}}_i/d\tau$ is the dimensionless velocity and $\hat{\mathbf{v}}_i = \mathbf{v}_i/|\mathbf{v}_i|$ is the corresponding unit vector of the velocity. Moreover, repulsive interactions are described by a harmonic repelling force, with $\hat{\mathbf{r}}_{ij} = \frac{\mathbf{r}_i - \mathbf{r}_j}{|\mathbf{r}_i - \mathbf{r}_j|}$ and $\tilde{\xi}_{ij} = \xi_{ij}/d$ is the dimensionless penetration depth. The model includes two parameters: The interaction strength κ and the driving amplitude μ .

(i) In the first step of our “renormalized” kinetic theory we use the above microscopic equations of motion to study the binary scattering dynamics and compute the collision rule. Due to the short-ranged nature of the repulsive interaction potential in Eq. (2.24), one can give a precise definition of the instant when two particles come into contact. Capturing all possible configurations for particle encounters then amounts to defining an appropriate set of parameters describing the geometry at this first moment of contact. For identical particles moving with equal speed, the configuration at the moment of contact (the collision geometry) is completely determined by the relative angle $\theta_{12} = \angle(\mathbf{v}_1, \mathbf{v}_2)$ [Fig. 2.27(a)] and the impact parameter b . The latter is given by $b = -\cos \gamma$, with $\sin \gamma = -\mathbf{v}_{12} \cdot \hat{\mathbf{e}} / |\mathbf{v}_{12}|$ and $\hat{\mathbf{e}} = \mathbf{r}_1 - \mathbf{r}_2 / |\mathbf{r}_1 - \mathbf{r}_2|$ [see Fig. 2.27(b)]. The impact parameter characterizes the type of collision: $b = 0$ signifies a head-on collision in the relative frame or symmetric collision in the laboratory frame, whereas $b = \pm 1$ corresponds to glancing collisions where particles are barely touching each other. For $|b| > 1$ there is no collision. For the scattering studies we prepared the two particles with $b \in [-1, 1]$ and $\theta_{12} \in [0, \pi]$. The results of the scattering study are depicted in Fig. 2.27(c), showing the change in the direction of motion of particle 2, $\Delta\theta_2$ (called scattering angle) as a function of the collision geometry (θ_{12}, b) . We discover a non-trivial, highly non-linear mapping³⁵, which will serve as a starting point for the subsequent kinetic description (see **iii**).

(ii) In the next step of our “renormalized” kinetic theory we employ the equations of motion [Eq. (2.24)] to numerically follow the dynamics of a large number of particles and compute the phase boundary between the *isotropic* and *polarized* states. To this end, the equations of motion are complemented by a stochastic element accounting for noise in the system. Since Brownian noise is irrelevant in active systems [90, 58, 32, 110, 93, 30, 31], we restrict ourselves to a stochastic element that solely leads to fluctuations in the particles’ orientations, *e.g.* Refs. [105, 40, 23, 42]. Specifically, we implement noise as an additive, uncorrelated stochastic force periodically changing the particles’ orientation with a rate λ . The velocity at time t obtained from integrating the deterministic model equations Eqs. (2.24) is then rotated by a Gaussian-distributed random angle η . The Gaussian distribution of the random angle η has zero mean and variance σ_0^2 . In general, the parameters λ and σ_0 together determine the strength of noise in the system. However, for all of our later studies the exact value of the rate λ is not a central issue. To determine the phase-diagram we perform molecular dynamics simulations of a large number of particles of about $N \sim 10^5$ – 10^6 , moving in a square box of linear size $L_{\text{box}} = 250d$ with periodic boundary conditions. Before starting the simulations particles are placed randomly in the simulation box. Overlapping particles are relocated until no more particle overlaps occur³⁶. Particle velocities are initialized in randomized directions with their modulus set equal to the stationary velocity, which is given by μ in dimensionless units. In order to numerically

³⁵Note that, by means of the scattering study we also worked out the underlying principle of alignment and analyzed the alignment tendency as a function of the model parameters κ and μ . For this the interested reader is referred to **publication B.8**.

³⁶For larger packing fractions, this procedure becomes unfeasible. To complete the numerical phase diagram, starting from random positions, we used an over-damped algorithm prior to the actual simulation, where only the interaction forces induce movement until remaining overlaps have been minimized.

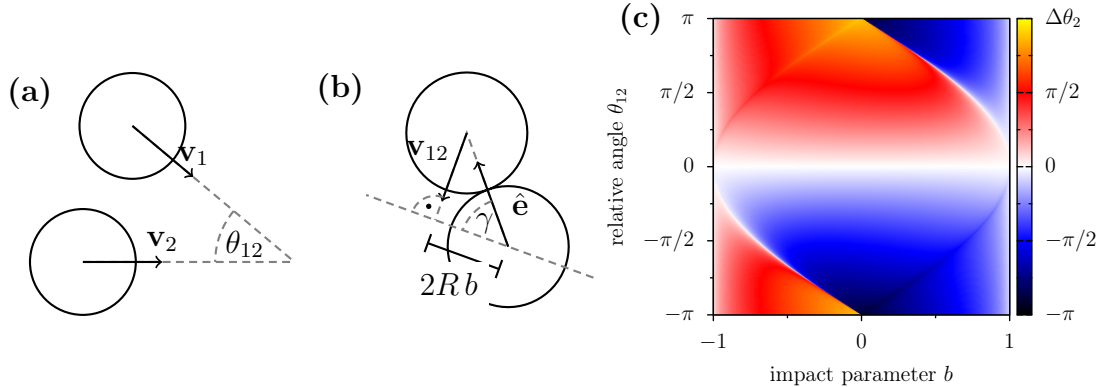


Figure 2.27: Illustration of the collision geometry defined by the impact parameter b and the relative angle θ_{12} . **(a)** Particles 1 and 2 are moving with their respective velocities \mathbf{v}_1 and \mathbf{v}_2 , enclosing the relative angle $\theta_{12} = \angle(\mathbf{v}_1, \mathbf{v}_2)$. **(b)** Definition of relative velocity \mathbf{v}_{12} , unit vector $\hat{\mathbf{e}}$, and impact parameter b . The unit vector $\hat{\mathbf{e}}$ is defined as the normalized vector connecting the particle centers at the very moment of contact, and $2Rb$ gives the offset from a head-on collision. **(c)** Change in the direction of motion of particle 2, $\Delta\theta_2$ (scattering angle), as a function of the collision geometry (θ_{12}, b). Since both particles are identical spheres, the scattering behavior of the particle 1 can be read off at the point $(-\theta_{12}, b)$ in the plot. Parameters: $\mu = 0.01$, $\kappa = 10^{-1}$, corresponding to maximal average alignment (for proof see **publication B.8**).

determine the phase boundary, we typically computed 10 realizations of different initial coordinates and velocity directions for a set of values of the single particle noise σ_0 and the packing fraction $\Phi = \frac{N\pi d^2}{4L_{\text{box}}^2}$. Running the simulations for sufficiently long times, we classify a point in Φ - σ_0 -parameter space to be macroscopically *polarized* if the system's polarization $\psi = N^{-1} \sum_{i=1}^N \hat{\mathbf{v}}_i$ [with $\hat{\mathbf{v}}_i = \mathbf{v}_i / |\mathbf{v}_i|$] exceeds a value of $\psi > 0.6$ for at least one realization. Otherwise, the parameter set is classified as *isotropic*. The resulting phase diagram is depicted in Fig. 2.28(a): Red dots indicate the values of the control parameters (Φ, σ_0) where a transition to a *polar* state is observed, while gray squares correspond to *isotropic* states.

(iii) In the last step of our “renormalized” approach, by means of kinetic theory we aim to determine the phase boundary based on the results of the scattering study [Fig. 2.27(c)], which we are going to compare to the phase boundary obtained from the multi-particle MD simulations [see Fig. 2.28(a)]. This comparison allows us to scrutinize *quantitatively* the validity of kinetic theory since the collision rule is devoid of any approximation. The collision rule required to set up the Boltzmann equation maps the pre-collision orientations given by the angles θ_1 and θ_2 on the post-collision orientations, denoted θ'_1 and θ'_2 . Denoting the angular change for particle $j \in \{1, 2\}$ by $\eta_j(\theta_{12})$, the collision rule has the following

general form:³⁷

$$(\theta_1, \theta_2) \rightarrow (\theta_1 + \eta_1(\theta_{12}), \theta_2 + \eta_2(\theta_{12})). \quad (2.25)$$

Since the above collision rule required for the Boltzmann equation does not resolve length scales comparable to the size of single particles, the impact parameter b must be reduced from the mapping given in Fig. 2.27(c). In a collision with given relative pre-collisional angle θ_{12} , a scattering angle $\eta_j(\theta_{12})$ occurs with probability $p_j(\eta_j|\theta_{12})d\eta_j$ where

$$p_j(\eta_j|\theta_{12}) = \frac{1}{2} \int_{-1}^{+1} db \delta(\Delta\theta_j(b, \theta_{12}) - \eta_j). \quad (2.26)$$

Since $p_j(\eta_j|\theta_{12})$ is computed from $\Delta\theta_j(b, \theta_{12})$ [see Fig. 2.27(c)] by integrating over the impact parameter b , we have now transitioned from a deterministic description to a probabilistic treatment of the collision process. For a detailed discussion of $p_j(\eta_j|\theta_{12})$, the interested reader is referred to **publication B.8**.

To implement $p_j(\eta_j|\theta_{12})$ into the Boltzmann equation (2.8), it suffices to modify the gain part of the collision integral Eq. (2.8e):

$$\mathcal{C}^+[f^{(2)}] = \int_{-\pi}^{\pi} d\theta_1 \int_{-\pi}^{\pi} d\theta_2 \Gamma(\theta_1, \theta_2) f^{(2)}(\mathbf{r}, \theta_1, \theta_2, t) \frac{1}{2} \sum_{j=1}^2 \int_{-\infty}^{\infty} d\eta_j p_j(\eta_j|\theta_{12}) \bar{\delta}(\theta_j + \eta_j - \theta). \quad (2.27)$$

In the modified *gain* contribution $\mathcal{C}^+[f^{(2)}]$, each of the the two terms ($j = 1, 2$) accounts for the scattering of one of the particles in a binary collision using the respective distribution $p_1(\eta_1|\theta_{12})$ or $p_2(\eta_2|\theta_{12})$ [Eq. (2.26)] corresponding to particle 1 or 2. The factor 1/2 is required to avoid counting collisions twice. Note that in the collision process above the interaction noise $\sigma = 0$ [see Eq. (2.8e)], and $\eta_j(\theta_{12})$ is fully determined by the numerical results of the scattering study. Therefore, in the following, the control parameters are the single particle noise characterized by σ_0 and the homogeneous packing, *i.e.* $\Phi = \rho_0 \pi d^2 / 4$ where ρ_0 is the homogenous hydrodynamic particle density and d denotes the particle diameter.

To make contact with the Φ - σ_0 -phase diagram from multi-particle simulations, we calculate the *critical single particle noise* by the condition $\nu(\Phi, \sigma_0) = 0$. Note that ν is defined in Eq. (2.10) [details on the derivation of ν can be found in **publication B.8**]. Interestingly, by assuming that the initial states at the onset of collective motion are devoid of angular correlations, *i.e.* the *assumption of molecular chaos* is fulfilled [Eq. (2.8a)], we find that $\nu < 0$ for all control parameters Φ and σ_0 . This would imply that the system's isotropic state remains stable for arbitrary values of the control parameters, which is obviously at odds with the phase diagram obtained from multi-particle simulations [Fig. 2.28(a)]. This clearly indicates that the state of the system preceding a transition to a polarized state cannot be free of correlations, casting doubt on the validity of the molecular chaos assumption Eq. (2.8a). In contrast, in a monatomic gas, elastic collisions on average prohibit a build-up of inter-particle correlations over time, thereby supporting the validity of the *molecular*

³⁷Instead of the half angle alignment rule, Eq. (2.8g), *i.e.* $(\theta_1, \theta_2) \rightarrow (\theta_1 + \frac{1}{2}(\theta_2 - \theta_1), \theta_2 + \frac{1}{2}(\theta_1 - \theta_2))$, we determine η_j from the binary scattering studies.

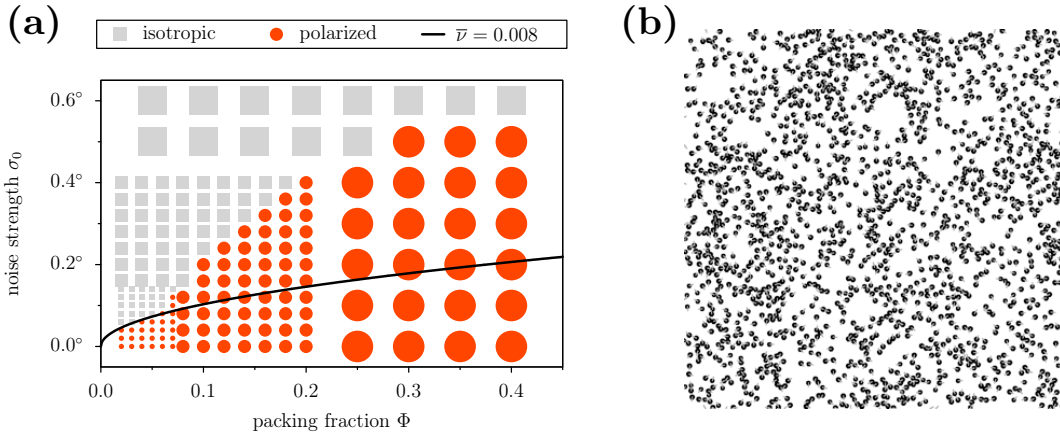


Figure 2.28: **(a)** *Phase diagram* as function of packing fraction Φ and angular noise σ_0 [degrees]: Results obtained from multi-particle simulations are displayed by symbols, while lines correspond to analytical predictions for the phase boundary. *Multi-particle simulation*: Red dots indicate polarized states while gray squares correspond to control parameter sets where no change in the initial isotropic state has been observed. *Analytical results*: The solid line depicts the phase boundary obtained from kinetic theory incorporating the function χ as obtained from numerical measurements. The phase boundary shows an excellent agreement with the numerical multi-particle phase diagram at low packing fractions $\Phi < 0.08$. **(b)** *Snapshot of a state with pre-cursor angular correlations*: Only a small section of the entire simulation system is shown. The state is approximately homogeneous, but the distribution of relative orientations clearly deviates from a typical molecular chaos state [see **publication B.8** for the numerical results on $\chi(\theta)$].

chaos assumption. However, our actively propelled constituents give rise to highly dissipative collisions resulting in orientational correlations. To account for these orientational correlations, we introduce the function $\chi(\theta_{12})$, leading to the following modified “closure relation” for the two-particle density:

$$f^{(2)}(\mathbf{r}, \theta_1, \theta_2, t) = \chi(\theta_{12})f(\mathbf{r}, \theta_1, t)f(\mathbf{r}, \theta_2, t). \quad (2.28)$$

Measuring $\chi(\theta_{12})$ in the multi-particle MD simulations we find, slightly below the ordering transition, pronounced deviations from $\chi(\theta_{12}) = 1$, indicating the existence of angular correlations³⁸ [see Fig. 2.28(b) for a snapshot]. Due to the appearance close to the ordering transition we refer to these correlations as *pre-cursor* correlations. Most importantly, these angular correlations are strong enough to trigger a sign-change in the kinetic coefficient ν , thereby allowing kinetic theory to predict an ordering transition. Moreover, the predicted phase boundary perfectly matches the one obtained from the multi-particle simulations in the regime of small packing fractions [see Fig. 2.28(a)]. However, for intermediate packing

³⁸A detailed presentation and discussion of the dependence of $\chi(\theta_{12})$ can be found in **publication B.8**.

fraction $0.1 < \Phi < 0.4$, kinetic theory underestimates the systems's ordering capability. One reason for this discrepancy could be the omission of spatial correlations. Otherwise, analyzing videos of the ordering process (see attached video material) indicates that at these packing fractions an intricate clustering process triggers the ensuing coarsening dynamics. An appropriate description of clustering involves multi-particle collisions, which requires (within the framework of a single particle description³⁹) accounting for higher-order correlations by means of $f^{(3)}, f^{(4)} \dots$

In summary, we generalized kinetic theory for propelled particles moving with constant speed [15, 16] as detailed in section 2.3.2 regarding the two following aspects: The collision rule is quantitatively determined by the results of the microscopic scattering study, and Eq. (2.28) accounts for angular correlations among the active particles, where the deviation to the molecular chaos $\chi(\theta_{12})$ is explicitly measured in the multi-particle MD simulations. Our “renormalized” kinetic theory seems to be flexible enough to accommodate the complex behavior of soft active colloids, *e.g.* the occurrence of *pre-cursor* angular correlations. We are convinced that our approach is also perfectly suited to reconcile microscopic experimental studies of propelled particle systems [90, 93, 30], in which *pre-cursor* correlations are likely to exist, and their corresponding quantitative mesoscopic descriptions. This could pave the way to understanding the patterning process leading to the rich manifold of experimentally observed patterns.

³⁹An alternative way to describe the clustering process is by introducing a further species, and is detailed in section 2.3.5.

2.4 Propelled Particle Systems at High Densities

This section is devoted to the generic phenomena occurring in propelled particle systems at large packing fractions. Whereas under dilute conditions, denser regions act as “vacuum cleaners”, collecting more and more particles and aligning those parallel to the horde, the picture for the emergence of collective motion under highly packed conditions is expected to be distinctively different:

- Particles’ excluded volume gives rise to strong repulsive interactions leading to anti-correlations in the velocity. As long as ferromagnetic alignment interactions only affect⁴⁰ the particles’ velocities, as in Vicsek-like models (refer to section 1.2 for details, or [105]), repulsive interactions impair the local build-up of coherently moving units, especially at large packing fractions.
- At highly dense packings, particles are forced to arrange in spatial configurations reminiscent of solids in classical statistical mechanics. Here, in the case of a propelled particle system, the fundamental question is [69, 49, 68, 57, 48]: *Which degree of spatial order (short-range, quasi-long range or true long-range) can develop in the presence of ferromagnetic alignment interactions?*
- Additionally, for packing fractions close to the maximum,⁴¹ transport of displacements (phonons) by repulsive interactions is expected to be fast relative to the local ferromagnetic alignment interactions. This separation of time-scales could lead to *intermittency in the order parameters*, *i.e.* on-going fluctuations in time and space without any relaxation in a stationary state. Fluctuations in the order parameters, *e.g.* of the net polarization, correspond to collisions (in particular compression and shear) of largely extended coherently moving regions. These encounters create strong compressions at their contact zones potentially giving rise to *shock-waves* propagating with a speed much larger than the individual particle velocities.

In order to analyze and understand the phenomena occurring in propelled particle systems at large packing fractions, we will propose an agent-based model in section 2.4.1, which can be regarded as the Vicsek-model [105] extended by repulsion [41, 40]. In section 2.4.2 we will discuss the numerical results of this model, including a classification of the ensuing states. In particular, we characterize the degree of orientational and transitional order of all observed states at large packing fractions.

2.4.1 Agent-based Model

To study active soft matter at high densities, we consider an off-lattice system of N particles that have a tendency to align their velocity with neighboring particles and repel each other if they come too close. These interactions are implemented by the following parallel update

⁴⁰A counterexample is the vibrated disk assay, which is detailed in section 2.2.

⁴¹In two dimensions, the maximal packing fraction is ~ 0.91 .

rules for the velocity $\mathbf{v}_i(t)$ and position $\mathbf{x}_i(t)$ of each particle i with some discrete time interval⁴² Δt :

$$\mathbf{v}_i(t + \Delta t) = v_a \frac{\sum_{j \in \mathcal{A}_i} \mathbf{n}_j(t)}{|\sum_{j \in \mathcal{A}_i} \mathbf{n}_j(t)|} + v_r \sum'_{j \in \mathcal{A}_i} \frac{\mathbf{x}_{ij}(t)}{|\mathbf{x}_{ij}(t)|}, \quad (2.29)$$

$$\mathbf{x}_i(t + \Delta t) = \mathbf{x}_i(t) + \mathbf{v}_i(t + \Delta t) \Delta t. \quad (2.30)$$

Here $\mathbf{n}_i := \mathbf{v}_i/|\mathbf{v}_i|$ denotes the particle director, and $\mathbf{x}_{ij} := \mathbf{x}_i - \mathbf{x}_j$ signifies the relative distance vector between particles i and j . The first term in Eq. (2.29) is an alignment interaction as introduced by Vicsek et al. [105] where the updated velocity of particle i is given by the average velocity of all particles within a spherical area \mathcal{A}_i of radius $2R$ centered on particle i . The parameter v_a characterizes the strength of alignment as well as the particles' propelling speed. The second term in Eq. (2.29) describes a soft, and pairwise additive repulsive interaction between a given particle i and all its neighbors within the same area⁴³ \mathcal{A}_i . It displaces a particle pair, whose distance $|\mathbf{x}_{ij}(t)| \leq 2R$, radially outward by a constant amount $v_r \Delta t$. In the following, we will refer to R as the particle radius. Length and time are measured in units of the particle diameter, $D = 2R$, and the corresponding time to traverse this distance, $\tau = 2R/v_a$, respectively.

We are mainly interested in the collective dynamics as a function of the packing fraction $\rho = N \pi R^2 / L_{\text{box}}^2$ [L_{box} : linear side length of simulation box], and the relative strength of the repulsive and alignment interaction, $\nu := v_r/v_a$. Noting that $v_a \Delta t$ sets the maximal penetration depth in binary collisions, we choose the other parameters such that $v_a \Delta t \ll 2R$ in order to reduce the number of events where particles would pass through each other. Specifically, the updating time is fixed to $\Delta t = 1$ and we choose $v_a = 0.05$. All simulations, if not stated otherwise, were performed in a periodic square box of side-length $L_{\text{box}} = 100$, *i.e.* the simulation typically comprised $N \sim 10^4$ particles.

2.4.2 Results for Propelled Particles at Large Densities

First, we analyze the degree of polar and bond orientational (hexatic) order. The global polarization is defined as $\mathcal{P}(t) = |\langle \mathbf{n}_i(t) \rangle_i|$, where $\langle \dots \rangle_i$ denotes an average over all particles in the system. Local hexatic order is characterized by $\Psi_{6,l} = |\mathcal{N}_l|^{-1} \sum_{m \in \mathcal{N}_l} e^{i6\theta_{lm}}$, where the summation extends over the \mathcal{N}_l topological (Voronoi) nearest neighbors of particle l , and θ_{lm} is the angle of the bond between particles l and m relative to some arbitrary axis. The absolute value of $\Psi_{6,l}$ characterizes the degree of local hexatic order and its direction gives the hexatic cell's orientation.

Figs. 2.29(a) and 2.29(b) illustrates the degree of polar and hexatic order as a function of the packing fraction and the relative strength of repulsive and alignment interaction.

⁴²Note that our model is discrete, thereby Δt is a model parameter, characterizing the time between two successive updates of the alignment and repulsive interaction, see Refs. [105, 29, 22, 40, 23, 11].

⁴³The model is easily generalized to account for different radii for alignment and repulsion, R_a and R_r , respectively. Here, we focus on the competition between alignment and repulsion, hence we choose $2R_r = R_a$. Previous studies of the Vicsek model with repulsion were restricted to the limit $R_r \ll R_a$ [22, 74].

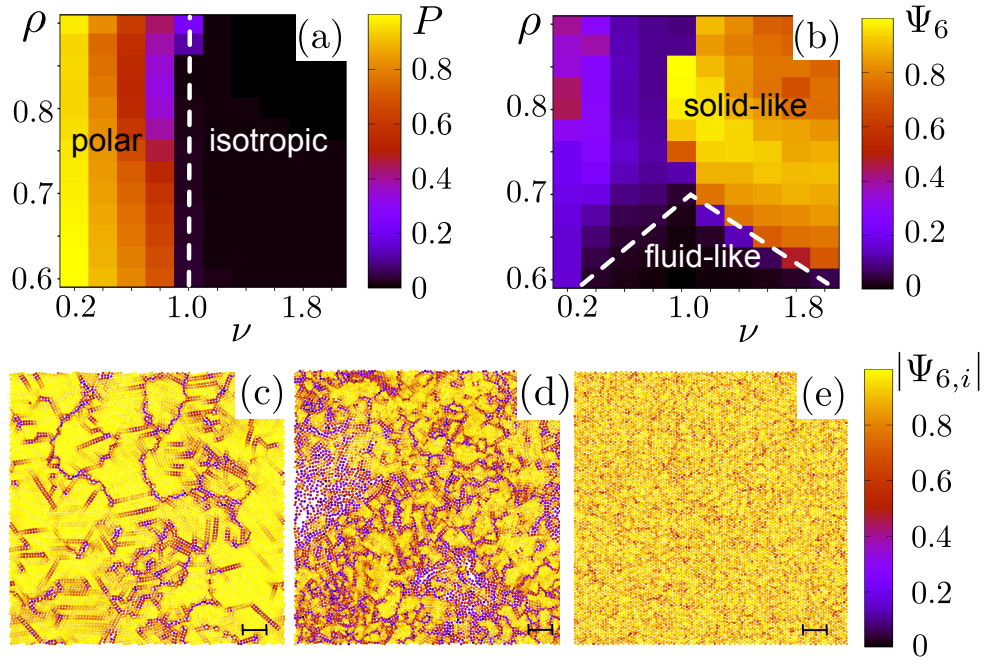


Figure 2.29: *Global polar order* parameter P (a) and *hexatic order* parameter Ψ_6 (b) as a function of ρ and ν . The dashed white lines indicate tentative boundaries between *polar* and *isotropic* states, and *solid-like* states exhibiting hexatic order from *fluid-like* states, respectively. Snapshots of *local hexatic order* Ψ_6 for $\nu = 0.25$ (c), $\nu = 0.75$ (d), and $\nu = 1.5$ (e) at a high packing fraction $\rho = 0.85$. See also videos attached to this thesis (for a Video description please refer to **publication B.9**). Scale bars indicate a distance of $10D$.

We observe that global polar order, characterized by the time-averaged polarization $P = \langle \mathcal{P}(t) \rangle_t$, is well-established for $\nu \lesssim 1$, but then at $\nu \approx 1$ sharply drops to very small values [Fig. 2.29(a)]. The phase boundary between *polar* and *isotropic* states, tentatively defined by $P = 0.2$, is nearly independent of the packing fraction ρ . To discern the different degrees of bond-orientational or translational order is more difficult. As can be inferred from Fig. 2.29(b), the degree of hexatic order grows with increasing packing fraction ρ , indicating a *solid-like* regime; the dashed white line in Fig. 2.29(b) correspond to a value of $\Psi_6 = |\langle \langle \Psi_{6,i} \rangle_i \rangle_t| = 0.2$.

To characterize the degree of order at high densities it is necessary to go beyond the global hexatic order parameter Ψ_6 and have a closer look at the number as well as the spatial organization and dynamics of topological defects. To this end we analyzed appropriate quantities⁴⁴ leading to the following central results, illustrated in Fig. 2.30 (for details on the study, the interested reader is referred to **publication B.9**):

⁴⁴In particular, we considered the correlation functions [73, 72], $C(r) = \frac{1}{\sum_i |\Psi_i|^2} \sum_{|\mathbf{x}_i - \mathbf{x}_j| = r} \Psi_i \Psi_j^*$, for both the hexatic (bond orientational), $\Psi_i = \Psi_{6,i}$, and the translational, $\Psi_m = \Psi_{\mathbf{G},m} = \exp(-i \mathbf{G} \cdot \mathbf{r}_m)$, order parameter [\mathbf{G} : one of the three lattice vectors].

In the *fluid-like* regime the correlation functions characterizing the degree of translational and (bond) orientational order decay exponentially, indicating that the ensuing order is *short-ranged* [Fig. 2.30, red boundaries]. However, in the *solid-like* regime we find two distinct regions in the ν - ρ -parameter space [Fig. 2.30, green boundaries]:

- (1) [$\nu > 1$]: An *active crystal* with long-range bond orientational and translational order; regarding the polarization, the state is isotropic [Fig. 2.30, blue boundaries]. Topological defects⁴⁵ vanish out of the system by ring-like contraction and pair-annihilation [see attached Videos].
- (2) [$\nu < 1$]: A *polycrystalline active solid* that coherently flows into a certain direction (*i.e.* there is a broken-symmetry axis) with long-range polar order [Fig. 2.30, blue boundaries]. Moreover, these states are characterized by hexagonal patches of different relative bond orientations, implying exponentially decaying correlations of the bond orientational order parameter. However, correlations of translational order decay as a power-law (quasi-long range), indicating the crystalline nature of these states. Additionally, the region in parameter space for the *polycrystalline active solid* can be tentatively divided according to their fluctuations (in all order parameters and the number of defects):
 - (A) [$0.375 \lesssim \nu < 1$] Order (polar and spatial order) in these states exhibits strong fluctuations in time, *i.e.* the degree of polar order (and spatial order) suddenly drops to a finite, but non-zero value (say around 0.2), while ordered regimes show *e.g.* a polarization of about 0.8; hence, we termed this regime *intermittent* [Fig. 2.30, dashed boundaries]. This behavior leads to a bimodal probability distribution for the number of topological defects. Moreover, the drop-down of order is typically accompanied by *shock-waves*. For an illustration the reader is referred to the video material.
 - (B) [$\nu \lesssim 0.375$] Order in these states fluctuates only little in time compared to (A). The fluctuations occur concomitantly with weak rotations of the broken-symmetry axis. The probability distribution of the number of defects is found to be of Gaussian shape.

Even though our numerical studies discovered and characterized a plethora of new and unknown states within the field of propelled particle systems, many questions remain unanswered:

- (i) Is the “list” of states and phenomena already complete, and how can these states be verified experimentally? Moreover, if we extend our model by a simple growth process, does it lead to a transition to a glass state⁴⁶ in time, as found recently in dense cell sheets [4]?
- (ii) At packing fractions close to the maximal packing, fast non-linear modes analogous to

⁴⁵Particles having not six Voronoi neighbors (computed via CGAL library version 4.8).

⁴⁶Hallmarks of the glass transition are the occurrence of dynamical heterogeneities (pronounced diversity in migration velocities) and a sub-diffusive mean-square displacement.

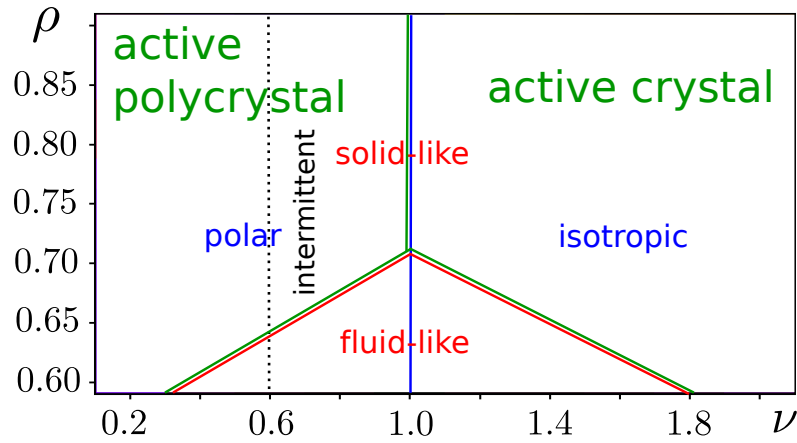


Figure 2.30: Summary of the characteristic states in the ν - ρ control parameter space for propelled particles with “ferromagnetic alignment” in the regime of large packing fractions.

phonons in an equilibrium crystal occur, which we roughly termed *shock-waves*. What is the dispersion-relation of these non-linear modes, and what sets their propagation speed? Moreover, how are they related to the system’s ordering capability?

(iii) What are the essential ingredients for a corresponding analytic (continuous) description characterizing these modes?

Appendix A

List of Publications

2010:

- (1) Volker Schaller, Christoph A. Weber, Christine Semmrich, Erwin Frey, Andreas R. Bausch, *Polar patterns of driven filaments*, **Nature** 467, 7377 (2010).

2011:

- (2) Volker Schaller, Christoph A. Weber, Erwin Frey, Andreas Bausch, *Polar Pattern Formation: Hydrodynamic coupling of driven filaments*, **Soft Matter** 7 (7), 3213 - 3218 (2011).
- (3) B. Meier, A. Zielinski, C.A. Weber, D. Arcizet, S. Youssef, T. Franosch, J. O. Rädler, D. Heinrich, *Chemical cell trapping in controlled alternating gradient fields*, **Proceedings of the National Academy of Sciences** 108, 11417-11422 (2011).
- (4) Volker Schaller, Christoph A. Weber, Benjamin Hammerich, Erwin Frey, Andreas R. Bausch, *Frozen steady states in active systems*, **Proceedings of the National Academy of Sciences** 108, 19183-19188 (2011).

2012:

- (5) Christoph A. Weber, Volker Schaller, Andreas R. Bausch, Erwin Frey, *Nucleation-induced transition to collective motion in active systems*, **Phys. Rev. E** 86, 030901(R) (2012).

2013:

- (6) Christoph A. Weber, Florian Thüroff, Erwin Frey, *Role of particle conservation in self-propelled particle systems*, **New Journal of Physics** 15, 045014 (2013).

- (7) Christoph A. Weber, Timo Hanke, Julien Deseigne, Sébastien Léonard, Olivier Dauchot, Erwin Frey, Hugue Chaté, *Long-range Ordering of Vibrated Polar Disks*, **Phys. Rev. Let.** 110, 208001 (2013).
- (8) Florian Thüroff, Christoph A. Weber, Erwin Frey. *A Critical Assessment of the Boltzmann Approach for Active Systems*, **Phys. Rev. Let.** 111, 19061 (2013).
- (9) Timo Hanke, Christoph A. Weber, Erwin Frey. *Understanding Collective Dynamics of Soft Active Colloids by Binary Scattering*, **Phys. Rev. E** 88, 052309 (2013).

Submitted for publication:

- (10) Christoph A. Weber, Christopher Bock, Erwin Frey. *Defect-Mediated Transition in Active Soft Matter*, submitted for publication.

In preparation:

- (11) Christoph A. Weber, Ryo Suzuki, Volker Schaller, Andreas R. Bausch, Igor S. Aranson and Erwin Frey. *Origin of Non-thermal Anomalous Events in Active Filaments*, in preparation.
- (12) Simon Weber, Christoph A. Weber, Erwin Frey. *Phase Separation of Two Species with different Activity*, in preparation.
- (13) Florian Thüroff, Christoph A. Weber, Erwin Frey. *Solving Numerically Active Kinetic Equations*, in preparation.

Appendix B

Selected Publications

B.1 Polar Patterns of Driven Filament

title	<i>Polar patterns of driven filaments</i>
authors	Volker Schaller, Christoph A. Weber , Christine Semmrich, Erwin Frey, Andreas R. Bausch
status	published
journal	Nature, Vol. 467, 09312, 2010.
supplement	yes, attached
published video material	http://www.nature.com/nature/journal/v467/n7311/full/nature09312.html

Summary

The emergence of collective motion exhibited by systems ranging from flocks of animals to self-propelled microorganisms to the cytoskeleton is a ubiquitous and fascinating self-organization phenomenon. Similarities between these systems, such as the inherent polarity of the constituents, a density-dependent transition to ordered phases or the existence of very large density fluctuations, suggest universal principles underlying pattern formation.

To increase the understanding underlying the self-organization in active systems we consider an experimental system consisting of actin filaments that move on a carpet of molecular myosin motors. We find that, at sufficiently high filament densities, persistent collective motion emerges: The filaments self-organize into moving clusters, rotating vortices or collectively moving wave-patterns.

Our experimental approach, which offers control of relevant system parameters such as filament density, is complemented by agent-based simulations, which allow backtracking of the assembly and disassembly pathways to the underlying local interactions. We identify weak and *local* alignment interactions to be essential for the observed formation of patterns and their dynamics. The presented minimal polar-pattern-forming system may thus provide new insights into emergent phenomena in other propelled particle systems.

B.2 Polar Pattern Formation: Hydrodynamic Coupling of Driven Filaments

title	<i>Polar pattern formation: hydrodynamic coupling of driven filaments</i>
authors	Volker Schaller, Christoph A. Weber , Erwin Frey, Andreas R. Bausch
status	published
journal	Soft Matter, 7, 3213, 2011.
supplement	yes, attached
published video material	http://pubs.rsc.org/ en/Content/ArticleLanding/2011/SM/c0sm01063d

Summary

In our recent studies of the motility assay at high filament densities we showed that local alignment interactions trigger the emergence of coherently moving patterns (see B.1). However, in the later stages of the patterning process, we found indications that hydrodynamic interactions play a crucial role for the systems dynamics.

Therefore, in this project we investigated the role of hydrodynamic interactions in the actin gliding assay at high filament densities. We find that the approximately two-dimensional collectively moving structures induce a back-flow in the overlying fluid. By means of appropriate shear flow experiments we were able to proof that this back-flow is strong enough to influence the movement of nearby coherently moving structures. Moreover, these long ranged hydrodynamic interactions play a crucial role in the pattern forming mechanisms: Stability and size of the patterns is set by the fluid-mediated interaction. Finally, studying the role of confining boundaries we found that a swarming cluster effectively feels a repelling force without being in direct contact that points away from the boundary. This force also originates from hydrodynamic interactions between cluster and boundary, again mediated by the solvent above the coherently moving structure.

B.3 Frozen Steady States in Active Systems

title	<i>Frozen steady states in active systems</i>
authors	Volker Schaller, Christoph A. Weber , Benjamin Hammerich, Erwin Frey, Andreas R. Bausch
status	published
journal	PNAS, Vol. 108, No, 48, 2011.
supplement	yes, attached
published video material	http://www.pnas.org/content/suppl/2011/11/10/1107540108.DCSupplemental

Summary

In this project we study the actin motility assay at large densities in the presence of cross-linking molecules. Surprisingly, we find an absorbing state with frozen fluctuations that at first sight seems to be impossible for active matter driven by the incessant input of energy. While such states were reported for externally driven systems through macroscopic shear or agitation, the investigation of frozen active states in inherently active systems like cytoskeletal suspensions or active gels were still at large. By means of the high-density gliding assay experiments, we demonstrate that frozen steady states can arise in active systems if active transport is coupled to growth processes.

Specifically, we show that the interplay of only three components, actin filaments, HMM motor proteins, and fascin crosslinkers is sufficient for the emergence of a frozen active steady state that consists of highly symmetric structures, rings, and elongated filament bundles that are actively assembled and propelled by the motor proteins. We complement our approach by agent-based simulations allowing us to correlate the formation of a frozen steady state with the mechanical properties of the emergent structures. We identify the crosslinkers as the central determinant mediating the emergence of frozen active steady states: Crosslinkers support the growth to larger filament bundles and thereby freeze the structures configurations.

B.4 Nucleation-induced Transition to Collective Motion in Active Systems

title	<i>Nucleation-induced transition to collective motion in active systems</i>
authors	Christoph A. Weber , Volker Schaller, Andreas R. Bausch, Erwin Frey
status	published
journal	Phys. Rev. E 86, 030901(R), 2012.
supplement	yes, attached
published video material	http://pre.aps.org/supplemental/PRE/v86/i3/e030901

Summary

Motivated by our recent findings of collective patterns in the actin motility assay at large filament densities (see B.1), we analyzed a numerical model able to capture the main features of the filament-filament interactions. Many other models for self-propelled particles systems have been analyzed numerically, mainly focusing on the long-time dynamics, *e.g.* the emergence of a broken symmetry state, or concentrated on the analysis of the ensuing stationary pattern. However, the time-dependent assembly processes leading to collective motion so far remained elusive.

To close this gap, we used a simple agent-based model for (self-)propelled particles, which interact via an effective excluded volume interaction and a local polar alignment field, to analyze the dynamics of the pattern forming processes *in time*. As already found for other models for aligning (self-)propelled particles systems, also our model shows a phase transition to collective motion above a critical density. Interestingly, we find that the onset of collective motion is accompanied by a gain in free volume over time. Close to the critical density, the onset of collective motion is shown to require the spontaneous formation of a cluster of sufficiently large mass that acts as a nucleus and triggers the transition to collective motion. The corresponding lag-time shows a power-law divergence upon approaching the critical density.

The fact that the ordering process is driven by the formation of a critical nucleation cluster hopefully motivates to consider the time dependent characteristics of a broader class of active systems.

B.5 Role of Particle Conservation in Self-propelled Particle Systems

title	<i>Role of particle conservation in self-propelled particle systems</i>
authors	Christoph A. Weber , Florian Thüroff, Erwin Frey
status	published
journal	New Journal of Physics, 15(945014), 2013.
supplement	no

Summary

The emergence of collective motion in driven or self-propelled particle systems is a fascinating field of recent interdisciplinary interest. Actively propelled particles undergoing dissipative collisions are known to develop a state of spatially distributed coherently moving clusters. For densities larger than a critical value clusters grow in time and form a stationary well-ordered state of coherent macroscopic motion. Many analytical approaches for self-propelled particles systems have been proposed, mainly focussing on particle conserving systems. The impact of a particle reservoirs on the system's patterning properties remains largely elusive.

To close this gap we suggest and analyze a simple two-species kinetic model. Led by observations of localized coherently moving clusters pervading these systems in the vicinity of the ordering transition, we use these two species to depict some of the interaction properties between freely moving particles and particles integrated in clusters. Specifically, we account for coalescence of clusters from single particles, assembly of single particles on existing clusters, collisions between clusters, and cluster disassembly. By means of our model we then address two questions:

1. What is the role of the particles' aspect ratio in the context of cluster formation, and does the particle shape affect the system's behavior on hydrodynamic scales?
2. To what extent does particle conservation influence pattern formation?

Coarse-graining our kinetic model, (1) we demonstrate that particle shape (*i.e.* aspect ratio) slightly shifts the scale of the transition density, but does not impact pattern formation properties. (2) We show that the validity of particle conservation determines the existence of a longitudinal instability, which tend to amplify density heterogeneities locally in turn triggering a wave pattern with wave vectors parallel to the axis of macroscopic order. If the system is in contact with a particle reservoir the ensuing instability vanishes again, which can be traced back to a compensation of the ensuing density heterogeneities.

B.6 Long-range Ordering of Vibrated Polar Disks

title	<i>Long-range Ordering of Vibrated Polar Disks</i>
authors	Christoph A. Weber , Timo Hanke, Julien Deseigne, Sébastien Léonard, Olivier Dauchot, Erwin Frey, Hugues Chaté
journal	Phys. Rev. Let. 110, 208001 (2013)
supplement	yes, attached

Summary

The emergence of collective motion in driven or self-propelled particle systems is a fascinating field of recent interdisciplinary interest. Many models for self-propelled particles systems have been analyzed numerically or analytically, usually lacking a quantitative connection to a concrete experimental system. To close this gap, we propose a simple particle-based model for propelled particles, in order to describe the dynamics of granular disks vibrated by a shaking apparatus.

Vibrated polar disks have been used experimentally to investigate collective motion of driven particles, and allow for a detailed characterization of the particles dynamics. Specifically, by means of direct comparison with experimental data, we show that our model reproduces *quantitatively* the single, binary and collective properties of this system. The *quantitative* agreement with the experimental system allows us to use the model to study the systems dynamics at system sizes, which are not accessible in the laboratory. Therefore we can answer the question: “Can vibrated disks really order?”. Moreover, we explore the models parameter space and find a phase diagram qualitatively different from that of dilute or point-like particle systems. In particular, our findings might reopen the debate about the possibility of a continuous transition to collective motion, since the structures “responsible” for its discontinuous character—the bands—cannot not be found for packing fractions above some critical value.

B.7 A Critical Assessment of the Boltzmann Approach for Active Systems

title	<i>A Critical Assessment of the Boltzmann Approach for Active Systems</i>
authors	Florian Thüroff, Christoph A. Weber , Erwin Frey
journal	Phys. Rev. Let. 111, 190601 (2013)
supplement	yes, attached

Summary

Here we study a generalized Boltzmann equation to assess the polar ordering transition in systems of self-propelled rods, based on an explicit microscopic picture of particle interactions, and critically examine its range of applicability to experimentally relevant active systems. In recent studies on active matter, the Boltzmann equation has been used by several authors to describe spontaneous symmetry breaking and to study the emergence of spatial patterns. All these approaches are based on a simplified picture of particle interactions, which, in essence, translates Vicsek’s alignment rule for agent based simulations to the case of binary particle collisions. These studies are able to reproduce a number of phenomena previously observed in agent based simulations, including the formation of polar order and traveling wave solutions. However, to which extent a Boltzmann approach is appropriate to capture the characteristic features of active systems when based on the actual physics of particle interactions, remains an open question.

In this contribution, we present for the first time a Boltzmann description of the macroscopic polar ordering process in active systems, which is fully based on a microscopic picture of binary particle interactions. To make contact with the characteristics of the microscopic collision processes, we present binary scattering studies for rigid and for semiflexible, self-propelled rods in two-dimensions moving in an over-damped environment. Based on a thorough analysis of these scattering studies, we then set up a generalized kinetic description of such systems, which explicitly keeps track of the essential features of binary collisions in the form of “scattering functions”. To assess the ordering processes predicted by these kinetic equations, we use both, a standard analytical procedure to derive the macroscopic equations of motion, and a full numerical solution of the underlying Boltzmann equation itself. We find that the Vicsek-like alignment rule is qualitatively consistent with the pattern formation properties of general weakly aligning systems, but systematically underestimates the transition scales toward the formation of polar order. In particular, we demonstrate that in the presence of collision noise, kinetic theory predicts a complete breakdown of order formation below a noise-dependent, non-zero angular interaction range, even in the case of optimal Vicsek-like alignment.

B.8 Understanding Collective Dynamics of Soft Active Colloids by Binary Scattering

title	<i>Understanding Collective Dynamics of Soft Active Colloids by Binary Scattering</i>
authors	Timo Hanke, Christoph A. Weber , Erwin Frey
journal	Phys. Rev. E. 88, 052309 (2013)
supplement	yes, attached (video description)

Summary

Many models for self-propelled particles systems have been analyzed numerically or analytically, usually relying on the assumption that *binary* interactions between the constituents contribute the major part to their alignment capabilities. In the following letter we addressed the question, whether the collective dynamics in propelled particle systems can be understood by solely considering *binary* interactions between the constituents, by a combination of molecular dynamics (MD) simulations and kinetic theory. Specifically, we considered a system of active spherical particles interacting by a short-ranged and repulsive harmonic force. In the absence of interactions, these soft particles move at constant speed determined by a balance between a driving and a dissipative force. From MD simulations for this system of soft active colloids we determined the phase boundary between the isotropic and the polarized state. To connect these numerical studies with a kinetic approach, we employed the MD simulations to also analyze binary scattering of particles. Thereby one could extract the underlying collision-rule, *i.e.* the mapping of the pre-collision to the post-collision velocities, which served as a starting point to set up a Boltzmann equation for the one-particle distribution function. The microscopic origin of the collision rule offered the opportunity to quantitatively scrutinize the predictions of kinetic theory for propelled particle systems through direct comparison with multi-particle simulations. Thereby we identified local pre-cursor correlations at the onset of collective motion to constitute the essential determinant for a qualitative and quantitative validity of kinetic theory. In particular, only if the kinetic description included these correlations, the analytic prediction of the phase boundary coincided quantitatively for small packing fractions with the one from multi-particle simulations. Most importantly, if orientational correlations were neglected, kinetic theory for propelled particles failed, *i.e.* it predicted that ordering is absent, which is at odds with corresponding molecular dynamics simulations.

B.9 Defect-Mediated Transition in Active Soft Matter

title	<i>Defect-Mediated Transition in Active Soft Matter</i>
authors	Christoph A. Weber , Christopher Bock, Erwin Frey
status	submitted for publication
supplement	yes, attached

Summary

Since activity and active transport processes play a crucial role in all biological system, many theoretical models have been developed to unravel the fundamental ingredients for the emergence of the developing patterns and phenomena. A subclass of active systems are propelled particle systems. Famous members of this class are gliding bacteria, driven cytoskeletal filaments or shaken granules. In general, propelled particle systems can give rise to collective motion patterns reminiscent to flocks of birds or schools of fish. To investigate the physical properties of these systems the numerical analysis of particle-based models turned out as one of the major tools. The most famous particle-based model within the field of propelled particle systems has been proposed by Vicsek et al. [Vicsek, Phys. Rev. Let., 1995]. It is essentially equal to a XY-model for propelled particle system and rests on the competition between parallel alignment and some noise. This model lead to an intense growth of the field with a large number of contributions from scientist of various field of physics: granular media, biological physics and critical phenomena & kinetic theory. However, most of these studies so far considered solely *dilute* systems.

In our manuscript we study a particle-based model in the spirit of the one proposed by Vicsek et al., but focus on the regime of large densities close the maximal packing fraction in two dimensions and analyze the competition between parallel alignment and particles' excluded volume. We find a number of unknown states and phenomena: In particular, we discover the emergence of two new *active crystalline* phases with distinctively different properties compared to the states at dilute particle densities. For dominating alignment strength the stationary state is polarized (long-range ordered), but fluctuations cause an intermittency (reminiscent to shock-waves) in the order parameter leading to the creation of topological defects. Interestingly, the number of defects in the system remain approximately constant and are arranged in interconnected grain boundaries. For dominating excluded volume we find an active crystal: In contrast to thermal systems, the fluctuations of the propelled particle system preserve—unlike thermal fluctuations—long-range translational order without creating topological defects.

Defect-Mediated Phase Transitions in Active Soft Matter

Christoph A. Weber, Christopher Bock, and Erwin Frey
*Arnold Sommerfeld Center for Theoretical Physics and Center for NanoScience,
 Department of Physics, Ludwig-Maximilians-Universität München,
 Theresienstraße 37, D-80333 Munich, Germany*

How do topological defects affect the degree of order in active matter? To answer this question we investigate an agent-based model of self-propelled particles, which accounts for polar alignment and short-ranged repulsive interactions. For strong alignment forces we find collectively moving polycrystalline states with fluctuating networks of grain boundaries. In the regime where repulsive forces dominate, the fluctuations generated by the active system give rise to quasi-long-range transitional order, but—unlike thermal system—without creating topological defects.

PACS numbers: 64.70.D-, 61.72.Lk, 05.70.Ln, 64.60.Cn

For a system in thermodynamic equilibrium, phases with a broken continuous symmetry in two spatial dimensions are prohibited by general theorems [1, 2]. Yet, for two-dimensional solids, XY magnets, and superfluids there is a clear qualitative difference between a low-temperature phase exhibiting quasi-long-range order and a high-temperature phase where correlation functions decay exponentially [3]. Since for crystalline solids the low- and high-temperature phases are separated by two broken symmetries, namely translational and orientational symmetry, melting can proceed by two steps, mediated by the unbinding of dislocations [4–7] or disclinations [6, 7], respectively. With its two successive continuous phase transitions with an intervening hexatic phase it provides an alternative melting scenario to a discontinuous first-order transition [8, 9].

These statements may no longer remain valid for systems driven out of thermodynamic equilibrium. Indeed, for active systems where individual particles are self-propelled, an antagonism between dissipative processes favoring “ferromagnetic” alignment of the particles’ velocities and noise can trigger a phase transition from an isotropic to a long-range ordered polar state, where particles move collectively. This was first demonstrated by Vicsek et al. [10] who employed a two-dimensional agent-based model where particle alignment is implemented as an update rule: Each particle aligns parallel to the average of all particles’ orientations within some defined finite neighborhood. Interestingly, computer simulations of the Vicsek model show that the transition is discontinuous, and the polar state exhibits propagating wave-like excitations [11, 12]. The basic mechanism for the phase transition is believed to constitute a low-density phenomenon. In the corresponding kinetic description the formation of order is driven by a gradual reduction in the spread of particle orientations by means of weakly aligning binary collisions [13–15]. Experimental investigations supporting this picture are motility assays where cytoskeletal filaments are propelled by some lawn of molecular motors [16–19], and vibrated granular systems [20, 21].

In contrast, much less is known about ordered states

of active matter at *high densities*, where in addition to *polar order* the active system may also exhibit different degrees of *liquid crystalline* [23] or even *crystalline order*. Numerical studies of models for (self-)propelled particles discovered jammed [24], and also crystalline-like states at large packing fractions [11, 25]. Recently, a mean-field theory combining elements from phase-field models of crystals [26] and hydrodynamic theories of active systems [27–29] was proposed and shown to exhibit a wealth of crystalline states of different symmetry and degrees of polar order [30]. Although all these theoretical studies suggest the interesting possibility of the emergence of translational and orientational order in active particle systems, a characterization of the nature of these ordered states and the transition between them remains elusive. In this context, one might suppose that topological defects will play an important role. Indeed, recent

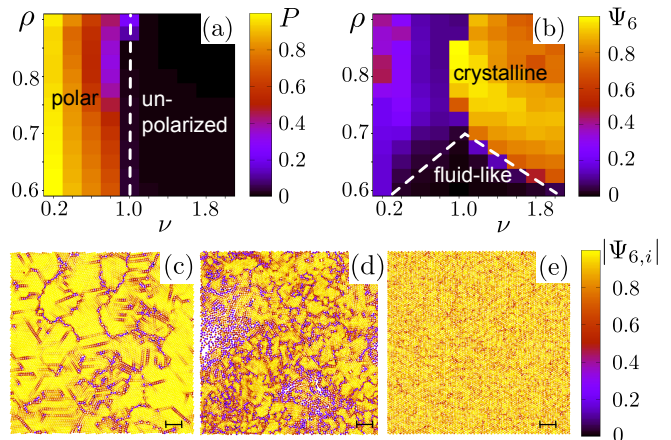


FIG. 1. Global polar order parameter P (a) and hexatic order parameter Ψ_6 (b) as a function of ρ and ν . The dashed white lines indicate tentative boundaries between *polar* and *unpolarized* states, and *crystalline* states exhibiting hexatic order from *fluid-like* states. Snapshots of local hexatic order $|\Psi_{6,i}|$ for $\nu = 0.25$ (c), $\nu = 0.75$ (d), and $\nu = 1.5$ (e) at a high packing fraction $\rho = 0.85$. See also videos in the Supplemental Material [22]. Scale bars indicate a distance of $20R$.

experimental and theoretical studies of active liquid crystals [23, 31] show that activity leads to generation and swarming of topological defects. Active dislocations have also been shown to drive growth of bacterial cell walls through dislocation climb [32].

In this study we investigate the role of topological defects for the nature of ordered states in active matter at high densities. To this end, we build on a generalized Vicsek model introduced by Grégoire and Chaté [11, 33], which accounts for Vicsek-like alignment interactions as well as short-ranged repulsive interactions. Depending on the relative strength of these interactions we find different degrees of crystalline and polar order. In the regime where repulsion is dominant, we observe no polar order, *i.e.* no collective motion of the particles. Interestingly, however, the fluctuations generated by the active system lead to an intriguing state of matter exhibiting quasi-long-range translational order but – unlike systems in thermal equilibrium – devoid of any topological defects. In contrast, in the regime where dissipative alignment dominates we find collectively moving polycrystalline states with hexagonally ordered crystalline domains of characteristic size. These states exhibit pronounced defect fluctuations and sound-wave-like excitations.

To study active soft matter at high densities, we consider an off-lattice system of N particles which have a tendency to align their velocity with neighboring particles and repel each other if they come too close [11, 33]. These interactions are implemented by the following parallel update rules for the velocity $\vec{v}_i(t)$ and position $\vec{x}_i(t)$ of each particle i with some discrete time interval Δt :

$$\vec{v}_i(t + \Delta t) = v_a \frac{\sum_{j \in \mathcal{A}_i} \vec{n}_j(t)}{|\sum_{j \in \mathcal{A}_i} \vec{n}_j(t)|} + v_r \sum'_{j \in \mathcal{A}_i} \frac{\vec{x}_{ij}(t)}{|\vec{x}_{ij}(t)|}, \quad (1)$$

$$\vec{x}_i(t + \Delta t) = \vec{x}_i(t) + \vec{v}_i(t + \Delta t) \Delta t. \quad (2)$$

Here $\vec{n}_i := \vec{v}_i/|\vec{v}_i|$ denotes the particle director, and $\vec{x}_{ij} := \vec{x}_i - \vec{x}_j$ signifies the relative position vector between particles i and j . The first term in Eq. (1) is an alignment interaction as introduced by Vicsek et al. [10] where the updated velocity of particle i is given by the average velocity of all particles within a circular area \mathcal{A}_i of radius $2R$ centered on particle i . The parameter v_a characterizes the strength of alignment as well as the particles' propulsion speed. The second term in Eq. (1) describes a soft, pairwise additive repulsive interaction between a given particle i and all its neighbors within the same area \mathcal{A}_i . It displaces a particle pair, whose separation $|\vec{x}_{ij}(t)| \leq 2R$ [$i \neq j$, indicated by the primed sum], radially outward by a constant amount $v_r \Delta t$. In the following, we will refer to R as the particle radius. Length and time are measured in units of the particle diameter, $2R$, and the corresponding time to traverse this distance, $\tau = 2R/v_a$, respectively. The model can easily be generalized to account for different radii for alignment

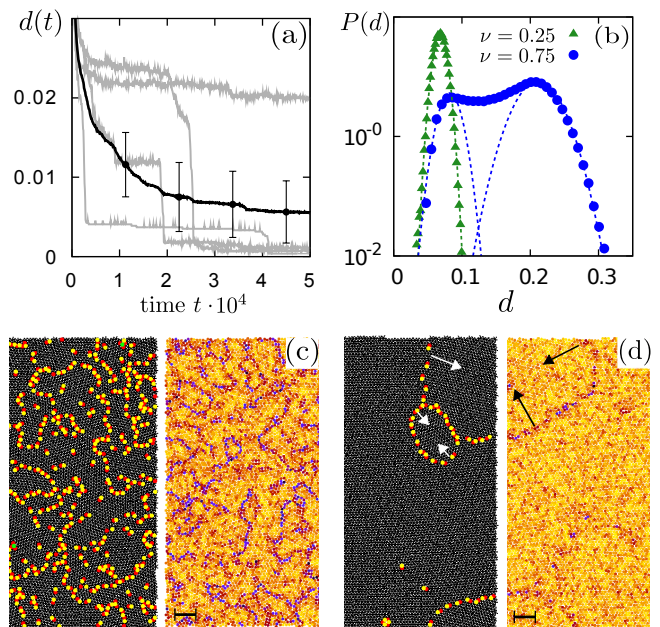


FIG. 2. **(a)** Defect ratio d as a function of time t for $(\rho, \nu) = (0.85, 1.5)$. The black curve is an average over 50 realizations (grey lines) with error bars indicating the standard deviation. **(b)** Probability distribution $P(d)$ [lin(d)-log] of the defect ratio for $(\rho, \nu) = (0.85, 0.25)$ (green, triangles), and $(\rho, \nu) = (0.85, 0.75)$ (blue, circles). **(c, d)** Snapshots illustrating the defect dynamics for $(\rho, \nu) = (0.85, 1.5)$ where the system shows a high degree of crystalline order: **(c)** Early phase with roughly homogeneous distributed defects and small hexagonal patches; **(d)** Formation of ring-like dislocation lines at larger times that contract (indicated by black arrows). The left and right half of each figure depict the Voronoi triangulation and the hexatic order parameter, respectively. Particles with 5/7-fold coordination are indicated by red/yellow dots, and green dots corresponds to particles with more than 7-fold or less than 5-fold coordination. The scale bars correspond to 10 particle diameters ($20R$).

and repulsion, R_a and R_r , respectively. Here, we focus on the competition between alignment and repulsion, and therefore have chosen the two radii as $2R_r = R_a$; previous studies of the Vicsek model with repulsion were restricted to the limit $R_r \ll R_a$ [34, 35]. We are mainly interested in the collective dynamics as a function of the packing fraction $\rho = N \pi R^2 / L^2$, and the relative strength of the repulsive and alignment interaction $\nu := v_r / v_a$.

First, we analyze the degree of polar and bond-orientational order. The global polarization is defined as a system average $\langle \dots \rangle_i$ of all the particles' orientations $\vec{n}_i(t)$: $\mathcal{P}(t) = |\langle \vec{n}_i(t) \rangle_i|$. Local bond-orientational order is characterized by the hexatic order parameter $\Psi_{6,i} = |\mathcal{N}_i|^{-1} \sum_{j \in \mathcal{N}_i} e^{i6\theta_{ij}}$, where the summation extends over all \mathcal{N}_i topological (Voronoi) nearest neighbors of particle i , and θ_{ij} is the “bond”-angle between particles i and j relative to an arbitrarily chosen reference axis.

Figures 1(a,b) illustrate the degree of polar and hexatic order as a function of the packing fraction ρ , and the relative strength of repulsive and alignment interactions ν . We observe that global polar order, characterized by the time-averaged polarization $P = \langle \mathcal{P}(t) \rangle_t$ [$\langle \dots \rangle_t$: time-average], is well-established for weak repulsion $\nu \lesssim 1$, but at $\nu \approx 1$ sharply drops to very small values [Fig. 1(a)]. The respective phase boundary between *polar* and *unpolarized* states is tentatively defined by $P = 0.2$. Note that it is nearly independent of the packing fraction ρ , indicating that the transition from a polar collectively moving state to an unpolarized state is mainly driven by an antagonism between repulsive and alignment forces but not the particle density. To discern the different degrees of bond-orientational or translational order is more difficult. As can be inferred from Fig. 1(b), there are different degrees of global hexatic order, $\Psi_6 = \langle |\langle \Psi_{6,i} \rangle_i| \rangle_t$, with a maximum for large packing fraction ρ and strong repulsive interaction (large ν); the dashed white line in Fig. 1(b) correspond to a value of $\Psi_6 = 0.2$. Strikingly, the loss of polar order is concomitant with the emergence of a high degree of crystalline order, and vice versa.

While the global polar and hexatic order parameters provide a first rough estimate of the degree and nature of the ordered states, a full characterization thereof requires an in-depth analysis of the spatio-temporal dynamics. In particular, as for thermodynamic equilibrium systems, the dynamics and the spatial organization of topological defects are especially important indicators of crystalline order. Figs. 1(c-e) depict snapshots of the local hexatic order $|\Psi_{6,i}|$ at a large packing fraction of $\rho = 0.85$ for a set of values for ν . Depending on the relative strength of repulsive and alignment interaction marked differences in the spatial organization of defects are clearly visible. While for $\nu \lesssim 0.25$ dislocations align to form a network of rather well-defined grain boundaries, they tend to cluster in the intermediate regime $0.375 \lesssim \nu \lesssim 1.0$ [Figs. 1(c,d)]. For $\nu \gtrsim 1.0$, concomitant with the loss of polar order, the defects become more evenly spread and slowly disappear from the system; see Fig. 1(e) for a snapshot, and Fig. 2(a) for the dynamics of the defect density. This reassures the observation made on the basis of the order parameters, namely that polar and crystalline order are mutually exclusive.

There are even more dramatic differences in the spatio-temporal dynamics of the defects; see the videos in the Supplemental Material [22]. For $\nu \lesssim 0.375$, we observe a *flowing polycrystalline state* where changes in the flow direction strongly affect the network of grain boundaries. In the stationary regime, the defect fraction $d = D/N$ is Gaussian-distributed around a mean of about 7% [Fig. 2(b)]; here D is the number of all particles with a coordination different from 6-fold. In the intermediate regime, we find *intermittent dynamics* where episodes of polycrystalline and polar order alternate with episodes of disorder which are accompanied by

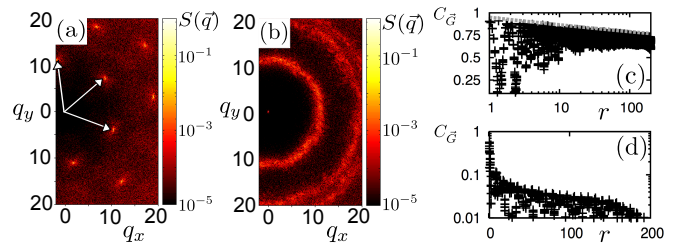


FIG. 3. *Static structure factor* $S(\vec{q})$ for $(\rho, \nu) = (0.85, 1.5)$ (a) and $(\rho, \nu) = (0.85, 0.25)$ (b), respectively, both in the stationary regime. Reciprocal lattice vectors \vec{G} are indicated by white arrows. *Correlation function* $C_{\vec{G}}(r)$ for $(\rho, \nu) = (0.85, 1.5)$ (c) [$\log(r)$ -lin, dashed line is a power law with exponent 0.04] and $(\rho, \nu) = (0.85, 0.25)$ (d). Results correspond to a simulation box of size $L = 400$ containing $N = 172156$ particles; see Supplemental Material [22] S5 for the corresponding pair correlation functions and details on the data evaluation.

sound waves (see Supplemental Material [22], S1, S4). This dynamics is reflected in a bimodal shape of the defect probability density $P(d)$ [Fig. 2(b)]: While the peak at low values of d corresponds to particle configurations with a high degree of polar order, the peak at higher values originates from time intervals where the collective motion breaks down and strong density inhomogeneities arise.

Dynamics and spatial organization of topological defects change qualitatively for strong repulsive interaction, $\nu \gtrsim 1$, where polar order is also absent. Starting from an initial disordered state [Fig. 2(c)], we observe that first the spatial distribution of defects coarsens quickly and then organizes into dislocation lines [Fig. 2(d)]. Subsequently these defect lines contract and self-annihilate, leaving the system in a state with evenly spread *isolated* and *paired dislocations*; see also videos in the Supplemental Material [22]. The annihilation processes of these dislocations are seen as periods of steep decline in the time traces for the defect fraction [Fig. 2(a), grey curves]. After each steep decline, the decrease in defect number slows down significantly due to an enlarged inter-defect distance. We observe that the number of isolated defects decreases extremely slowly; see the asymptotic decline in the average defect fraction in Fig. 2(a). Moreover, we find evidence that the topological defects even move sub-diffusively (see Supplemental Material [22], S3). Taken together, it is numerically not feasible to study the asymptotic dynamics significantly beyond what is shown in Fig. 2(a). To check whether a defect-free crystal is stable we initialized the system in an unpolarized and perfectly hexagonal ordered state, and waited until the global hexatic order parameter $\Psi_6(t)$ converged to a stationary value. Even though the active dynamics leads to a reduction of the hexatic order parameter to a stationary value of $\Psi_6 \approx 0.9$, it is not

strong enough to create any defects for densities larger than $\rho \approx 0.8$. Hence, we conclude that the stationary states for $\nu \gtrsim 1$ and large density ($\rho \gtrsim 0.8$) are indeed *free of topological defects*. When decreasing the packing fraction below 0.8, there is a small range of packing fractions where fluctuations trigger the creation of defects (see Supplemental Material [22], S2). However, in the ensuing non-equilibrium steady state dislocations are always found in pairs, indicating that the corresponding states exhibit quasi-long-range order; exploring parameter space we could not identify hexatic phases with isolated dislocations. Further decreasing the packing fraction, the defect ratio $d(\rho)$ increases to a rather high value $d \sim 0.4$, signaling a transition to a fluid-like phase.

In order to further scrutinize the nature of order within the crystalline regime we computed the pair correlation function $g(\vec{r})$, the corresponding static structure factor $S(\vec{q})$, and the correlation functions [3, 22]

$$C_\alpha(r) = \frac{1}{\sum_i |\Psi_{\alpha,i}|^2} \sum_{|\vec{x}_i - \vec{x}_j| = r} \Psi_{\alpha,i} \Psi_{\alpha,j}^* \quad (3)$$

for the hexatic $\Psi_{6,i}$, and the translational $\Psi_{\vec{G},i} = e^{-i\vec{G}\vec{r}_i}$ order parameter with \vec{G} denoting a reciprocal lattice vector. As discussed above, for $\nu > 1$, dislocation pairs decay extremely slowly and, as a consequence, the asymptotic non-equilibrium steady state can not be reached within a computationally accessible time. Therefore, to obtain steady state results for the correlation functions, we initialized the system in a hexagonal and isotropic configuration ($\Psi_6 = 1$, $P \approx 0$); the corresponding results for simulations starting from an disordered initial state are discussed in the Supplemental Material [22]. We find that both $S(\vec{q})$ [Figs. 3(a) and 3(b)] and $g(\vec{r})$ [see Supplemental Material S5] exhibit a sharp and discrete pattern of hexagonal symmetry, clearly indicating a high degree of translational order. This is confirmed by $C_6(r)$ being constant over the whole system size [Fig. 4(a)], and the slow decay of the translational correlation function $C_{\vec{G}}(r)$. The decay follows a power-law with a very small exponent of about 0.04 [see Fig. 3(c), dashed grey line], which is difficult to discern from a logarithmic decay. Taken together, these results lead us to conclude that this state of active matter is an *active crystal*, free of topological defects with long-range bond-orientational order and quasi-long-range translational order. In contrast, in the parameter regime of *polycrystalline* order, the static structure factor shows the ring-like features of a liquid [Figs. 3(b)]; see also Supplemental Material [22] S5. These features are due to the different orientations of the hexagonally ordered patches, as also evident from the exponential decay in C_6 [Fig. 4(a)] and the fast decay of $C_{\vec{G}}(r)$ [Figs. 3(d)].

To further quantify the nature of the polycrystalline state we compare the global hexatic order parameter, $\Psi_6 = \langle |\langle \Psi_{6,i} \rangle_i| \rangle_t$, with an order parameter characteriz-

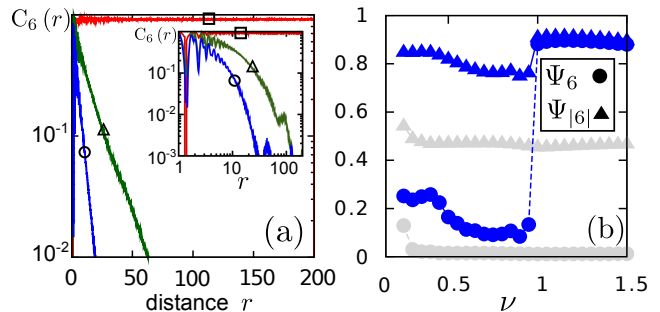


FIG. 4. (a) Correlation function $C_6(r)$ in $\ln(r)$ -log (inset: log-log) for the same parameters as in Figs. 1c-d: $\rho = 0.85$, and $\nu = 1.5$ (red, square), $\nu = 0.75$ (blue, circle), and $\nu = 0.25$ (green, triangle). Correlations were computed in a box of size $L = 400$ including $N = 172156$ particles. (b) Local and global hexatic order parameter, $\Psi_{|6|}$ and Ψ_6 , as a function of ν for different values of ρ [$\rho = 0.85$ (blue/black); $\rho = 0.6$ (light grey)].

ing local hexatic order, $\Psi_{|6|} := \langle \langle |\Psi_{6,i}| \rangle_i \rangle_t$. For polycrystalline solids, one expects Ψ_6 to be small since the complex numbers $\Psi_{6,i}$ of particles from different ordered patches cancel in the average $\langle \dots \rangle_i$. In contrast, using the absolute values $|\Psi_{6,i}|$ there is no such cancellation of phases. Therefore, the value of $\Psi_{|6|}$ should be close to 1 in a polycrystalline phase because most particles have six-fold coordination and are not located at grain boundaries. Figure 4(b) depicts both order parameters as a function of ν for two different densities, with the lower value corresponding to the *fluid-like* and the larger one to the *crystalline* regime. In the *fluid-like* regime, local bond orientational order, $\Psi_{|6|}$, is moderately developed while global orientational order, Ψ_6 , is close to zero. Moreover, both order parameters are only weakly dependent on ν . This is in stark contrast to the behavior at higher densities, $\rho = 0.85$. There Ψ_6 shows a steep and large decrease at $\nu \approx 1$, while $\Psi_{|6|}$ remains approximately constant, indicating that we have a polycrystalline phase for $\nu \lesssim 1$. Since the active crystal phase ($\nu \gtrsim 1$) exhibits quasi-long-range order, local and global hexatic order are likewise well developed.

Topological defects are the hallmark of phase transitions in two-dimensional crystalline systems. For systems in thermodynamic equilibrium they drive the successive breaking of translational and bond-orientational order. Our investigations of active crystalline matter at high density have revealed: While defects still play a decisive role, the emerging defect dynamics and phase behavior differ qualitatively from their equilibrium analogues. In active systems, the non-equilibrium steady states include different types of polycrystalline phases, and a crystalline phase with quasi-long-range translational order but completely devoid of any topological defects. Our theoretical findings can readily be tested by experimental model systems [22].

We would like to thank David Nelson for fruitful and stimulating discussions. This project was supported by the Deutsche Forschungsgemeinschaft in the framework of the SFB 863, and the German Excellence Initiative via the program “NanoSystems Initiative Munich” (NIM).

-
- [1] N. D. Mermin and H. Wagner, *Phys. Rev. Lett.* **17**, 1133 (1966).
- [2] P. Hohenberg, *Physical Review* **158**, 383 (1967).
- [3] D. R. Nelson, *Defects and Geometry in Condensed Matter Physics* (Cambridge University Press, Cambridge, 2002), p. 392.
- [4] J. M. Kosterlitz and D. J. Thouless, *Journal of Physics C: Solid State Physics* **6**, 1181 (1973).
- [5] A. P. Young, *Phys. Rev. B* **19**, 1855 (1979).
- [6] B. I. Halperin and D. R. Nelson, *Phys. Rev. Lett.* **41**, 121 (1978).
- [7] D. R. Nelson and B. I. Halperin, *Phys. Rev. B* **19**, 2457 (1979).
- [8] L. Landau, *Phys. Z. Sowjetunion* **11**, 26 (1937).
- [9] S. Alexander and J. McTague, *Phys. Rev. Lett.* **41**, 702 (1978).
- [10] T. Vicsek *et al.*, *Phys. Rev. Lett.* **75**, 1226 (1995).
- [11] G. Grégoire and H. Chaté, *Phys. Rev. Lett.* **92**, 025702 (2004).
- [12] H. Chaté, F. Ginelli, G. Grégoire, and F. Raynaud, *Phys. Rev. E* **77**, 046113 (2008).
- [13] E. Bertin, M. Droz, and G. Grégoire, *Phys. Rev. E* **74**, 022101 (2006).
- [14] E. Bertin, M. Droz, and G. Grégoire, *Journal of Physics A: Mathematical and Theoretical* **42**, 445001 (2009).
- [15] F. Thüroff, C. A. Weber, and E. Frey, submitted for publication .
- [16] T. Butt *et al.*, *Journal of Biological Chemistry* **285**, 4964 (2010).
- [17] V. Schaller *et al.*, *Nature* **467**, 73 (2010).
- [18] V. Schaller, C. Weber, E. Frey, and A. R. Bausch, *Soft Matter* **7**, 3213 (2011).
- [19] Y. Sumino *et al.*, *Nature* **483**, 448 (2012).
- [20] J. Deseigne, O. Dauchot, and H. Chaté, *Phys. Rev. Lett.* **105**, 098001 (2010).
- [21] C. A. Weber *et al.*, *Phys. Rev. Lett.* **110**, 208001 (2013).
- [22] See Supplemental Material for videos and more information at <http://...> .
- [23] T. Sanchez *et al.*, *Nature* **491**, 431 (2012).
- [24] J. Henkes, Y. Fily, and M. C. Marchetti, *Phys. Rev. E* **84**, 040301 (2011).
- [25] J. Bialké, T. Speck, and H. Löwen, *Phys. Rev. Lett.* **108**, 168301 (2012).
- [26] K. R. Elder, M. Katakowski, M. Haataja, and M. Grant, *Phys. Rev. Lett.* **88**, 245701 (2002).
- [27] J. Toner and Y. Tu, *Phys. Rev. Lett.* **75**, 4326 (1995).
- [28] J. Toner and Y. Tu, *Phys. Rev. E* **58**, 4828 (1998).
- [29] J. Toner, *Phys. Rev. E* **86**, 031918 (2012).
- [30] A. M. Menzel and H. Löwen, *Phys. Rev. Lett.* **110**, 055702 (2013).
- [31] L. Giomi, M. J. Bowick, X. Ma, and M. C. Marchetti, *Phys. Rev. Lett.* **110**, 228101 (2013).
- [32] A. Amir and D. R. Nelson, *Proceedings of the National Academy of Sciences* **109**, 9833 (2012).
- [33] G. Grégoire, H. Chaté, and Y. Tu, *Physica D: Nonlinear Phenomena* **181**, 157 (2003).
- [34] H. Chaté *et al.*, *The European Physical Journal B - Condensed Matter and Complex Systems* **64**, 451 (2008).
- [35] L. Peng *et al.*, *Phys. Rev. E* **79**, 026113 (2009).

Supplemental Material:

Defect-Mediated Phase Transitions in Active Soft Matter

Christoph A. Weber, Christopher Bock, and Erwin Frey
Arnold Sommerfeld Center for Theoretical Physics and Center for NanoScience,
Department of Physics, Ludwig-Maximilians-Universität München,
Theresienstraße 37, D-80333 Munich, Germany

All simulations of the agent-based model were, if not stated otherwise, performed in a square box of side-length $L = 100$ [unit length: particle Diameter $2R$] with periodic boundary conditions and typically containing $N \sim 10^4$ particles. Noting that $v_a \Delta t$ sets the maximal penetration depth in binary collisions, we choose the other parameters such that $v_a \Delta t \ll 2R$ in order to reduce the number of events where particles would pass through each other. Specifically, the updating time is fixed to $\Delta t = 1$, and we take $v_a = 0.05$.

Initialization at high densities

In general, we initialized the numerical simulations of the agent based model in two different configurations, which we termed:

(\mathcal{R}) *Random*. Particle initial positions and orientations were chosen randomly. Since this leads to strong overlaps of the particle interaction radii R , we let the system first evolve in time with repulsive interactions only, until most of the overlaps vanished and the defect ratio has reached a value of $d = 0.2$. Then, both propulsion and alignment interaction were switched on, and data were recorded.

(\mathcal{H}) *Hexagonal*. Particle orientations were chosen randomly, while their positions were placed in a perfect hexagonal configuration with a hexagonal lattice spacing of $2R$. This implies a global hexatic order parameter $\Psi_6 = 1$ and the absence of defects, *i.e.* $d = 0$, at the time when simulations were started.

Triangulation

We used standard 2D Voronoi Triangulation functions as implemented by the *CGAL* library [<http://www.cgal.org>].

Fourier transformation and structure factor

In Fig. 3 we computed the pair correlation function $g(\mathbf{r}) = (L/N)^2 \sum_{i,j} \delta(\mathbf{r} - (\mathbf{r}_i - \mathbf{r}_j))$, and the corresponding static structure factor $S(\mathbf{q}) = 1 + \frac{N}{L^2} \int d\mathbf{r}^2 g(\mathbf{r}) e^{i\mathbf{q}\cdot\mathbf{r}}$. We numerically determined $S(\mathbf{q})$ by using standard fast Fourier transform (FFT) libraries with a spatial resolution of 0.1 unit length.

Correlation function of the translational order parameter

Since global (bond) orientational is not perfect for $\nu > 1$ (*e.g.* for $\rho = 0.85$ we have $\Psi_6 \approx 0.9$), the inverse lattice vector \mathbf{G} must be determined properly. We varied the corresponding angle of the inverse lattice vector \mathbf{G} with a step size of $5 \cdot 10^{-4}$ rad, and thereby determined the optimal value of \mathbf{G} with the weakest decay of $C_{\mathbf{G}}$; the ensuing results are depicted in Fig. 3(c,d,g,h), and Fig.S5 and Fig.S6 in the Supplementary Material. Note that a non-optimal choice of the lattice angle leads—even for a perfectly hexagonal configuration—to an underestimation of translational order[1].

Experimental realization at high density

Active matter at high density may be realized experimentally using emulsion droplets containing extensile microtubule bundles [2]. They have been shown to exhibit spontaneous motility when in frictional contact with a hard

surface; depending on the availability of ATP their motion can be tuned from passive Brownian motion to active persistent random walks. We envisage that large assemblies of such active soft droplets are ideal model systems to test our theoretical predictions. Though the detailed mechanisms of the interaction between the droplets is different from the interaction rules of the agent-based model, we expect that the main features of the dynamics and phase behavior to be generic for active matter at high densities. Another promising experimental system are active colloidal particles. Recent studies of photo-activated colloidal particles [3] and carbon-coated Janus particles [4] show various types of pattern and cluster formation. The versatility of colloidal systems should also allow the design of experiments to explore the dynamics of active matter at high density at high density.

Video descriptions

For all attached videos we chose the following parameter values: Interaction radii $R = 0.5$, updating time $dt = 1.0$, alignment strength $v_a = 0.05$, and system size $L = 100$.

The videos depict the *Voronoi triangulation* of the particles (left) and the *local hexatic order parameter* $|\Psi_{6,i}|$ (right). Voronoi triangulation: Particles with a coordination different from 6-fold are illustrated by color: red= 5 neighbors, yellow= 7 neighbors, green is equal to more than 7 or less than 5 neighbors.

Local hexatic order parameter: 1 = yellow, 0 = black, with the color code shown in Fig. 1 (main text).

Parameters for density ρ and ν are indicated in the file names. Each video corresponds to an initialization with different *random* particle coordinates and orientations (\mathcal{R}).

ADDITIONAL MATERIAL

In this section we provide additional graphs substantiating certain statements made in the main text.

-
- [1] C.-C. Liu *et al.*, Journal of Polymer Science Part B: Polymer Physics **48**, 2589 (2010).
 - [2] T. Sanchez *et al.*, Nature **491**, 431 (2012).
 - [3] J. Palacci *et al.*, Science **339**, 936 (2013).
 - [4] I. Buttinoni *et al.*, Phys. Rev. Lett. **110**, 238301 (2013).
 - [5] H. Chaté, F. Ginelli, G. Grégoire, and F. Raynaud, Phys. Rev. E **77**, 046113 (2008).
 - [6] E. R. Weeks and D. A. Weitz, Phys. Rev. Lett. **89**, 095704 (2002).

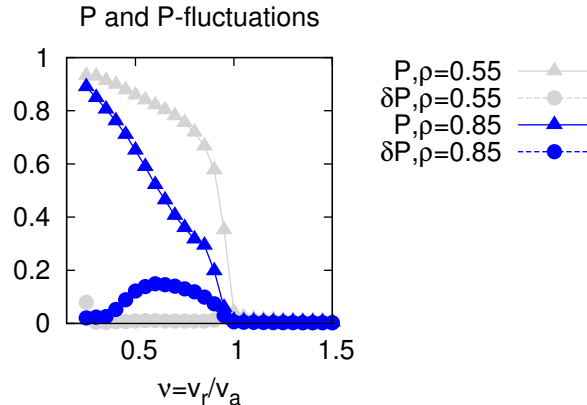


FIG. S1: *Intermittent states*: In order to find the ν -parameter regime for the *intermittent states*, we analyzed the total polarity P and the fluctuations in time of $\mathcal{P}(t)$, denoted as δP . Both quantities are depicted as a function of ν for a *fluid-like* density $\rho = 0.55$ and a *crystalline* density $\rho = 0.85$ [refer to Fig. 1, main text]. Pronounced fluctuations in polarity $\mathcal{P}(t)$ exist for $0.375 \lesssim \nu \lesssim 1.0$ (i.e. $\delta P > 0.08$), indicating the *intermittent* regime. Moreover, our results indicate that the unpolarized–polarized transition with a *fluid-like* density $\rho = 0.55$ is very steep, reminiscent of the *discontinuous* phase transition found in the Vicsek model without repulsion [5]. In contrast, the existence of the intermittent states at large densities (e.g. $\rho = 0.85$) flattens the slope of the total polarity in the transitional region between the *crystalline* regime ($\nu > 1$) and the polarized non-intermittent regime ($\nu \lesssim 0.375$).

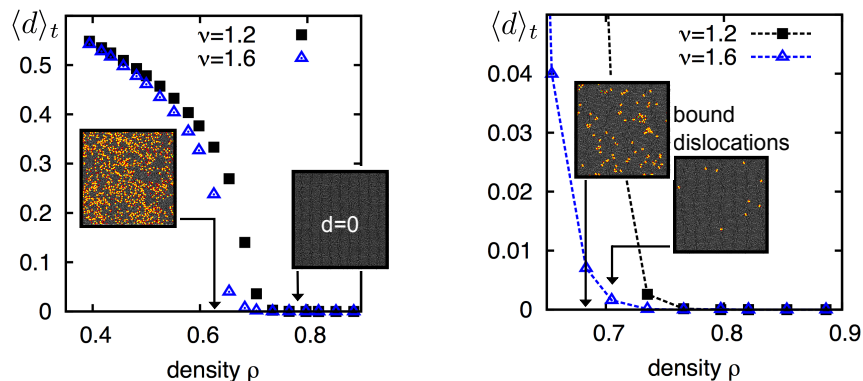


FIG. S2: *Averaged defect ratio* $\langle d \rangle_t$ for $\nu = \{1.2, 1.6\}$ as a function of density ρ (left and right solely differ in a different plot range for the density). The system is initialized in an unpolarized and fully ordered hexagonal configuration (\mathcal{H}). The *fluid-like* phase is characterized by a rather large defect ratio $\langle d \rangle_t \sim 0.4$. Increasing the density, we observe a small density region (e.g. around $\rho \approx 0.7$ for $\nu = 1.6$), where *active* fluctuations are strong enough to create a non-zero defect ratio. However, the defect ratio is rather small, i.e. $\langle d \rangle_t \sim 0.005$. Moreover, within this region, isolated disclinations are absent and dislocations are always found in pairs. This indicates that the corresponding states exhibit *quasi long-range order* and that there is *no hexatic phase* in our model. Increasing the density further ($\gtrsim 0.775$ for $\nu = 1.6$), one observes a *defect-free* stationary state with $d = 0$. The decay of the averaged defect ratio can be roughly fitted by $\langle d \rangle_t \propto (\rho_c - \rho)^\delta$, with δ being in the interval $[0.35, 0.4]$. *Snapshots*: Each snapshot depicts the state's triangulation for a representative configuration in time and corresponds to $\nu = 1.6$ (blue data points). The respective density ρ is indicated by means of the black arrows.

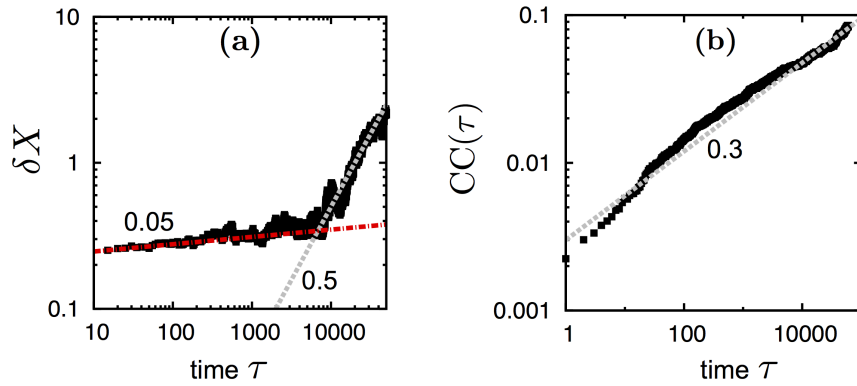


FIG. S3: *Motion of topological defects*: Since the number of topological defects is rather small in the stationary state, their motion cannot be characterized by studying the defect’s mean square displacement within an appropriate statistical accuracy. Therefore, we analyzed **(a)** the *particles’ mean square displacement* $\delta X(\tau) = \sqrt{\langle [\mathbf{x}_i(t_0 + \tau) - \mathbf{x}_i(t_0)]^2 \rangle_i}$, with i denoting the particle index and t_0 is a time point where the number of defects $d(t)$ have become approximately stationary. We find a *sub-diffusive* particle motion for small and intermediate time scales with $\delta X \sim \tau^{0.05}$ (red dash-dotted line). At large time scales there is a crossover to a diffusive regime with $\delta X \sim \tau^{0.5}$ (grey dotted line). Moreover, we evaluated **(b)** the *cage correlation function* [6], $CC(\tau)$, here defined as the ratio of particles which have changed at least once their neighborhood (often referred to as “cage”). In the time regime corresponding to sub-diffusive particle motion, mostly none of the particles have rearranged their neighborhood. We find that in the considered time regime $CC(\tau)$ increases according to a power-law $CC(\tau) \sim \tau^{0.3}$, whereby the ratio of rearranged cages remains relatively small; until the crossover to the diffusive regime only about 5% of the particles have rearranged their cage(s). Since defects can either move by cage rearrangements or particle motion, we can conclude that defect also move sub-diffusively—as the particles—at least for small time scales. The slow movements of the topological defects makes it practically unfeasible to follow numerically the annihilation processes of just a few remaining dislocations in the system, *i.e.* the process $d \rightarrow 0$ for large time scales when starting with a random initial condition (\mathcal{R}). Parameters: $\rho = 0.75$, $\nu = 1.2$, random initial condition \mathcal{R} .

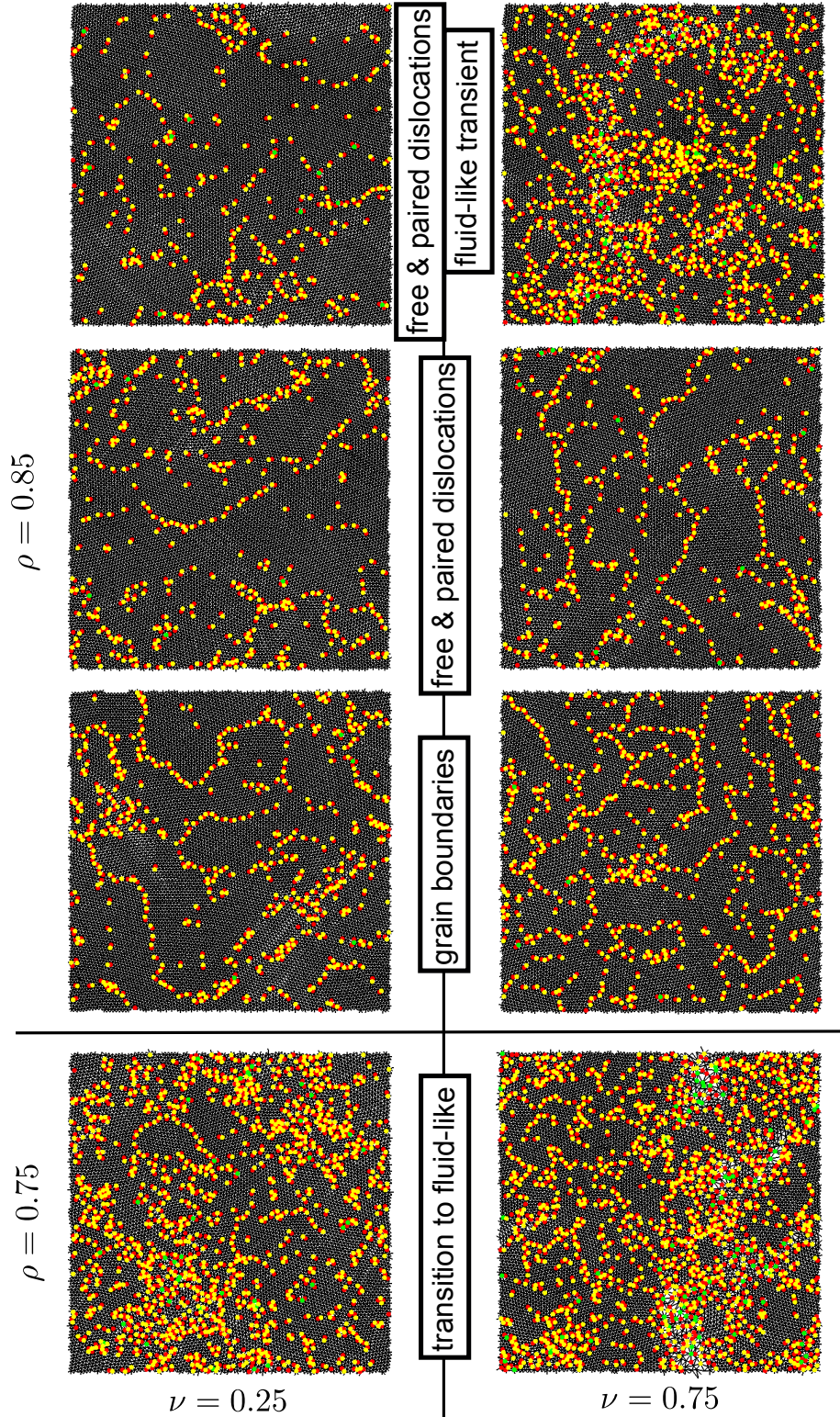


FIG. S4: Illustration of the spatial arrangements of dislocations for $\nu < 1$ (left: weakly intermittent $\nu = 0.25$; right: intermittent state $\nu = 0.75$), and densities $\rho = 0.85$ and $\rho = 0.75$. For $\rho = 0.85$, three representative configurations in time (no particular order in time) are depicted for each of the two ν -values. Even though intermittency is different for $\nu = 0.25$ and $\nu = 0.75$, one finds a similar arrangement of dislocations ranging from periods with mostly connected grain boundaries, to periods of pronounced coexistence between bound and free dislocations. In contrast, for $\rho = 0.75$, defects are large in number ($d \sim 0.2$) and appear spatially disordered. Therefore, we term this state fluid-like.

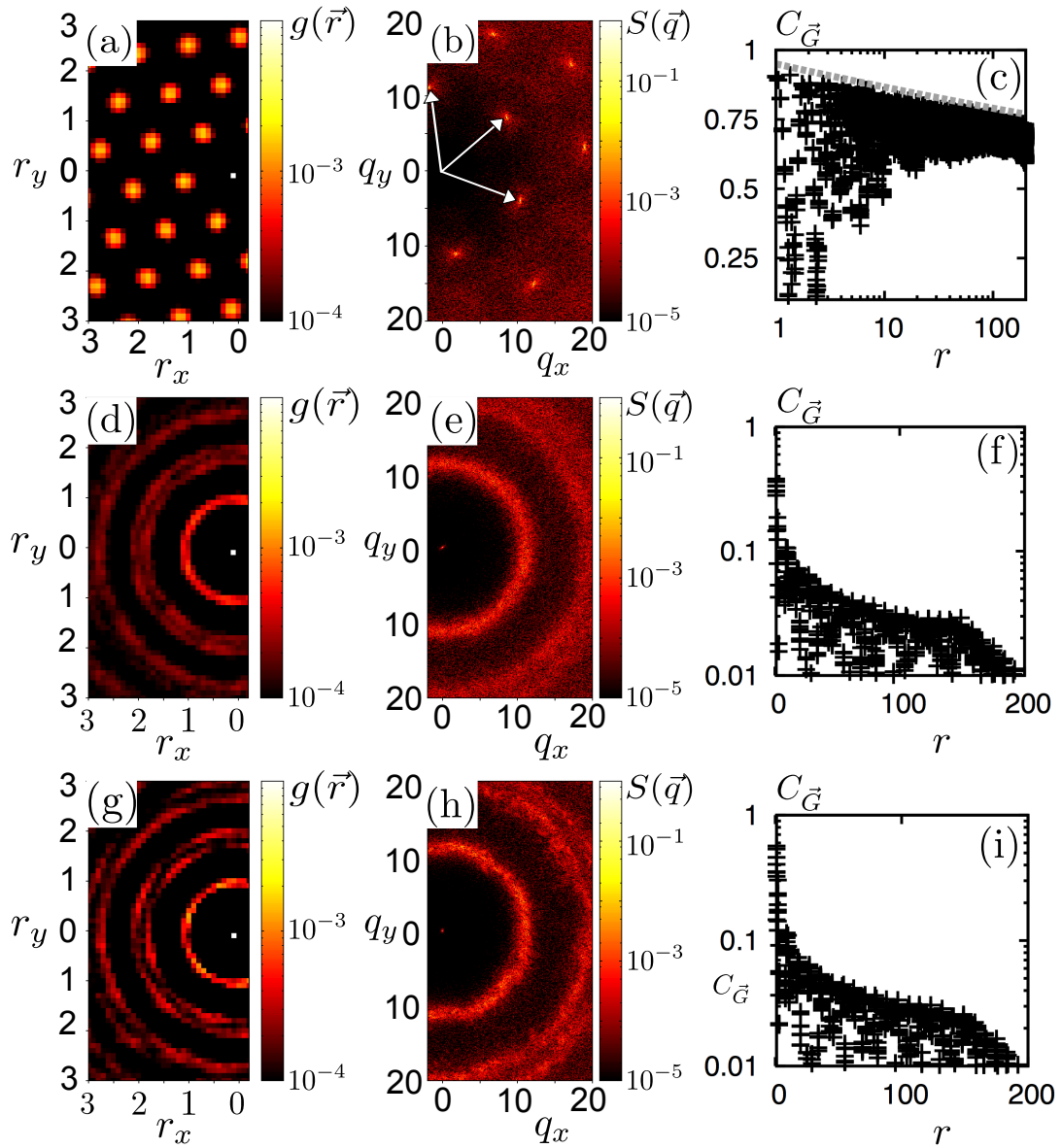


FIG. S5: Pair correlation function $g(\mathbf{r})$, static structure factor $S(\mathbf{q})$ and Correlation function $C_{\vec{G}}$ for decreasing values of ν (from top to bottom). (a,b,c) corresponds to $(\rho, \nu) = (0.85, 1.5)$, (d,e,f) to $(\rho, \nu) = (0.85, 0.75)$ and (g,h,i) to $(\rho, \nu) = (0.85, 0.25)$, respectively. Reciprocal lattice vectors \vec{G} are indicated by white arrows in (b). Note that since the stationary states for $\nu < 1$ develop very fast, there is no difference in the results obtained by either starting from a hexagonal (\mathcal{H}) or a disordered (\mathcal{R}) configuration. Results correspond to a simulation box of size $L = 400$ containing $N = 172156$ particles.

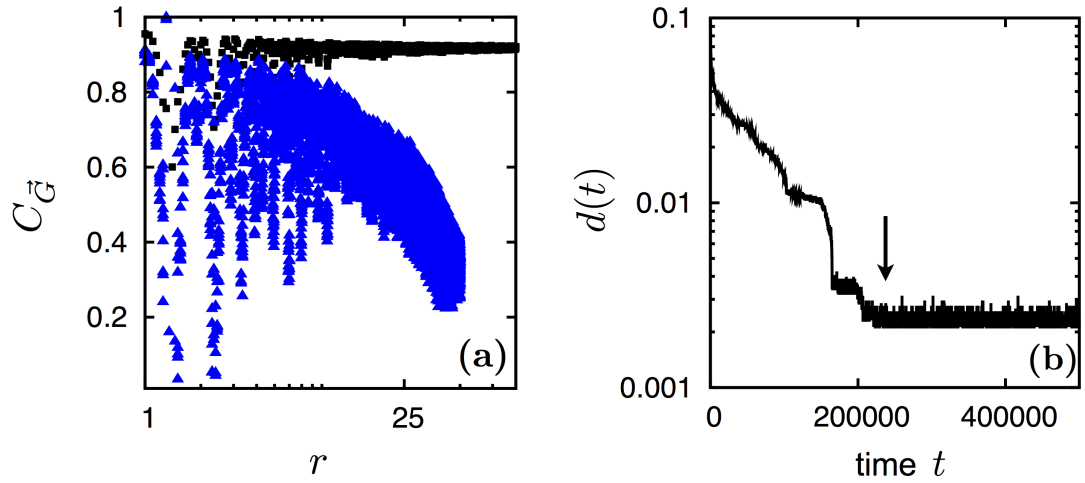


FIG. S6: (a) Comparison of the translational correlation function $C_{\mathbf{G}}$ of the considered *crystalline state* ($\rho = 0.85, \nu = 1.5$) for the *two* different initial conditions: *Random*(\mathcal{R}) and *hexagonal*(\mathcal{H}). The black curve depicts the results already presented in the main text [Fig. 3(c)]. It corresponds to a defect-free ($d = 0$) stationary state. For this *hexagonal*(\mathcal{H}) initial conditions were chosen since the time for all defects to vanish out of the system increases to time scales that cannot be addressed numerically (explanation see caption of Supplemental Fig. S3). The blue curve corresponds to the same parameter set, but the system was initialized in a *random* configuration (\mathcal{R}). We selected the realization with the smallest number of topological defects and computed $C_{\mathbf{G}}$ within the “last quasi-stationary” regime. The corresponding time trace of the defect ratio $d(t)$ is shown in (b). The begin of the “last quasi-stationary” plateau is marked by an arrow. The existence of defects ($d \neq 0$) leads to an underestimation of the decay of $C_{\mathbf{G}}$.

Appendix C

Materials & Methods for Section on *Anomalous* Contour Fluctuations

Stochastic molecular dynamic model:

The stochastic model treats the polymer as N discretized beads of size d , which are coupled by harmonic springs for tangential stretching and bending. For bending forces along the polymer contour, we employ the well-established *Worm-like Chain* model [24], with the bending force at bead i given by

$$\mathbf{F}_i^{\text{bend}} = \frac{\mathcal{E}}{d} \frac{\partial}{\partial \mathbf{x}_i} \sum_j \mathbf{T}_j \cdot \mathbf{T}_{j+1}, \quad (\text{C.1})$$

where $\mathbf{T}_i(t)$ denotes the tangent of the i -th bead, defined as $\mathbf{T}_i = \mathbf{x}_i - \mathbf{x}_{i-1}/|\mathbf{x}_i - \mathbf{x}_{i-1}|$, and \mathcal{E} [energy \times length] is the bending rigidity. Each bead is exposed to uncorrelated thermal fluctuations $\xi(t)$, *i.e.*

$$\langle \xi_i(t) \xi_j(t') \rangle = 2\mu k_b T \delta(t - t') \delta_{ij}, \quad (\text{C.2})$$

where μ denoting the hydrodynamic mobility of the bead. We neglect filament stretching by choosing the corresponding spring constant K_c much larger than \mathcal{E}/d^2 , thereby the only quantity characterizing the thermal filament dynamics is the the persistence length $\ell_p = \mathcal{E}/k_b T$ and the longest relaxation time [?]

$$\tau_c = \frac{\zeta}{\ell_p k_B T} (L/4.73)^4, \quad (\text{C.3})$$

where $L = Nd$ is the filament length and ζ denotes the friction coefficient of the considered rod segment. We chose the parameters according to experimental measurements for actin [?], with $\ell_p \approx 15\mu m$ and $\tau_c \approx 0.6s$ for $L = 8\mu m$.

We simplify the interactions between the filament and the 2d-motor lawn to a process of stochastic and independent binding events of motors along the filament contour. A motor begins its cycle with the “Hold”-state by binding randomly at bead i (with coordinates \mathbf{x}_i)

with probability $1/N$, independent of the bead’s binding history or state occupancy. After attaching to the filament, say at time $t = 0$, the motor attains the spatial coordinates of the randomly selected bead, plus some small randomly chosen distance \mathbf{R}_i ⁽¹⁾. The motor stays in this configuration, called *holding state*, for a time period of the holding time τ_h . During this time period the motor provides a rigid link between substrate and filament for displacements beyond some critical distance l_c . Specifically, the corresponding restoring force is zero for $|\mathbf{x}_i(0) - \mathbf{x}_i(t)| < l_c$, and proportional to K_h for $|\mathbf{x}_i(0) - \mathbf{x}_i(t)| \geq l_c$ (harmonic force $\mathbf{F}_i^{\text{hold}}$ pointing parallel to $\mathbf{x}_i(0) - \mathbf{x}_i(t)$, and with $K_h \approx K_c$). We assume that the upper bound for this critical length is essentially given by the S2 domain of HMM (tail part of the molecular motor), which is approximately 65nm [50]. However, the tail is probably partly attached to the substrate, thus we choose l_c equal to 30nm . After the holding time period, the *stroke phase* of the molecular motor is modeled as a spring that is connected to the filament, thereby exerting a force $\mathbf{F}_i^{\text{push}}$ on the filament while moving with a velocity $\Delta x_s/\tau_s$ (Δx_s denotes the stroke length) within the stroke time τ_s along its contour. For simplicity, we employ a linear spring with a constant $K_s \approx K_c$. A typical filament in the experiment is about $8\mu\text{m}$ in length and the stroke displacement has been estimated by measurements to be about 8nm [50], which is in agreement with our choice for $\Delta x_s = L \cdot 10^{-3}$ in the simulation. Moreover, we matched the time scales characterizing the molecular motor, *i.e.* $\tau_h = 0.001\text{s}$ and $\tau_s/\tau_h = 0.1$ [50], with the thermal relaxation time relaxation time τ_c : $\tau_c/\tau_h \approx 6 \cdot 10^2$.

Finally, we checked that fluctuations of the number of bound motors in time do not have any qualitative impact on the ensuing filament dynamics, therefore we kept the number of bound motors, denoted as m_b (either in “Hold” or “Push” state), constant. Apart from thermal fluctuations, the only stochastic element in our model is where (at which bead) the motor binds to the filament.

In summary, measuring distance in units of the bead diameter d , $\mathbf{x}_i \rightarrow \mathbf{x}_i/d$ and time we rescale as $t \rightarrow t/\frac{d^2}{\mu k_b T}$ [$\mu = (0.5\zeta d)^{-1}$ is the Rouse mobility of a sphere], we face the following discretized Langevin equation:

$$\begin{aligned} \mathbf{x}_i(t + \Delta t) - \mathbf{x}_i(t) &= \Delta t \frac{\ell_p}{d} \left[\frac{\partial}{\partial \mathbf{x}_i} \sum_j \mathbf{T}_j \cdot \mathbf{T}_{j+1} \right] + \tilde{\mathbf{F}}_i^{\text{stretch}} \Delta t + \sqrt{2\Delta t} \xi(t)_{(0,1)} \quad (\text{C.4}) \\ + \Delta t &\begin{cases} \tilde{\mathbf{F}}_i^{\text{hold}} & \text{if } t \in [0, \tau_h], |\mathbf{x}_i(0) + \mathbf{R}_i - \mathbf{x}_i(t)| \geq l_c, \\ \tilde{\mathbf{F}}_i^{\text{push}}(\Delta x_s/\tau_s) & \text{if } t \in [\tau_h, \tau_h + \tau_s], \end{cases} \quad (\text{C.5}) \end{aligned}$$

where $\tilde{\mathbf{F}}^{\dots}$ denoting the respective non-dimensional forces ², τ is the simulation time-scale, and \mathbf{R}_i denotes the aforementioned random distance with respect to bead i and \mathbf{T}_i is the the local tangent. $\xi(t)_{(0,1)}$ is an uncorrelated random number drawn from a Gaussian distribution with zero mean and standard deviation equal to 1.

¹For simplicity, \mathbf{R}_i is a vector with random orientation and randomly chosen radii within $[0, l_c]$.

²We skip to write down an explicit form of these non-dimensional forces, since their spring constants are chosen such that their relaxation occurs on some Δt . However, it is worth noting that their characteristic on/off time scales (*i.e.* τ_h and τ_s) are crucial for the dynamics.

Bibliography

- [1] R. Aditi Simha und S. Ramaswamy, *Phys. Rev. Lett.* **89** (2002), 058101.
- [2] V. et al., *Nature* **398** (1999), 530.
- [3] W. et al., *Nature* **378** (1995), 748.
- [4] T.E. Angelini, E. Hannezo, X. Trepate, M. Marquez, J.J. Fredberg und D.A. Weitz, *Proceedings of the National Academy of Sciences* **108** (2011), 4714.
- [5] I.S. Aranson, D. Blair, V.A. Kalatsky, G.W. Crabtree, W.K. Kwok, V.M. Vinokur und U. Welp, *Phys. Rev. Lett.* **84** (2000), 3306.
- [6] I.S. Aranson, A. Sokolov, J.O. Kessler und R.E. Goldstein, *Phys. Rev. E* **75** (2007), 040901.
- [7] I.S. Aranson und L.S. Tsimring, *Phys. Rev. E* **71** (2005), 050901.
- [8] I.S. Aranson und L.S. Tsimring, *Rev. Mod. Phys.* **78** (2006), 641.
- [9] I.S. Aranson und L.S. Tsimring: *Granular Patterns*. Oxford University press, New-York, 2009.
- [10] I.S. Aranson, D. Volfson und L.S. Tsimring, *Phys. Rev. E* **75** (2007), 051301.
- [11] G. Baglietto und E.V. Albano, *Phys. Rev. E* **80** (2009), 050103.
- [12] A. Baskaran und M.C. Marchetti, *Phys. Rev. Lett.* **101** (2008), 268101.
- [13] A. Baskaran und M.C. Marchetti, *Phys. Rev. E* **77** (2008), 011920.
- [14] M. Bathe, C. Heussinger, M.M. Claessens, A.R. Bausch und E. Frey, *Biophysical Journal* **94** (2008), 2955 .
- [15] E. Bertin, M. Droz und G. Grégoire, *Phys. Rev. E* **74** (2006), 022101.
- [16] E. Bertin, M. Droz und G. Grégoire, *Journal of Physics A: Mathematical and Theoretical* **42** (2009), 445001.
- [17] J. Bialké, T. Speck und H. Löwen, *Phys. Rev. Lett.* **108** (2012), 168301.

- [18] D.L. Blair, T. Neicu und A. Kudrolli, *Phys. Rev. E* **67** (2003), 031303.
- [19] L. Bourdieu, M. Magnasco, D. Winkelmann und A. Libchaber, *Physical Review E* **52** (1995), 6573.
- [20] N.V. Brilliantov und T. Pöschel: *Kinetic Theory of Granular Gases*. Oxford University press, New-York, 2004.
- [21] T. Butt, T. Mufti, A. Humayun, P.B. Rosenthal, S. Khan, S. Khan und J.E. Molloy, *Journal of Biological Chemistry* **285** (2010), 4964.
- [22] H. Chaté, F. Ginelli, G. Grégoire, F. Peruani und F. Raynaud, *The European Physical Journal B - Condensed Matter and Complex Systems* **64** (2008), 451.
- [23] H. Chaté, F. Ginelli, G. Grégoire und F. Raynaud, *Phys. Rev. E* **77** (2008), 046113.
- [24] J.d. Cloizeaux und G. Jannink: *Polymers in Solution: Their modelling and structure*. Clarendon Press, Oxford, New York, 1990.
- [25] D.S. Courson und R.S. Rock, *Journal of Biological Chemistry* **285** (2010), 26350.
- [26] M. Cross und H. Greenside: *Pattern formation and dynamics in nonequilibrium systems*. Cambridge, New York, 2009.
- [27] M.C. Cross und P.C. Hohenberg, *Rev. Mod. Phys.* **65** (1993), 851.
- [28] A. Czirók, H.E. Stanley und T. Vicsek, *Journal of Physics A: Mathematical and General* **30** (1997), 1375.
- [29] A. Czirók und T. Vicsek, *Physica A: Statistical Mechanics and its Applications* **281** (2000), 17 .
- [30] J. Deseigne, O. Dauchot und H. Chaté, *Phys. Rev. Lett.* **105** (2010), 098001.
- [31] J. Deseigne, S. Léonard, O. Dauchot und H. Chaté, *Soft Matter* **8** (2012), 5629.
- [32] C. Dombrowski, L. Cisneros, S. Chatkaew, R.E. Goldstein und J.O. Kessler, *Phys. Rev. Lett.* **93** (2004), 098103.
- [33] S. Dorbolo, D. Volfson, L. Tsimring und A. Kudrolli, *Phys. Rev. Lett.* **95** (2005), 044101.
- [34] M.R. D’Orsogna, Y.L. Chuang, A.L. Bertozzi und L.S. Chayes, *Phys. Rev. Lett.* **96** (2006), 104302.
- [35] T. Duke, E.T. Holy und S. Leibler, *Physical Review Letters* **74** (1995), 330.
- [36] U. Erdmann, W. Ebeling und A.S. Mikhailov, *Phys. Rev. E* **71** (2005), 051904.

- [37] U. Erdmann, W. Ebeling, L. Schimansky-Geier und F. Schweitzer, *The European Physical Journal B - Condensed Matter and Complex Systems* **15** (2000), 105.
- [38] M. Faretta und B. Bassetti, *EPL (Europhysics Letters)* **41** (1998), 689.
- [39] L. Giomi, L. Mahadevan, B. Chakraborty und M.F. Hagan, *Phys. Rev. Lett.* **106** (2011), 218101.
- [40] G. Grégoire und H. Chaté, *Phys. Rev. Lett.* **92** (2004), 025702.
- [41] G. Grégoire, H. Chaté und Y. Tu, *Physica D: Nonlinear Phenomena* **181** (2003), 157 .
- [42] D. Grossman, I.S. Aranson und E.B. Jacob, *New Journal of Physics* **10** (2008), 023036.
- [43] R. Gromann, L. Schimansky-Geier und P. Romanczuk, *New Journal of Physics* **14** (2012), 073033.
- [44] Y. Harada, K. Sakurada, T. Aoki, D.D. Thomas und T. Yanagida, *Journal of molecular biology* **216** (1990), 49.
- [45] J. Harting, H.J. Herrmann und E. Ben-Naim, *EPL (Europhysics Letters)* **83** (2008), 30001.
- [46] S. Henkes, Y. Fily und M.C. Marchetti, *Phys. Rev. E* **84** (2011), 040301.
- [47] C. Heussinger, M. Bathe und E. Frey, *Phys. Rev. Lett.* **99** (2007), 048101.
- [48] H. Hinrichsen, *Physica A: Statistical Mechanics and its Applications* **369** (2006), 1 .
- [49] P. Hohenberg, *Physical Review* **158** (1967), 383.
- [50] J. Howard: *Mechanics of Motor Proteins and the Cytoskeleton*. Palgrave Macmillan, 2005.
- [51] T. Ihle, *Phys. Rev. E* **83** (2011), 030901.
- [52] J. Schäfer, S. Dippel und D. E. Wolf, *J. Phys. I France* **6** (1996), 5.
- [53] M. Kardar: *Statistical Physics of Particles*. Cambridge University press, New-York, 2007.
- [54] S. Köhler und A. Bausch, *PLoS ONE* **7** (2012), e39869.
- [55] S. Köhler, V. Schaller und A. Bausch, *PLoS ONE* **6** (2011), e23798.
- [56] K. Kohlstedt, a. Snezhko, M. Sapochnikov, I. Aranson, J. Olafsen und E. Ben-Naim, *Physical Review Letters* **95** (2005), 068001.

- [57] J.M. Kosterlitz und D.J. Thouless, *Journal of Physics C: Solid State Physics* **6** (1973), 1181.
- [58] A. Kudrolli, G. Lumay, D. Volfson und L.S. Tsimring, *Phys. Rev. Lett.* **100** (2008), 058001.
- [59] A. Lau, B. Hoffman, A. Davies, J. Crocker und T. Lubensky, *Physical Review Letters* **91** (2003), 198101.
- [60] L. Le Goff, F. Amblard und E. Furst, *Physical Review Letters* **88** (2001), 018101.
- [61] L. Le Goff, O. Hallatschek, E. Frey und F.m.c. Amblard, *Phys. Rev. Lett.* **89** (2002), 258101.
- [62] V. Levi, A.S. Serpinskaya, E. Gratton und V. Gelfand, *Biophysical journal* **90** (2006), 318.
- [63] H. Levine, W.J. Rappel und I. Cohen, *Phys. Rev. E* **63** (2000), 017101.
- [64] R. Mach und F. Schweitzer, *Bulletin of Mathematical Biology* **69** (2007), 539.
- [65] M.C. Marchetti, J.F. Joanny, S. Ramaswamy, T.B. Liverpool, J. Prost, M. Rao und R.A. Simha, *arXiv:1207.2929 cond-mat.soft* (2012).
- [66] A.M. Menzel und H. Löwen, *Phys. Rev. Lett.* **110** (2013), 055702.
- [67] A.M. Menzel und T. Ohta, *EPL (Europhysics Letters)* **99** (2012), 58001.
- [68] N.D. Mermin, *J. Math. Phys.* **8** (1967), 1061.
- [69] N.D. Mermin und H. Wagner, *Phys. Rev. Lett.* **17** (1966), 1133.
- [70] S. Mishra, A. Baskaran und M.C. Marchetti, *Phys. Rev. E* **81** (2010), 061916.
- [71] V. Narayan, N. Menon und S. Ramaswamy, *Journal of Statistical Mechanics: Theory and Experiment* **2006** (2006), P01005.
- [72] D.R. Nelson: *Defects and Geometry in Condensed Matter Physics*. Cambridge University Press, 2002.
- [73] D.R. Nelson, M. Rubinstein und F. Spaepen, *Philosophical Magazine A* **46** (1982), 105.
- [74] L. Peng, Y. Zhao, B. Tian, J. Zhang, B.H. Wang, H.T. Zhang und T. Zhou, *Phys. Rev. E* **79** (2009), 026113.
- [75] F. Peruani, A. Deutsch und M. Bär, *Phys. Rev. E* **74** (2006), 030904.

- [76] F. Peruani, T. Klaus, A. Deutsch und A. Voss-Boehme, *Phys. Rev. Lett.* **106** (2011), 128101.
- [77] F. Peruani und L.G. Morelli, *Phys. Rev. Lett.* **99** (2007), 010602.
- [78] F. Peruani, J. Starruß, V. Jakovljevic, L. SØgaard-Andersen, A. Deutsch und M. Bär, *Phys. Rev. Lett.* **108** (2012), 098102.
- [79] A. Peshkov, I.S. Aranson, E. Bertin, H. Chaté und F. Ginelli, *Phys. Rev. Lett.* **109** (2012), 268701.
- [80] A. Peshkov, S. Ngo, E. Bertin, H. Chaté und F. Ginelli, *Phys. Rev. Lett.* **109** (2012), 098101.
- [81] S. Ramaswamy, *Annual Review of Condensed Matter Physics* **1** (2010), 323.
- [82] S. Ramaswamy, R.A. Simha und J. Toner, *Europhys. Lett.* **62** (2003), 196.
- [83] P. Romanczuk, M. Bär, W. Ebeling, B. Lindner und L. Schimansky-Geier, *The European Physical Journal - Special Topics* **202** (2012), 1.
- [84] P. Romanczuk und L. Schimansky-Geier, *Phys. Rev. Lett.* **106** (2011), 230601.
- [85] D. Saintillan und M.J. Shelley, *Phys. Rev. Lett.* **99** (2007), 058102.
- [86] D. Saintillan und M.J. Shelley, *Phys. Rev. Lett.* **100** (2008), 178103.
- [87] V. Schaller und A.R. Bausch, *Proceedings of the National Academy of Sciences* **110** (2013), 4488.
- [88] V. Schaller, B. Hammerich und A. Bausch, *The European Physical Journal E* **35** (2012), 1.
- [89] V. Schaller, C.A. Weber, B. Hammerich, E. Frey und A.R. Bausch, *Proceedings of the National Academy of Sciences* **108** (2011), 19183.
- [90] V. Schaller, C.A. Weber, C. Semmerich, E. Frey und A. Bausch, *Nature* **467** (2010), 73.
- [91] A. Snezhko und I.S. Aranson, *Nature Materials* **10** (2011), 698703.
- [92] A. Snezhko, K. Barlan, I.S. Aranson und V.I. Gelfand, *Biophysical journal* **99** (2010), 3216.
- [93] Y. Sumino, K.H. Nagai, Y. Shitaka, D. Tanaka, K. Yoshikawa, H. Chaté und K. Oiwa, *Nature* **483** (2012), 448.
- [94] B. Szabó, G.J. Szöllösi, B. Gönci, Z. Jurányi, D. Selmeczi und T. Vicsek, *Phys. Rev. E* **74** (2006), 061908.

- [95] J. Toner, *Phys. Rev. E* **86** (2012), 031918.
- [96] J. Toner und Y. Tu, *Phys. Rev. Lett.* **75** (1995), 4326.
- [97] J. Toner und Y. Tu, *Phys. Rev. E* **58** (1998), 4828.
- [98] J. Toner, Y. Tu und S. Ramaswamy, *Annals of Physics* **318** (2005), 170 .
- [99] Y. Toyoshima, S. Kron, E. McNally, K. Niebling, C. Toyoshima und J.A. Spudich, *Nature* **328** (1987), 536.
- [100] Y.Y. Toyoshima, S.J. Kron und J.a. Spudich, *Proceedings of the National Academy of Sciences of the United States of America* **87** (1990), 7130.
- [101] Y. Tu, J. Toner und M. Ulm, *Phys. Rev. Lett.* **80** (1998), 4819.
- [102] A. Turing, *Bulletin of Mathematical Biology* **52** (1990), 153 .
- [103] T.Q. Uyeda, S.J. Kron und J.a. Spudich, *Journal of molecular biology* **214** (1990), 699.
- [104] T.Q. Uyeda, H.M. Warrick, S.J. Kron und J.A. Spudich, *Nature* **352** (1991), 307.
- [105] T. Vicsek, A. Czirók, E. Ben-Jacob, I. Cohen und O. Shochet, *Phys. Rev. Lett.* **75** (1995), 1226.
- [106] T. Vicsek und A. Zafeiris, *Physics Reports* **517** (2012), 71 .
- [107] C.A. Weber, V. Schaller, A.R. Bausch und E. Frey, *Phys. Rev. E* **86** (2012), 030901.
- [108] H.H. Wensink und H. Löwen, *Journal of Physics: Condensed Matter* **24** (2012), 464130.
- [109] T. Yanagida, M. Nakase, K. Nishiyama und F. Oosawa, *Nature* **307** (1984), 58.
- [110] H.P. Zhang, A. Be'er, E.L. Florin und H.L. Swinney, *Proceedings of the National Academy of Sciences* **107** (2010), 13626.

Acknowledgement

Mein größter Dank geht an Erwin, meinem Betreuer während meiner Promotion. Ich bedanke mich vor allem für das schier endlose Vertrauen mich meine Forschungsambitionen frei ausleben zu lassen. Ohne diese freie Art der Betreuung wäre der Umfang dieser Arbeit deutlich kleiner ausgefallen, und zudem, noch viel wichtiger, ich hätte die letzten 4 Jahre nicht annähernd so genossen. Danke Dir für die vielen lehrreichen Diskussionen, den Humor und die vielen tollen nicht wissenschaftlichen Gespräche. Diese Zeit hat mich sehr geprägt. Danke!

Außerdem möchte ich mich bei Flo und Volker bedanken. Kollaborieren mit Euch war schlichtweg der Hammer. Danke, dass ich mit Euch zusammenarbeiten durfte, und danke Euch auch als Freund!

Danke auch an meine lieben Kollegen am Lehrstuhl, mit ganz besonderem Dank an meinen Zimmerkollegen Louis (Danke nicht nur fürs Fenster aufmachen... ;)). Außerdem vielen Dank an Brendan, Timo, Flo, Ryo und Yvonne für Euer tolles Feedback zu dieser Arbeit. Ich sage nur: “Auch wenns oft unklar bleibt, doch ab und zu, können Satzzeichen Leben retten!” (z.B. Wir essen Opa.)

Zudem danke ich Andreas Bausch für seine Ehrlichkeit innerhalb unserer Zusammenarbeit und sein Verständnis, sowie die tollen und lehrreichen Diskussionen. Danke auch dem Ryo Suzuki für unsere tolle Kollaboration. Außerdem danke ich Hugues Chaté und Olivier Dauchot für das gemeinsame Arbeiten an den Projekt “Vibrated Disks”, und die endlosen Skypekonferenzen. Und, auch vielen Dank dem Igor Aranson für (die) vielen Diskussionen und (den) tollen Aufenthalt in Chicago.

Ein “special thanks” geht an Timo und Simon; das Arbeiten mit Euch hat mir ganz besonderen Spaß gemacht.

Zum Schluss möchte ich meiner geliebten Familie danken, Mum, Dad, Yvonne, Stefan und Julian—mit ganz besonderem Dank an meine Freundin Jessi, sowie meinen tollen Freunde, Melli, Tobi und Philipp. Danke Euch für Euer Freuen wenns was zu feiern gab, und Euer Verständnis, dass ich doch sehr oft “unter Spannung” war. DANKE EUCH!

Last but not least: Thanks to Daniels für deine gefürchteten Zauberkunststücke und vieles, vieles mehr.

Nachtrag: Vielen Dank für die gemeinsame Zeit, mein Freund!

Curriculum Vitae

CURRICULUM VITAE

Name: **Christoph Alexander Gerhard Weber**
Date/Place of Birth: 24.07.1983 / Munich
Address: Pestitzer Str. 16,
01187 Dresden
Phone: +49 0176 23382909
Email: Christoph.A.Weber@physik.lmu.de,
weber@pks.mpg.de



EDUCATION

Aug 2013 – Postdoc in the group of Prof. Jülicher (MPIPKS Dresden)
Oct 2009 – Jul 2013 Ph.D. in physics (summa cum laude) about
Modeling Propelled Particle Systems in 2d
at the Ludwig-Maximilian-University
Supervisor: Prof. Frey
Mar 2009 – Oct 2009 Project work in the group of Prof. Frey
and collaboration with the group of Prof. Rädler
Dec 2008 Certificate Focus Biophysics
Oct 2005 – Dec 2008 Diploma in Physics with honor (1.0)
at the Ludwig-Maximilian-University
Dec 2007 – Dec 2008 Diploma thesis on *Modeling of Free-Flow Electrophoresis*
in the framework of a collaboration with *Becton Dickinson*
Oct 2003 – Oct 2005 Pre-Diploma in Physics (1.1)
at the Ludwig-Maximilian-University
Sept 1996 – Jun 2003 Abitur at Gymnasium Kirchheim

INVITED TALKS & RESEARCH STAYS

Nov 2012 Research stay in the group of Prof. Igor Aronson
at the Argonne National Laboratory, Chicago
Jul 2012 Research stay at the MPIPKS Dresden in the framework of
the Advanced Study Group: *Statistical Physics of collective motion*
May 2012 Invited talk at *Particules actives*, ENS de Lyon
Feb 2012 Invited talk at the Humboldt-University Berlin in
the group of Lutz Schimansky-Geier
Aug 2011 – Sep 2011 Research stay at the MPIPKS Dresden, in the framework of Dynact11
May 2011 – June 2011 KITP research program
Biological Frontiers of Polymer and Soft Matter Physics, Santa Barbara

TEACHING

May 2012	– Jun 2012	Substituting E. Frey for the lecture part <i>kinetic theory</i> of the <i>Advanced Statistical Mechanics</i> course
summer term 2012		Organization of tutoring classes of the the <i>Advanced Statistical Mechanics</i> (Prof. Frey)
summer term 2011		Organization and design of a Reading Course on <i>Theoretical Biological Hydrodynamics</i>
Dec 2010	– Apr 2011	Organization and design of a seminar on <i>Hydrodynamics</i>
summer term 2010		Organization and lecturing of tutoring classes of the <i>Non-linear Dynamics & Pattern formation</i> (Prof. Frey)
winter term 2009/10		Tutoring classes of the <i>Statistical Physics</i> (Prof. Frey)
summer term 2009		Tutoring classes of the <i>Introduction to theoretical Biophysics</i> (Prof. Gerland)
winter term 2008/09		Tutoring classes of the <i>Statistical Physics</i> (Prof. Frey)
winter term 2007/08		Tutoring classes of the <i>Mathematics 3</i> (Prof. Winkler)
summer term 2007		Tutoring classes of the <i>Electrodynamics</i> (Prof. Frey)
winter term 2006/07		Tutoring classes of the <i>Mathematics 1</i> (Prof. Winkler)
summer term 2006		Tutoring classes of the <i>Analysis 1</i> (Prof. Donder)
winter term 2005/06		Tutoring classes of the <i>Linear Algebra</i> (Prof. Dürr)

SUPERVISION

Nov 2011	– Dec 2012	Master-student Simon Weber working on <i>Phase Separation of Two Species with different Activity</i>
Sept 2011	– Sept 2012	Master-student Timo Hanke working on <i>Understanding Collective Dynamics of Soft Active Colloids through Binary Scattering</i>
Mai 2011	– July 2012	Bachelor-student Benedikt Hooek working on <i>Onset of horizontal motion in simplified models for vibrated polar disks</i>
Sept 2010	– Oct 2011	Master-student Christopher Bock working on <i>Active matter at high densities</i>
Jun 2010	– Aug 2010	Bachelor-student Timo Hanke working on <i>Ordering by repulsive interactions</i>
Apr 2010	– Jun 2010	Bachelor-student Michael Hartmann working on <i>Hydrodynamic scattering of driven particles on a wall</i>
Mar 2009	– May 2009	Bachelor-student Alej Zielinski working on <i>Modeling of Chemical cell trapping in controlled alternating gradient fields</i>

SCHOLARSHIPS & AWARDS

Nov 2012		Center of Nano-Science Publication Award
Oct 2012		Nano-Initiative Munich (NIM) travel grant for Argonne research stay
Nov 2011		Center of Nano-Science Publication Award
Nov 2010		Center of Nano-Science Publication Award
Oct 2009	– Oct 2012	Scholarship from the IDK-NBT (“Bayerisches Elitenetzwerk”) with financial support between Oct 2009 – Oct 2010

NON-ACADEMIC EDUCATION

2003 – 2004 NLP Practitioner in accordance with GANLP/DVNLP guidelines
2005 – 2006 Assistance for NLP Practitioner

LANGUAGE SKILLS

German (native), English (fluent), French (basics).

COMPUTER SKILLS

C/C++, Bash/AWK, Latex, Mathematica, Comsol.

Ich versichere, die Arbeit selbstständig angefertigt und dazu nur die im Literaturverzeichnis angegebenen Quellen benutzt zu haben.

München, den 14. Mai 2013